TOPIC

VIBRATION ANALYSIS

OF SANDWICH STRUCTURE WITH AUXETIC AND NON -RE ENTRANT HONEYCOMB CORE

USING FINITE ELEMENT METHOD AND EXPERIMENTS

-MASTER'S THESIS BY
DEBARSHI BISWAS

VIBRATION ANALYSIS OF SANDWICH STRUCTURE WITH AUXETIC AND NON -RE ENTRANT HONEYCOMB CORE USING FINITE ELEMENT METHODS AND EXPERIMENTS

A THESIS SUBMITTED TO **JADAVPUR UNIVERSITY**

FOR THE DEGREE OF MASTER OF ENGINEERING

By

DEBARSHI BISWAS

UNIVERSITY ROLL NO:002111204005 (2021-2023)

EXAMINATION ROLL NO:M4AUT23004

REGISTRATION NO:136524 OF 2016-2017

UNDER THE GUIDANCE OF

DR.TANMOY BANDYOPADHYAY

DEPARTMENT OF MECHANICAL ENGINEERING

JADAVPUR UNIVERSITY

188, Raja S.C. Mallick Rd,

Kolkata 700032

JADAVPUR UNIVERSITY

FACULTY OF ENGINEERING & TECHNOLOGY

DEPARTMENT OF MECHANICAL ENGINEERING

CERTIFICATE OF APPROVAL

The foregoing thesis entitled " **Vibration analysis of sandwich structure with auxetic and non -re entrant honeycomb core using finite element methods and experiments**" is hereby approved as a creditable study of an engineering subject carried out and presented in a manner satisfactory to warrant its acceptance as a prerequisite to the degree for which it has been submitted. It is understood that by this approval the undersigned do not necessary endorse or approve any statement mode opinion expressed or conclusion drawn therein but approve the thesis only for the purpose for which it is submitted

Committee on Final Examination
for Evaluation of the Thesis

(Signature of Examiners)

*Only in case the recommendation is concurred in

JADAVPUR UNIVERSITY

FACULTY OF ENGINEERING & TECHNOLOGY DEPARTMENT OF MECHANICAL ENGINEERING

CERTIFICATE OF RECOMMENDATION

This is certified that the thesis entitled " **Vibration analysis of sandwich structure with auxetic and non -re entrant honeycomb core using finite element methods and experiments**" which is being submitted by Debarshi Biswas in partial fulfilment for the award of the degree of **Master of Automobile Engineering** to Jadavpur University, Kolkata 700032, during the academic year 2022-2023,is the record of the student's own work carried out by him under our supervision.

Thesis Guide
Assistant Professor: Dr.Tanmoy Bandyopadhyay
Department of Mechanical Engineering,
Jadavpur University
188, Raja S.C. Mallick Rd,
Kolkata 700032

Countersigned

Professor:Dr. Prof Amit Karmakar
Head of the Department of
Mechanical Engineering ,
Jadavpur University
188, Raja S.C. Mallick Rd,
Kolkata 700032

Professor:Dr. Ardhendu Ghoshal
Dean, Faculty Council of Engineering
& Technology
Jadavpur University
188, Raja S.C. Mallick Rd,
Kolkata 700032

JADAVPUR UNIVERSITY

FACULTY OF ENGINEERING & TECHNOLOGY

DEPARTMENT OF MECHANICAL ENGINEERING

DECLARATION OF ORIGINALITY & COMPLIANCE OF ACADEMIC ETHICS

It is hereby declared that the thesis entitled " **Vibration analysis of sandwich structure with auxetic and non -re entrant honeycomb core using finite element methods and experiments**", contains literature survey and original research work by the undersigned candidate, as part of his Degree of Master of Automobile Engineering.

All information in this document has been obtained and presented in accordance with academic rules and ethical conduct.

It is also declared that all materials and results, not original to this work have been fully cited and referred throughout this thesis, according to rules of ethical conduct

Name : DEBARSHI BISWAS

University Roll Number : 002111204005 (2021-2023)

Examination Roll Number : M4AUT23004

Registration Number : 136524 OF 2016-2017

Date:

(Signature)

(Contact:

ACKNOWLEDGEMENTS

I am most deeply grateful to my Master's thesis guide, Associate Professor Tanmoy Bandyopadhyay for his guidance, encouragement, helping me to understand the theory behind the problem and helping me in performing the experiments during my research work in the final year of my Master's course in Jadavpur University.

I am also thankful to Professor Sumanta Neogi and Professor Arghya Nandi for helping me to carry out the experiments in Applied Mechanics lab by sharing valuable knowledge on the domain of experimental modal analysis.

Technician Mr. Manojit Mondal has taught me how to operate the analyser to find natural frequency.

The financial assistance in the form of monthly stipend from AICTE helped me to carry out my Master's degree very smoothly and without any hassle.

ABSTRACT

The present finite element-based method is intended to analyse the interactions between the unit cell dimensions of cellular structures especially in the form auxetic honeycomb cores and the free vibration response of sandwich panels. The sandwich panels are assumed to be composed of an auxetic honeycomb metallic (Titanium or Aluminium) core and enveloped by two composite face sheets with a PMMA matrix and reinforced by carbon-nanotubes (CNTs). The deformations of the sandwich panels are modelled using a higher-order shear deformation theory considering seven degrees of freedom at each node of the finite elements. The effective properties of the CNT reinforced face-sheets which are dependent on the working temperature and CNT grading pattern are evaluated based on the extended rule of mixture. The properties of the auxetic honeycomb core are however dependent on the spatial orientation of the unit cells of the auxetic pattern and accounts for the anisotropic nature and Negative Poisson's Ratio (NPR) of the metallic core structure. The influence of crucial parameters like the core metal, twist angle, plate-aspect ratio, core to face-sheet thickness ratio, rotational speed and unit cell dimensions of the auxetic honeycomb core are analysed .Experiments were performed to find the natural frequency.

TABLE OF CONTENTS

CH1:-INTRODUCTION

1.1.OUTLINE OF SANDWICH STRUTURE

The use of sandwich structures has increased manifold in the recent years. The introduction of the nanocomposites like CNT or graphene has resulted in advanced properties like enhanced strength without any significant changes in the weight of the structure. In general, most engineering materials used in practice generally exhibit positive Poisson's ratio wherein any longitudinal strain results in an opposite lateral strain. However, materials that exhibit negative Poisson's ratio (referred to as 'Auxetic' materials) have garnered much research interest in the recent years. 'Auxetic' materials have an interesting geometry of the unit cell owing to which an elongation in the longitudinal direction is accompanied with a corresponding elongation in the lateral direction and vice-versa. The auxetic materials are mostly employed as the honeycomb core of sandwich panels owing to their innate ability to withstand the in-plane loadings. The core of such honeycomb sandwich panels are ideally much thicker than the skin and are usually composed of low-weight metallic components like aluminium or titanium in order to impart high specific strength to withstand induced vibratory disturbances. The sandwich honeycomb panels find widespread usage in automobile, aerospace and mechanical industries because of their ability to withstand higher loads and absorb sudden vibration and impact in the form of explosive waves or low-velocity projectile impact which acts as a safeguard for the soft core inside.

1.2.LITERATURE SURVEY

Sreenivasamurthy and Ramamurti [1] studied the first bending and first torsional frequencies of flat rotating low aspect ratio cantilever plates using finite element method. Kant and Swaminathan [2] presented analytical solutions of the natural frequency of simply supported composite and sandwich plates based on a higher-order refined theory. Rao and Desai [3] worked on a semi-analytical method to evaluate the natural frequencies and displacement and stress eigenvectors for simply supported, cross-ply laminated and sandwich plates using higher order mixed theory. Khare et al. [4] developed a higher-order theory using a higher-order facet plate element to analyse the free vibration of isotropic, orthotropic and layered anisotropic composite and sandwich laminates. Zhu et al. [5] presented the bending and free vibration analyses of thin-to-moderately thick composite plates reinforced by single-walled carbon nanotubes using the finite element method based on the first order shear deformation plate theory. Balawi and Abot [6] studied analytically the effective mechanical behaviour of hexagonal honeycombs and correlated with experimental results for aluminium honeycombs. The work intended to study the effective in-plane elastic moduli of the honeycombs as a function of their relative density. Chen and Ozaki [7] studied the effect of height of hexagonal honeycomb core on the elastic modulus finite element method (FEM). Lei at al. [8] carried out free vibration analysis of functionally graded nanocomposite plates reinforced by uniaxially aligned single-walled carbon nanotubes (SWCNTs) using the element-free *kp*-Ritz method and first-order shear deformation plate theory. Wang et al. [9] developed two-dimensional (2D) and the three-dimensional (3D) finite element models and performed modal tests to predict the natural frequencies and mode shapes of the sandwich panels. Grujicic et al. [10] studied the effect of prior processing and the resulting microstructure on the performance of all-metal sandwich-structures with an auxetic-hexagonal core when subjected to blast loading. Duong and Duc [11] carried out numerical studies to evaluate the elastic

effective properties, including Young modulus, Poisson's ratio, shear modulus and linear thermal expansion coefficient of composites reinforced by randomly distributed spherical particles made from auxetic materials. Duc and Cong [12] analysed the nonlinear dynamic response of sandwich composite plates with negative Poisson's ratio in auxetic honeycombs. In addition, Duc et al. [13] presented an analytical solution to investigate the nonlinear dynamic response and vibration of sandwich auxetic composite cylindrical panels. Zhang et al. [14] vibration performance of sandwich beams with honeycomb-corrugation hybrid cores using Finite element methods and modal analysis techniques. Wang et al [15] performed experiments and finite element (FE) simulations to study the free vibration of ultralight all-metallic (Ti-6Al-4V alloy) sandwich beams with corrugated channel cores. Wang et al. [16] studied the vibration characteristics of sandwich panels with a hierarchical composite honeycomb sandwich core using finite element models as well as modal tests. Zhao et al. [17] analysed the in-plane elastic behaviour of honeycombs under large deformations using the Reissner beam theory considering the axial, bending and shearing deformation of the inclined honeycomb wall. Singha et al. [18 , 19] studied the effects of multiple debonding and FG-CNT reinforcements on the free vibration of rotating pre-twisted sandwich plates in thermal environment Pham et al. [20] studied the free vibration behaviour of auxetic honeycomb sandwich plates with the functionally graded material (FGM) skin layers using an edge-based smoothed finite element method (ES-MITC3) and the proposed program was trained and predicted by an artificial neural network (ANN) model for better prediction capability. Kushwaha [21] performed the free vibration analysis of three types of uniform PLA based auxetic architecture metamaterials i.e. square, auxetic and honeycomb along with three of its hybrids i.e. square-auxetic, auxetic-honeycomb and square-honeycomb. Liu et al. [22] studied the nonlinear vibration characteristics of an all-composite sandwich (ACS) plate with a hexagon honeycomb core (HHC). Jiang et al. [23] analysed the free vibration of carbon fiber composite sandwich plates with re-entrant honeycomb cores by using experiment, theory and finite element method (FEM). Hamrouni et al. [24] studied the dynamic behaviour of sandwich structures made with an auxetic or non-auxetic re-entrant, rectangular and hexagonal core wherein the specimens were made with additive manufacturing technology. Jiang et al. [25] analysed the free vibration of carbon fiber composite sandwich plates with re-entrant honeycomb cores by using experiment, theory and finite element method (FEM). Hamrouni et al. [26] studied the dynamic behaviour of sandwich structures made with an auxetic or non-auxetic re-entrant, rectangular and hexagonal core wherein the specimens were made with additive manufacturing technology.

It is evident from the literature survey that sandwich panels have gained wide research interest as preferred engineering materials in the last decade. A wide range of structural modification is achievable based on the choice of the face plate and core combinations in sandwich structures. However, the advantages of auxetic honeycomb structures when used as the core of sandwich panels has not been dealt with as a research area of huge possibilities. The auxetic honeycomb structures are known to exhibit both positive and negative poisons ratios (NPR) based on choice of the unit cell geometry which may be classified as comprising as non re-entrant and re-entrant angles, respectively. The present work is thereby aimed to investigate the natural frequency of sandwich panels made from CNT reinforced composite PMMA matrix as the face sheets and a metallic titanium-alloy based auxetic honeycomb core. The displacement fields of the sandwich panel are derived based on the higher-order shear

deformation theory considering seven degrees of freedom at each node. The stiffness and the mass matrices are evaluated using the finite element methods using an iso-parametric plate formulation and the equilibrium equations are solved using the QR iteration method. The research work on the free vibration study of sandwich structures with auxetic honeycomb cores is found to be very limited. As such, the authors have performed a series of experiments with an auxetic core made from Poly lactic acid using additive manufacturing process and another auxetic aluminium core made using CNC milling process. The experimental results obtained are found to be in excellent agreement with the results obtained using the in-house codes developed based on the finite element methods (FEM). The influence of critical parameters like unit cell plate geometry, auxetic angle, auxetic thickness ratio, temperature, twist angle, aspect ratio of panel, core to face sheet thickness ratio, rotational speed and hub radius on the free vibration behaviour and the mode shape of sandwich plate with auxetic honeycomb core are presented and analysed in details in the current work. The effects of adhesive bonding used to fasten the face sheet and the core together as a unit at higher temperatures are neglected in the present work.

It is evident from the literature survey that sandwich panels have gained wide research interest as preferred engineering materials in the last decade. A wide range of structural modification is achievable based on the choice of the face plate and core combinations in sandwich structures. However, the advantages of auxetic honeycomb structures when used as the core of sandwich panels has not been dealt with as a research area of huge possibilities. The auxetic honeycomb structures are known to exhibit both positive and negative poisons ratios (NPR) based on choice of the unit cell geometry which may be classified as comprising as non re-entrant and re-entrant angles, respectively. The present work is thereby aimed to investigate the natural frequency of sandwich panels made from CNT reinforced composite PMMA matrix as the face sheets and a metallic titanium-alloy based auxetic honeycomb core. The displacement fields of the sandwich panel are derived based on the higher-order shear deformation theory considering seven degrees of freedom at each node. The stiffness and the mass matrices are evaluated using the finite element methods using an iso-parametric plate formulation and the equilibrium equations are solved using the QR iteration method. The research work on the free vibration study of sandwich structures with auxetic honeycomb cores is found to be very limited. As such, the authors have performed a series of experiments with an auxetic core made from Poly lactic acid using additive manufacturing process and another auxetic aluminium core made using CNC milling process. The experimental results obtained are found to be in excellent agreement with the results obtained using the in-house codes developed based on the finite element methods (FEM). The influence of critical parameters like unit cell plate geometry, auxetic angle, auxetic thickness ratio, temperature, twist angle, aspect ratio of panel, core to face sheet thickness ratio, rotational speed and hub radius on the free vibration behaviour and the mode shape of sandwich plate with auxetic honeycomb core are presented and analysed in details in the current work. The effects of adhesive bonding used to fasten the face sheet and the core together as a unit at higher temperatures are neglected in the present work.

CH 2: SANDWICH STRUCTURE

2.1.INTRODUCTION TO SANDWICH STRUCTURE

The ASTM defines a sandwich structure as follows:
A structural sandwich is a special form of a laminated composite comprising of a combination of different materials that are bonded to each other so as to utilise the properties of each separate component to the structural advantage of the whole assembly.

A sandwich consists of three main parts as illustrated in Fig.2.1.

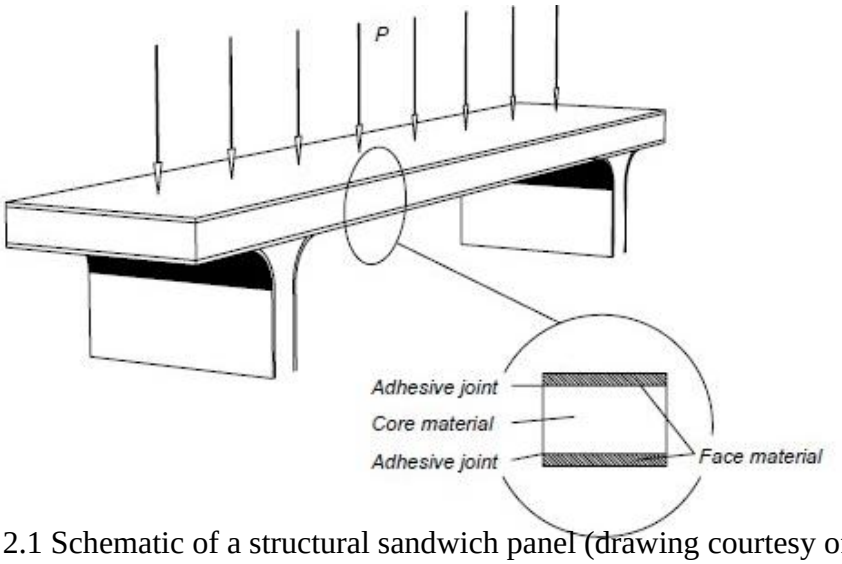

Figure 2.1 Schematic of a structural sandwich panel (drawing courtesy of Lars Falk).

Two thin, stiff, and strong faces are separated by a thick, light and weaker core. The faces are adhesively bonded to the core to obtain a load transfer between the components. The modus operandi of a sandwich is much the same as that of an I-beam, which is an efficient structural shape because as much as possible of the material is placed in the flanges situated farthest from the centre of bending or neutral axis. Only enough material is left in the connecting web to make the flanges work together and to resist shear and buckling. In a sandwich the faces take the place of the flanges and the core takes the place of the web. The difference is that the core of a sandwich is of a different material from the faces and it is spread out as a continuous support for the faces rather than concentrated in a narrow web. The faces will act together to form an efficient stress couple counteracting the external bending moment. The core resists shear and stabilises the faces against buckling or wrinkling. The bond between the faces and the core must be strong enough to resist the shear and tensile stresses set up between them.
The adhesive that bonds the faces to the core is thus of critical importance. The faces usually consist of thin and, in a classical meaning, high performing material while
the core material is a thick, light but relatively low performing material. The choice of constituents depends mainly on the specific application and the design criteria set up by it. The design of a structural sandwich will not be one of geometry only but an integrated process of sizing and materials selection.

2.2.ADVANTAGES AND DISADVANTAGES OF SANDWICH STRUCTURE

The advantages given by this design may be summarised**:**

high stiffness and strength to weight ratios, integration of functions such as thermal and acoustic insulation, high energy absorption capability, buoyancy, and few details. The way that a sandwich enhances the flexural rigidity of a structure without adding substantial weight has made the concept even more advantageous since the introduction of composite materials. These materials generally offer at least the same or even higher strengths as metals such as aluminium alloy or steel but their moduli are often much lower giving poor stiffness performance. By using sandwiched composites this problem can easily be overcome.
At present, the main drawbacks are:
production methods in infancy, complicated quality control, load introduction and joining difficulties, and lack of knowledge concerning the effect of damage. The sandwich concept has had a very strong development during the past years in increasing the knowledge of its mechanical behaviour, which has led to it being used in an increasing number of applications. Future research and development will, step by step, solve the above mentioned drawbacks and prove the sandwich concept even stronger.

2.3.APPLICATION OF SANDWICH STRUCTURE

Sandwich structures have been widely used in almost every branch of industry including aeronautical and aerospace industries, marine applications, civil engineering, and biomedical applications. Graphite-epoxy and carbon-epoxy multi-layered facings and aluminium or Nomex honeycomb core are typical in aerospace applications. Composite corrugate sandwich structures have been innovative developed by the interest in morphing aircraft. Sandwich structures with glass-epoxy or glass-vinyl ester facings and auxetic core are commonly used as marine structures. The blast resistance of auxetic and honeycomb sandwich panels is utilised for armoured vehicles application. In civil engineering, the sandwich structures usually have a closed-cell or open cell foam core and two glass-epoxy or glass-vinyl ester facings. The development of FRP sandwich panels with enhanced core structure provided an opportunity to expand the application in lightweight civil infrastructure. Smart materials used in smart sandwich structure provide a potential application in biomedical area.
Below are pictures of different applications of sandwich structures, where they come from and what advantages are gained by using a sandwich design. The set of applications is by no means complete and new interesting ones appear by the day.

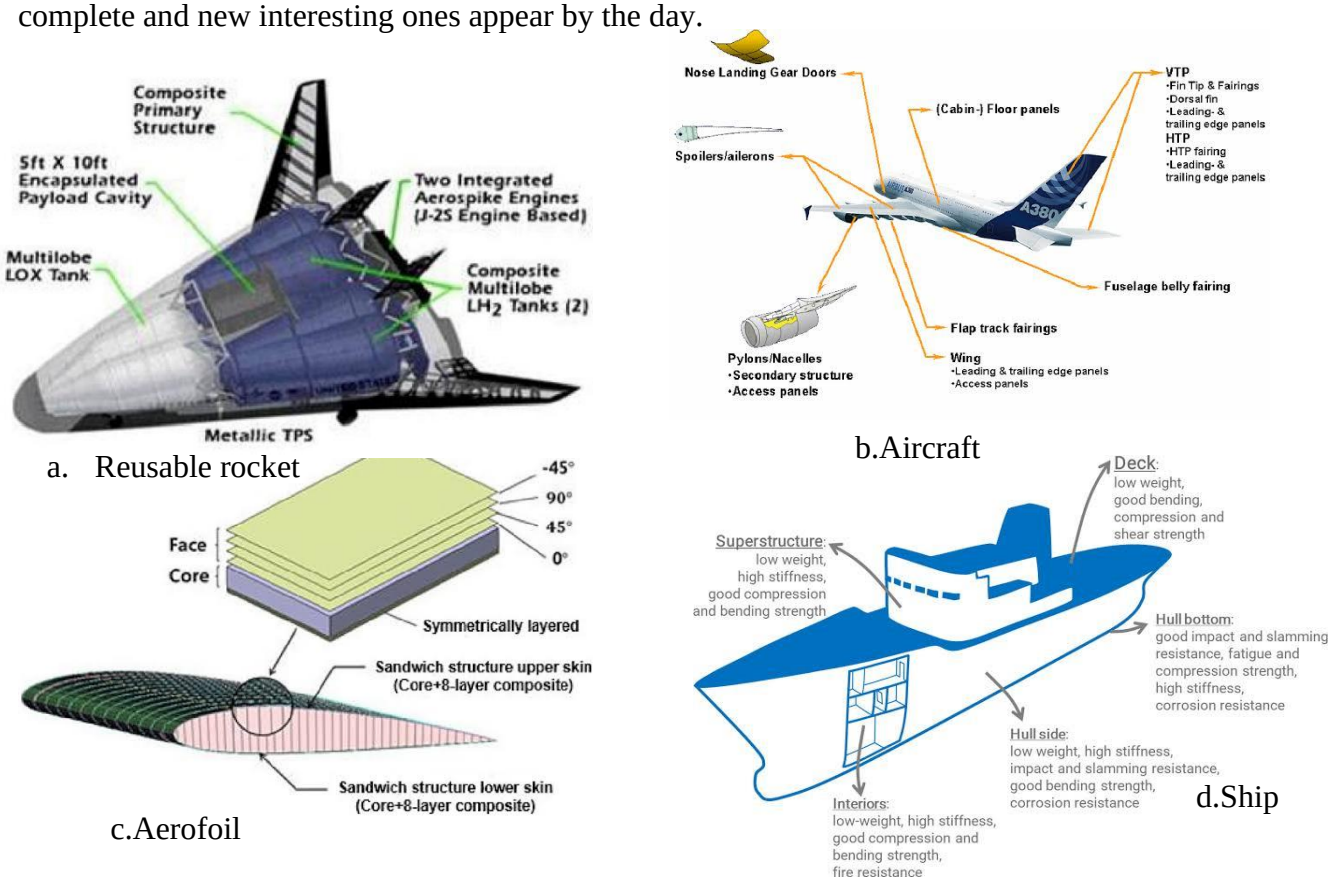

a. Reusable rocket

b.Aircraft

c.Aerofoil

d.Ship

Figure 2.2.Application of Sandwich structure

The basic concept of a sandwich panel is that the facings carry the bending loads (tension and compression), while the core carries the shear loads, much like the I-beam comparison shown in Fig. 2.3.

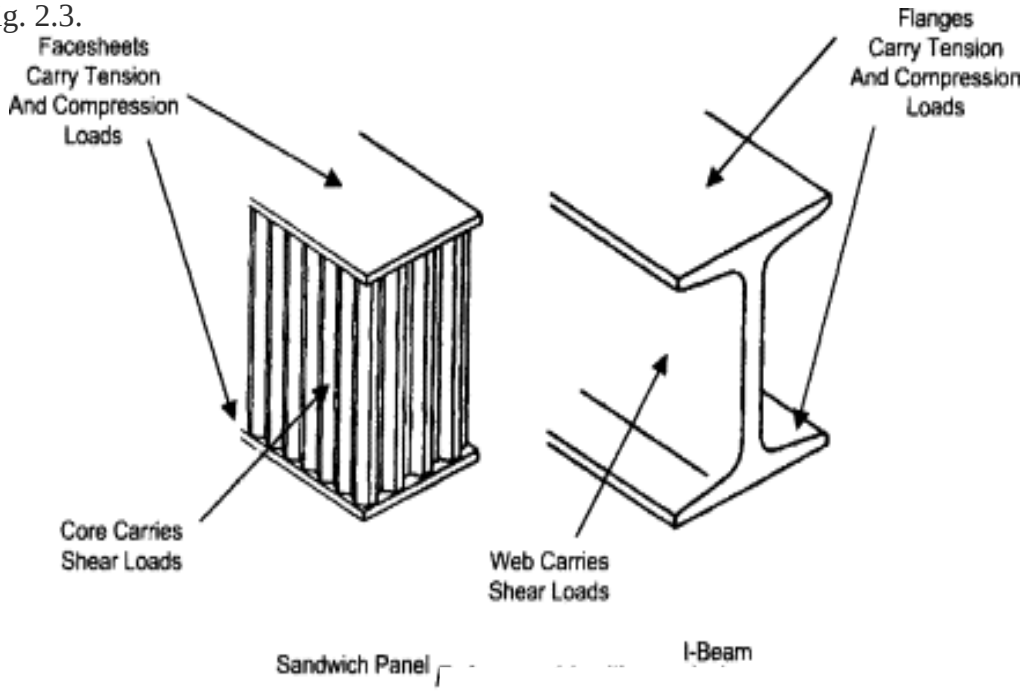

Figure 2.3. Why Sandwich Structures Are So Efficient

2.4. **FAILURE MODES OF SANDWICH STRUCTURE**

Possible failure modes of sandwich structures include tensile or compressive failure of the face sheets, debonding at the core/face sheet interface, indentation failure under localized loading, core failure, wrinkling of the compression face sheets, and global buckling.

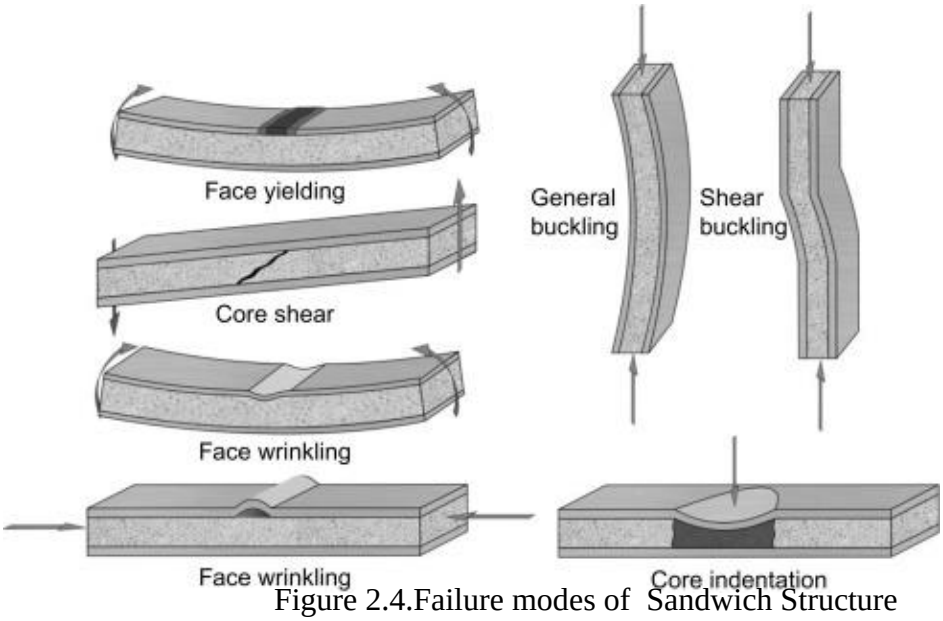

Figure 2.4.Failure modes of Sandwich Structure

CH-3:CARBON NANOTUBE(CNT)

3.1.WHAT ARE CARBON NANOTUBES?

Carbon nanotubes (CNTs) are cylindrical molecules that consist of rolled-up sheets of single-layer carbon atoms (graphene). They can be single-walled (SWCNT) with a diameter of less than 1 nanometre (nm) or multi-walled (MWCNT), consisting of several concentrically interlinked nanotubes, with diameters reaching more than 100 nm. Their length can reach several micrometres or even millimetres.

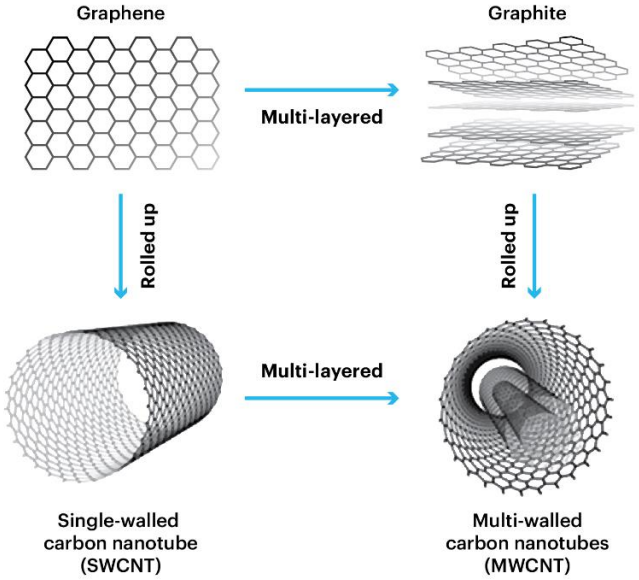

Figure 3.1.Graphene converted to SWNCT ,Graphite converted to MWCNT on rolling

- Carbon nanotubes are allotropes of carbon with a cylindrical nanostructure
- They have high length-to-diameter ratio of up to 132,000,000:1
- Nanotubes are members of the fullerene structural family
- Their name is derived from their long, hollow structure

3.2. PROPERTIES

- Highest strength to weight ratio which helps in creating light weight spacecrafts (strong like steel but light like aluminium, can bear maximum strain)
- It can easily penetrate membranes such as cell walls which helps in cancer treatment
- Electrical resistance changes significantly when other molecules attach themselves to the carbon atoms which help in developing sensors that can detect various problems (because these properties depends on rolling directions)

3.3.APPLICATION

- Can augment charge storage (supplementing Lithium-ion batteries life) and in super capacitors
- Graphene and CNT can replace transistors from the silicon chips as they are small and emit less heat
- Impact resistance materials
- Filters for removal of bacteria

- Can be used to make solar cells
- Smart fabrics
- CNT use in making bicycle components
- CNT for manufacturing of light weight boats

3.4. SYNTHESIS OF CARBON NANOTUBES

There are three main methods of nanotube synthesis:

- PLASMA ARC DISCHARGE: production of carbon nanotubes in an arc discharge plasma in a helium atmosphere.
- LASER EVAPORATION (pulsed laser ablation): evaporation of a graphite target in a high-temperature reaction by the action of a pulsed laser.
- CHEMICAL VAPOR DEPOSITION (CVD)**:** catalytic (nickel, cobalt, iron or their combinations) deposition of carbon from hydrocarbons (methane, ethylene, acetylene)

CVD is the most developed method for commercial production of CNTs.

This method also gives more flexibility in terms of diameter, length and morphology of nanotubes. Nevertheless, reproducibility often remains challenging.

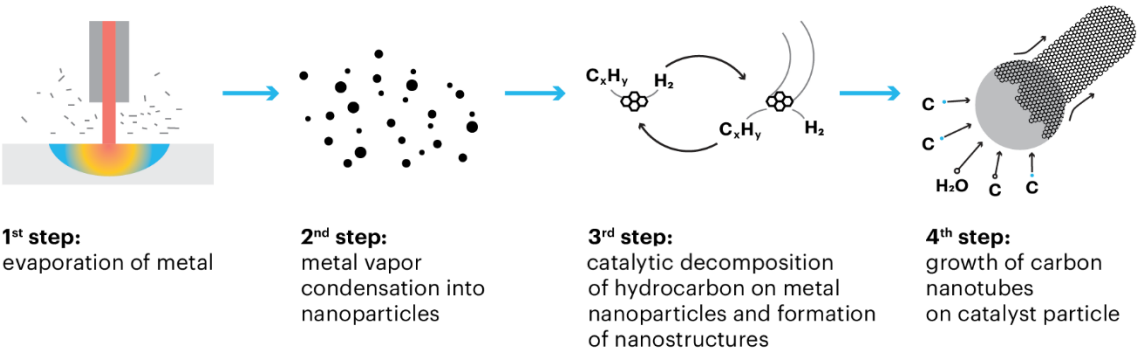

Figure 3.2.Steps in the production of CNT by CVD method

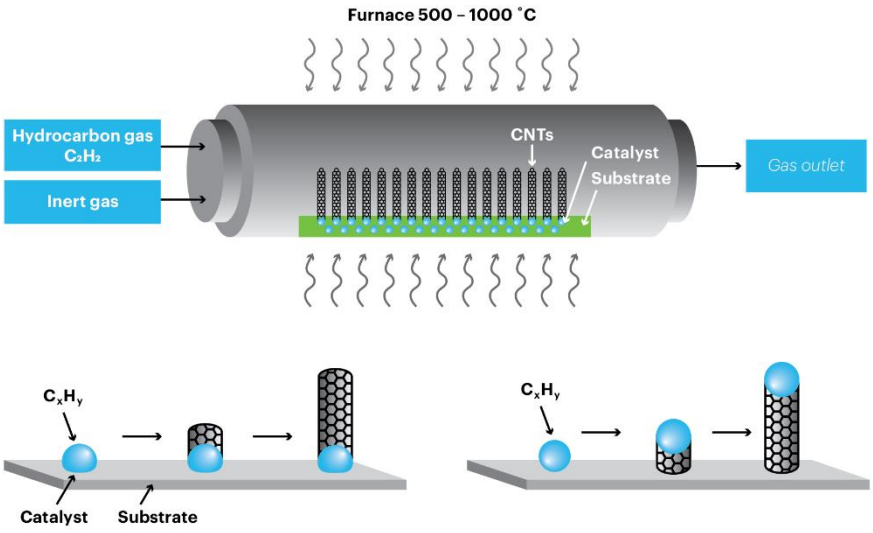

Figure 3.3.CVD production process

CH-4 TYPES OF CORES IN SANDWICH MATERIAL

4.1.NON RE-ENTRANT HONEYCOMB CORE

Natural Non re-entrant (Pointing outwards) honeycomb structures occur in many different environments, from beehives to honeycomb weathering in rocks. Based on these, man-made honeycomb structures have been built with similar geometry to allow the reduction of the quantity of material used, and thereby realizing minimal weight and material cost**.**

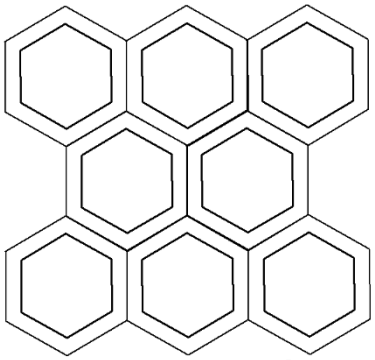

Figure 4.1.Non-re entrant honeycomb structure

Benefits of Honeycomb Composites:

The key benefits of using honeycomb composites are given below:

- Exceptional strength to weight ratio
- Corrosion resistance
- High toughness
- High temperature performance
- Easily machinable and formable
- Aluminium honeycomb provides maximum stiffness with one of the highest strength to weight ratios of any structural core material in the market.
- Kevlar™ honeycomb conforms to strict smoke, toxicity and flammability standards.

Applications:

Honeycomb materials can be used in a huge number of applications. Some of the common applications are as follows:

- Skis and snowboards
- Rocket substructure and jet aircraft
- LED technology and loudspeaker technology
- Automobile structure

- Air, water, fluid, and light directionalisation(The term directionalisation means that the directional stress is defined along each direction vector in the unit-sphere, yet the sum over all these directions should return the original stress tensor of the selected hyper-elastic model.)
- Electric shielding enclosures
- Wind turbine blades
- Clean room panels and exterior architectural curtain wall panels
- Heating, ventilation, air-conditioning equipment, and devices
- Energy absorption protective structures
- In the construction of boats for providing buoyancy that will help enhance speed
- In the rail industry for forming doors, floors, energy absorbers/bumpers, and furniture
- In the marine industry for constructing commercial vessels and naval vessel bulkheads, wall ceiling, partition panels, furniture, and several other applications

4.2.RE-ENTRANT AUXETIC HONEYCOMB CORE

An account on naturally occurring material that exhibits negative Poisson's ratio was given by Yeganeh-Haeri et al.[27] in the form of α-cristobalite, a silicon dioxide. Auxetic materials are defined as solids that possess negative Poisson's ratio. When auxetic materials are stretched in one direction, they expand in the direction transverse to the loading direction. It follows that if the load is reversed from stretching to compression, the materials contract in transverse direction.

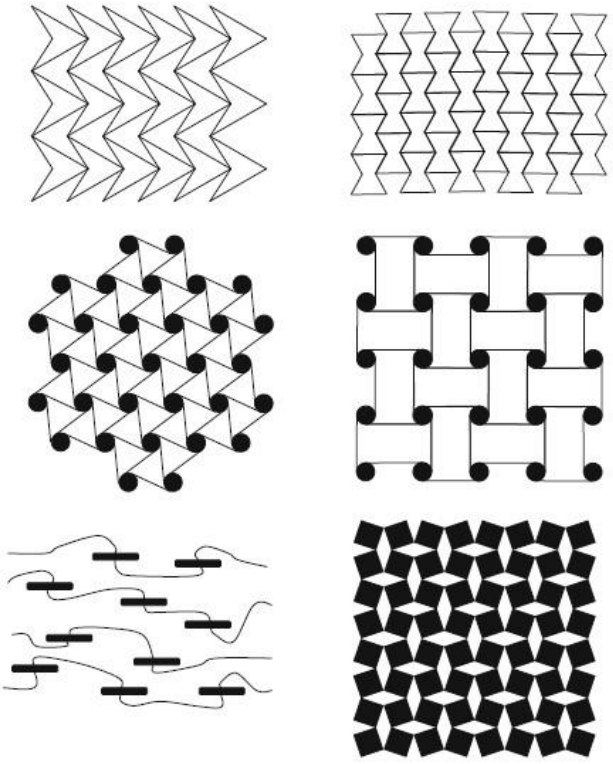

Figure 4.2.Few figures which exhibit auxetic behaviour

Benefits of Auxetic core:

Apart from the scientific value of having materials with a negative Poisson`s ration, auxetic materials show enhanced mechanical properties such as:

- increased shear stiffness
- increased plane strain fracture toughness
- increased indentation resistance

which make them superior to classical materials for many practical applications.

Application of Auxetic core:

Auxetics may be useful in applications such as

- Body armour,
- Packing material,
- Knee and elbow pads,
- Robust shock absorbing material,
- Sponge mops
- Armoured vehicle to protect from RDX blast
- Vibration isolation
- Energy absorption

4.3.AUXETIC HONEYCOMB CORE VS NON RE-ENTRANT HONEYCOMB CORE

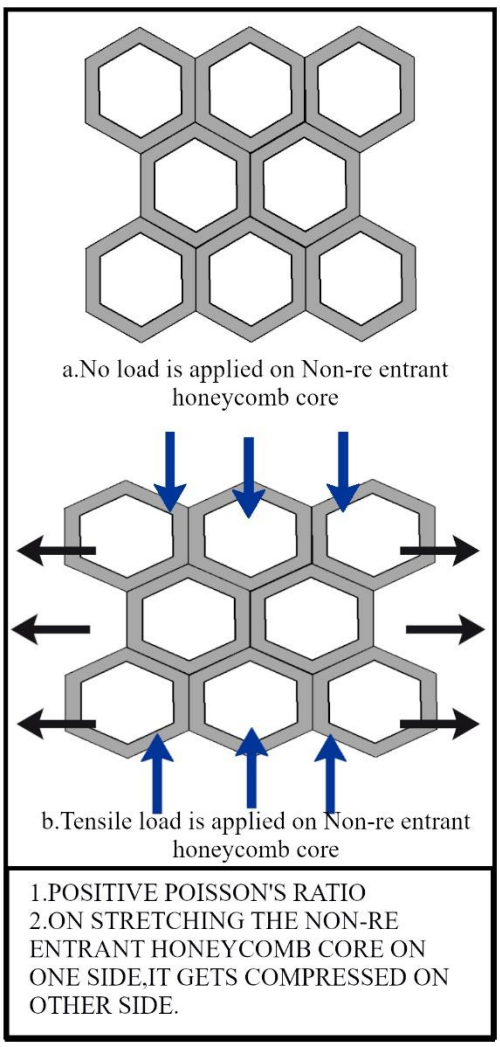

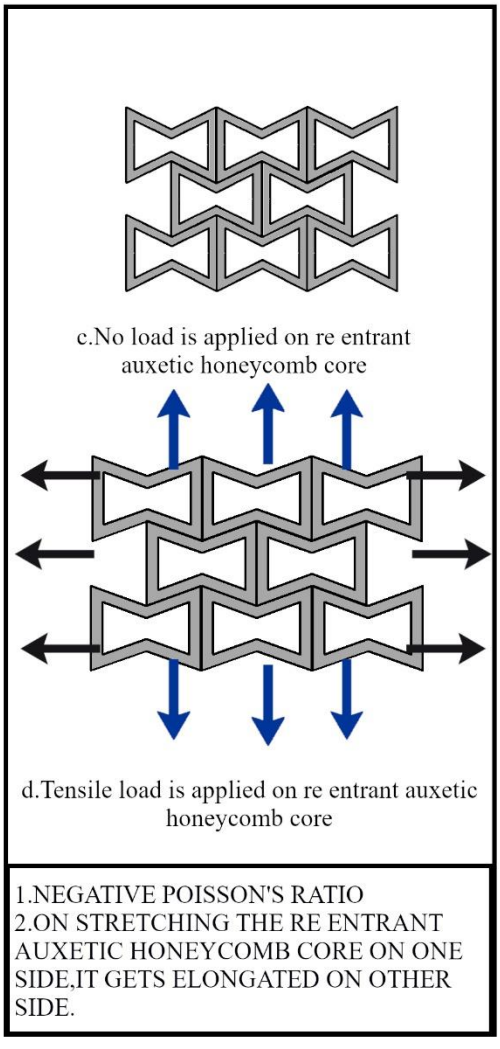

CH 5:MECHANICS OF HONEYCOMB STRUCTURES

These equations are valid for both non-re-entrant honeycomb as well as re-entrant auxetic core.(based on Lorna J. Gibson and Michael F. Ashby[28]) For re-entrant auxetic core, replace the value of θ_h with -ve θ_h.

E_a=Young's modulus of the re-entrant auxetic core or non-re-entrant honeycomb core material
G_a=Shear modulus of the re-entrant auxetic core or non re-entrant honeycomb core material
ν_a=Poisson's ratio of the re-entrant auxetic core or non re-entrant honeycomb core material
l_h=Length of re-entrant strut or slant length of strut
h_h=Length of vertical strut
t_h =Thickness of strut
θ_h = Re − entrant angle or non − re entrant honeycomb angle
θ=-θ_h for re-entrant auxetic core and θ_h for non re-entrant honeycomb core
ρ_a = Density of core material

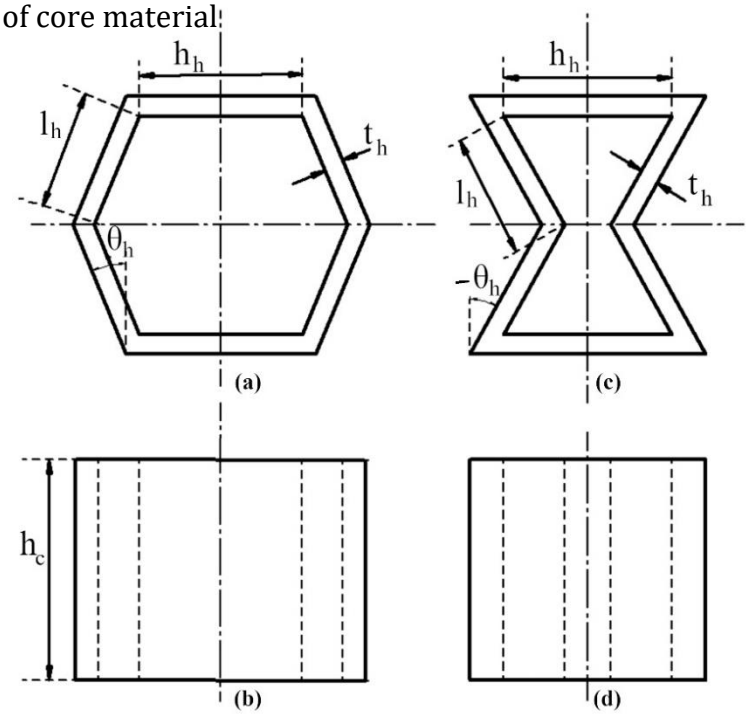

FIGURE 5.1. Honeycomb unit cell a. Top view of non re-entrant honeycomb core c. Top view of re-entrant auxetic honeycomb core b. Front view of non re-entrant honeycomb core d. Front view of re-entrant auxetic honeycomb core

5.1.DENSITY OF THE HONEYCOMB CORE

The volume of solid per cell is:- (5.1)

$$V_s = (2l_h + h_h)h_c t$$

Volume of a cell is: (5.2)

$$V_c = 2l_h \cos\theta (h_h + l_h \sin\ \theta) h_c$$

$$\text{Relative density} = \frac{\rho}{\rho_a} = \frac{\left(2+\frac{h_h}{l_h}\right)\frac{t_h}{l_h}}{2\cos\theta\left(\frac{h_h}{l_h}+\sin\theta\right)} \tag{5.3}$$

5.2. IN-PLANE PROPERTIES: YOUNG'S MODULUS,POISSON'S RATIO,SHEAR MODULUS,COEFFICENT OF THERMAL EXPANSION

i. Young's modulus

ii. Poisson's ratio

iii. Shear modulus

iv. Coefficient of thermal expansion

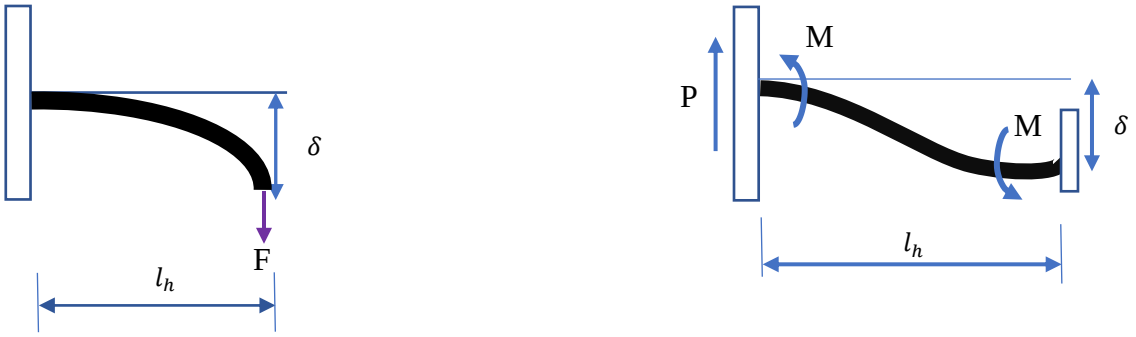

FIGURE 5.2. Strut of honeycomb is thought of Beam

$I \rightarrow$ second moment of area of the beam(strut)

- Beam with rectangular cross-section $= h_c t_h$.

$$I = \frac{h_c {t_h}^3}{12}$$

The end deflection of a cantilever beam of length l_h loaded at the end by the force ' F ' is (5.5)

$$\delta_1 = \frac{F\,{l_h}^3}{3E_a I}$$

End deflection of a beam of length ' l_h ' fixed at both to which equal but opposite loads P are applied at each end (5.6)

$$\delta_2 = \frac{P{l_h}^3}{12E_a I} = \frac{M{l_h}^2}{6E_a I}$$

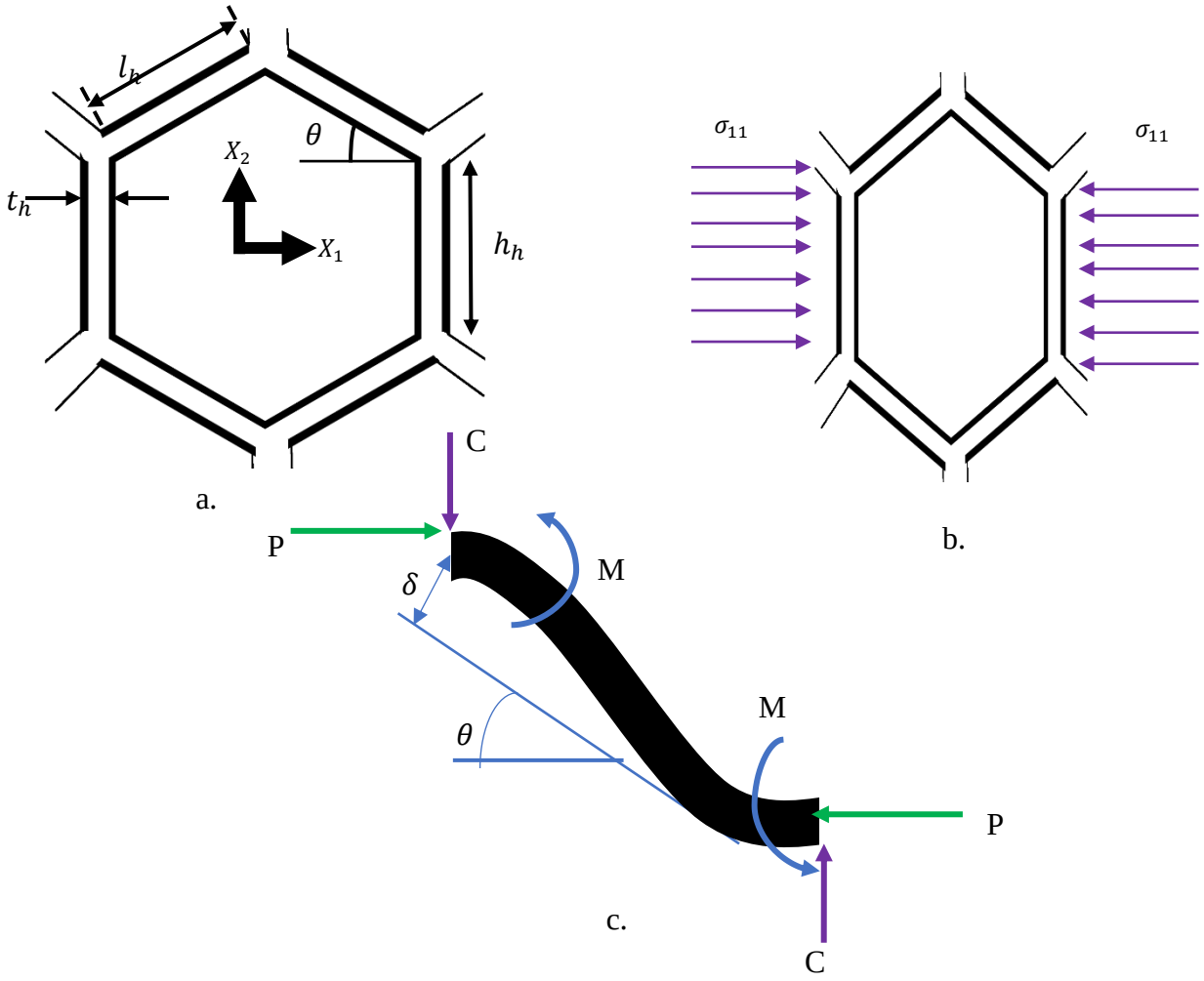

FIGURE 5.3. Cell Deformation under σ_{11}

- Consider the linear-elastic response of the structure shown in the fig 4 when subjected to the $stress, \sigma_{11}$.
- The forces acting on the cell wall of length l_h and depth b as fig 5.3(c).
- By symmetry, the force ' C ' acting on the walls of length ' h_h ' lies in the plane of the wall,
- There is no rotation of joints.
- Since (for reason of equilibrium) no net force acts across any plane through the structure which lies normal to X_2 axis, we have

$$C = 0 \tag{5.7}$$
$$M = \frac{P l_h \sin\theta}{2}$$

where, $P = \sigma_{11}(\mathrm{h_h} + l_h \sin\theta) h_c$ (5.8)

wall deflects by (5.9)

$$\delta = \frac{P{l_h}^3 \sin\theta}{12E_a I}$$

Of this, a component $\delta \sin\ \theta$ is parallel to X_1 axis, Giving a strain (5.10)

$$\varepsilon_{11} = \frac{\delta \sin\theta}{l_h \cos\theta}$$
$$= \frac{\sigma_{11}(h_h + l_h \sin\theta) h_c {l_h}^2 \sin\theta}{12\mathrm{E_a} I \cos\theta}$$

For Young's Modulus parallel to X_1 is

$$E_1 = \frac{\sigma_{11}}{\varepsilon_{11}}$$
$$= \frac{\sigma_{11} \times 12E_a I \cos\ \theta}{\sigma_{11}(h_h + l_h \sin\ \theta) h_c {l_h}^2 \sin\ \theta}$$
$$= \frac{12\mathrm{E_a}\ I \cos\ \theta}{(h_h + l_h \sin\ \theta) h_c {l_h}^2 \sin^2\theta} \qquad \left[I = \frac{h_c {t_h}^3}{12}\right]$$
$$= \frac{12E_a \times \frac{h_c {t_h}^3}{12} \cos\theta}{(h_h + l_h \sin\ \theta) h_c {l_h}^2 \sin^2\theta}$$

$$\frac{E_1}{E_a} = \left(\frac{t_h}{l_h}\right)^3 \frac{\cos\theta}{\left(\frac{h_h}{l_h} + \sin\theta\right)\sin^2\theta} \quad (5.11)$$

Strain along $X_2\ axis$ axis, (5.12)

$$\varepsilon_{22} = \frac{-\delta \cos\ (\theta)}{(h_h + l_h \sin\ \theta)}$$

$$v_{12} = -\frac{\varepsilon_{22}}{\varepsilon_{11}} = \frac{l_h \cos^2\theta}{(h_h + l_h \sin\theta)\sin\theta} \quad (5.13)$$

from which Poisson's ratio for loading the X_1 direction w.r.t to X_2 (5.14)

$$\vartheta_{12} = \frac{\cos^2 \theta}{\left(\frac{h_h}{l_h}+\sin \theta\right)\sin \theta}$$

Loading in the X_2 direction

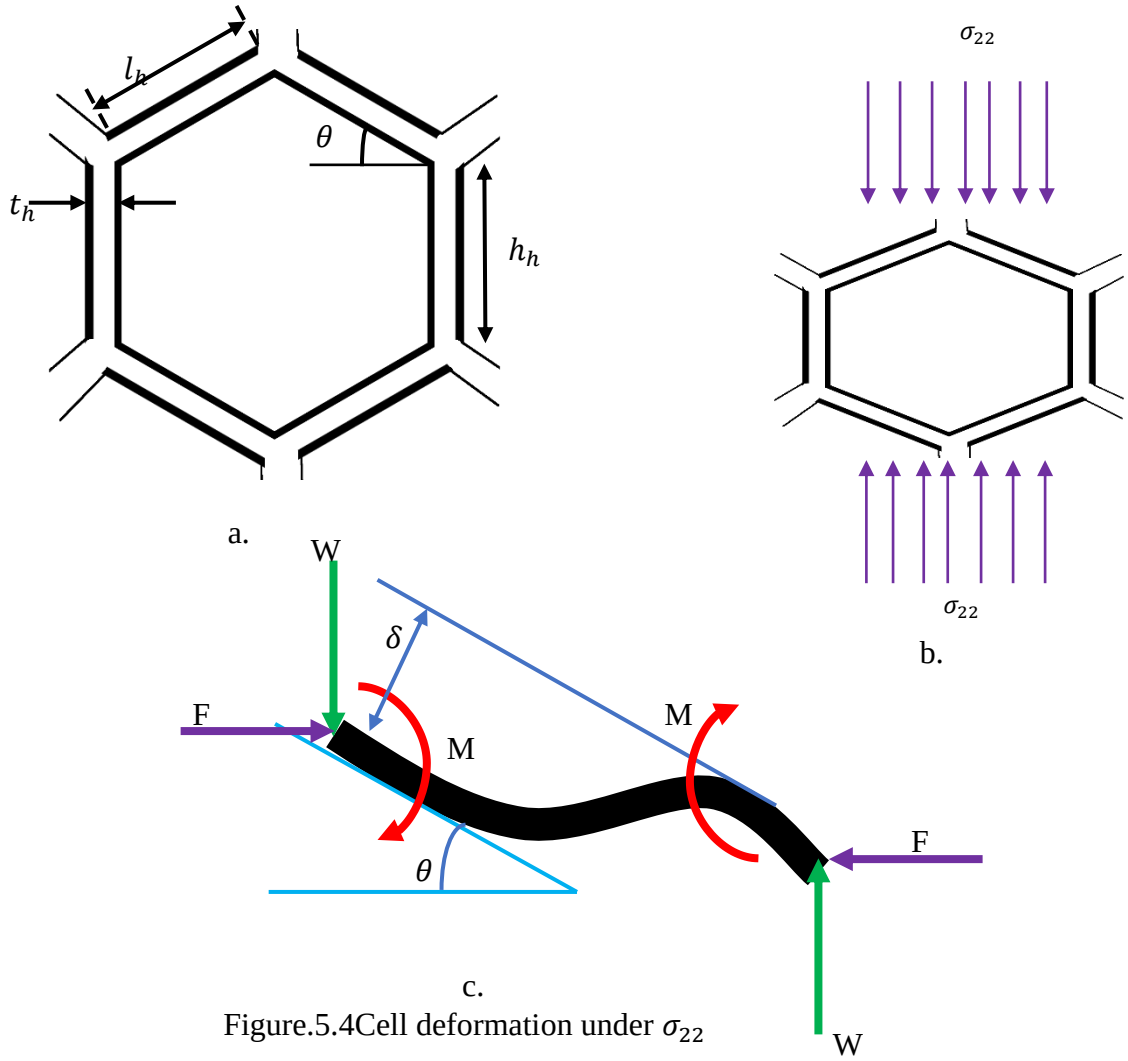

Figure.5.4Cell deformation under σ_{22}

As before, symmetry requires that the forces in the walls of length h_h lie in the plane of the walls, and there is no rotation of the joints. By equilibrium,

$$F = 0$$
$$W = \sigma_{22} l_h h_c \cos\theta \quad (5.15)$$

The wall deflects by , (5.16)

$$\delta = \frac{W {l_h}^3 \cos\theta}{12 E_a I}$$

Of this, a component $\delta\cos\theta_h$ is parallel to the X_2 axis, giving a strain:

$$\varepsilon_{22} = \frac{\delta\cos\theta}{(h_h + l_h\sin\theta)}$$

$$\Rightarrow \quad \varepsilon_{22} = \frac{\sigma_{22} h_c {l_h}^4 \cos^3\theta}{12 \mathrm{E}_a \mathrm{I}\,(h_h + l_h\sin\theta)} \tag{5.17}$$

- from which Young's Modulus parallel to the X_2 axis is:-

$$\mathrm{E}_2 = \frac{\sigma_{22}}{\varepsilon_{22}} = \frac{12 E_a I (h_h + l_h\sin\theta)}{h_c {l_h}^4 \cos^3\theta} \qquad \left[I = \frac{h_c {t_h}^3}{12}\right]$$

$$= \frac{12 \times E_a \times \frac{h_c {t_h}^3}{12} \times (h_h + l_h\sin\theta)}{h_c {l_h}^4 \cos^3\theta}$$

$$\Rightarrow \quad \boxed{\frac{E_2}{E_a} = \left(\frac{t_h}{l_h}\right)^3 \frac{\left[\frac{h_h}{l_h} + \sin\theta\right]}{\cos^3\theta}} \tag{5.18}$$

The strain parallel to the X_1 axis is

$$\varepsilon_{11} = -\frac{\delta\sin\theta}{l_h\cos\theta} \tag{5.19}$$

- Poisson's ratio for loading in X_2 direction w.r.t X_1,

$$v_{21} = -\frac{\varepsilon_{11}}{\varepsilon_{22}}$$

$$\Rightarrow \quad v_{21} = \frac{(h_h + l_h\sin\theta)\sin\theta}{l_h\cos^2\theta} \tag{5.20}$$

$$\boxed{\vartheta_{21} = \frac{\left(\frac{h_h}{l_h} + \sin\theta\right)\sin\theta}{\cos^2\theta}} \tag{5.21}$$

Shear Force in X_1 and X_2 plane

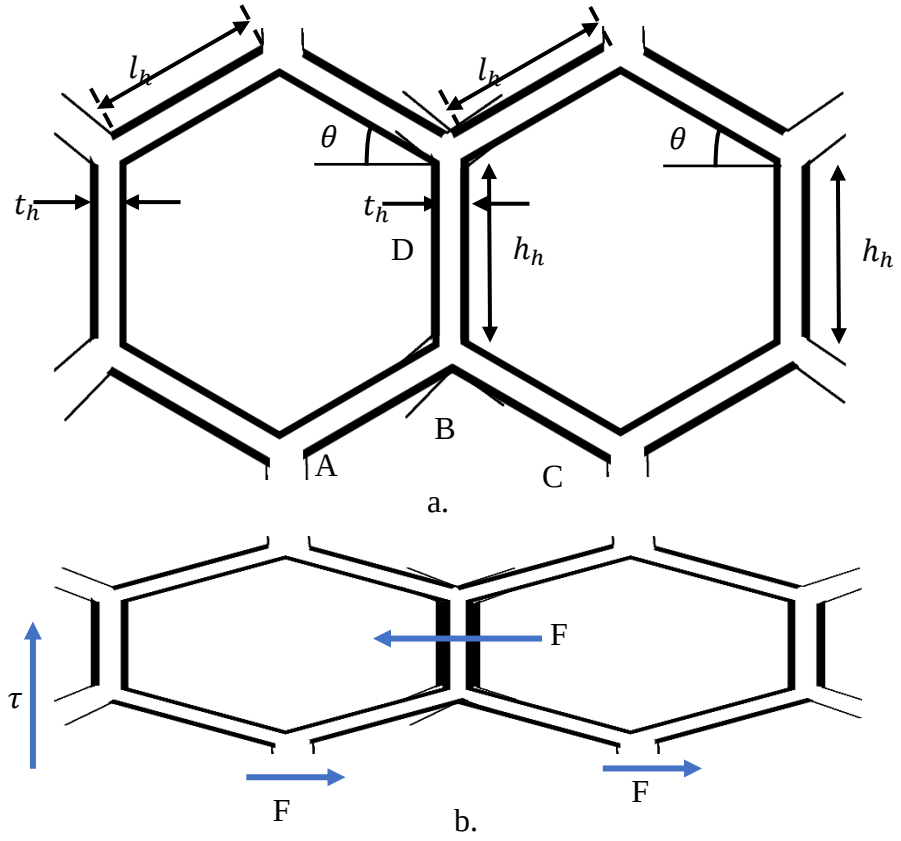

Figure 5.5.Cell Deformation under Shear stress

Consider the elastic deformation of the cellular structure when shear stress is applied such that force acting on it in fig.5.5(b)

By symmetry, there is no relative motion of the points A,B,C and forces in the members are shown in the fig.5.5

Summing moment at B, we find the moment applied to the members AB and BC is:-

$M=Fh_h/4$

$$\Rightarrow \quad \delta_2 = l_h\phi = \frac{M{l_h}^2}{6E_aI}$$
$$= \frac{Fh_h}{4} \times \frac{{l_h}^2}{6E_aI} = \frac{Fh_h{l_h}^2}{24E_aI}$$
$$\phi = \frac{Fh_hl_h}{24E_aI} \tag{5.22}$$

The Shearing deflection (U_s) of the point D w.r.t ' B ' is

$$U_S = \phi\frac{\mathrm{h_h}}{2} + \frac{F(\frac{h_h}{2})^3}{3E_aI}$$
$$U_S = \frac{F{h_h}^2l_h}{48E_aI} + \frac{F{h_h}^3}{24E_aI}$$
$$\Rightarrow U_S = \frac{F{h_h}^2}{48E_aI}(l_h + 2h_h) \tag{5.23}$$

Shear strain, γ_{12} is given by

$$\gamma_{12} = \frac{U_s}{\left(\frac{h_h}{2} + \frac{l_h}{2}\sin\theta\right)}$$
$$\Rightarrow \gamma_{12} = \frac{2U_s}{(h_h + l_h\sin\theta)}$$
$$\Rightarrow \gamma_{12} = 2 \times \frac{F{h_h}^2(l_h + 2h_h)}{48E_aI} \times \frac{1}{(h_h + l_h\sin\theta)}$$
$$\Rightarrow \gamma_{12} = \frac{F{h_h}^2}{24E_aI}\left[\frac{(l_h + 2h_h)}{(h_h + l_h\sin\theta)}\right] \tag{5.24}$$

Distance shear stress, $\tau_{12} = \frac{F}{2(h_cl_h\cos\theta)}$ (5.25)

- Shear modulus of Rigidity of Honeycomb
  Here G_{12},G_{23},G_{13} is derived.
  First, we will derive G_{12} by using the shear stress and shear strain which we have derived.
- G_{12}:-

$$G_{12} = \frac{\tau_{12}}{\gamma_{12}} = \frac{F}{2l_h h_c \cos\theta} \times \frac{24E_a \mathrm{I}(h_h + l_h \sin\theta)}{F {h_h}^2 (l_h + 2h_h)}$$

$$= \frac{12E_a \mathrm{I}(h_h + l_h \sin\theta)}{h_c {h_h}^2 l_h \cos\theta (l_h + 2h_h)}$$

$$= \frac{\mathrm{E}_a \ {t_h}^3 (h_h + l_h \sin\theta)}{{h_h}^2 l_h \cos\theta (l_h + 2h_h)}$$

$$= \mathrm{E_a} \frac{{t_h}^3}{{h_h}^2 l_h} \times \frac{l_h [h_h / l_h + \sin\theta]}{\cos\theta \times l_h \left(1 + \frac{2h_h}{l_h}\right)}$$

$$= \frac{\mathrm{E_a} \ {t_h}^3}{{h_h}^2 {l_h}^2} \frac{l_h \left[\frac{h_h}{l_h} + \sin\theta\right]}{\cos\theta \left(1 + \frac{2h_h}{l_h}\right)}$$

$$\Rightarrow G_{12} = \frac{E_a}{\left(\frac{{h_h}^2}{{l_h}^2}\right)} \frac{{t_h}^3}{{l_h}^3} \frac{\left[\frac{h_h}{l_h} + \sin\theta\right]}{\cos\theta \left[1 + \frac{2h_h}{l_h}\right]}$$

$$\boxed{G_{12} = \frac{E_a}{\left(\frac{{h_h}^2}{{l_h}^2}\right)} \frac{{t_h}^3}{{l_h}^3} \frac{\left[\frac{h_h}{l_h} + \sin\theta\right]}{\cos\theta \left[1 + \frac{2h_h}{l_h}\right]}} \quad (5.26)$$

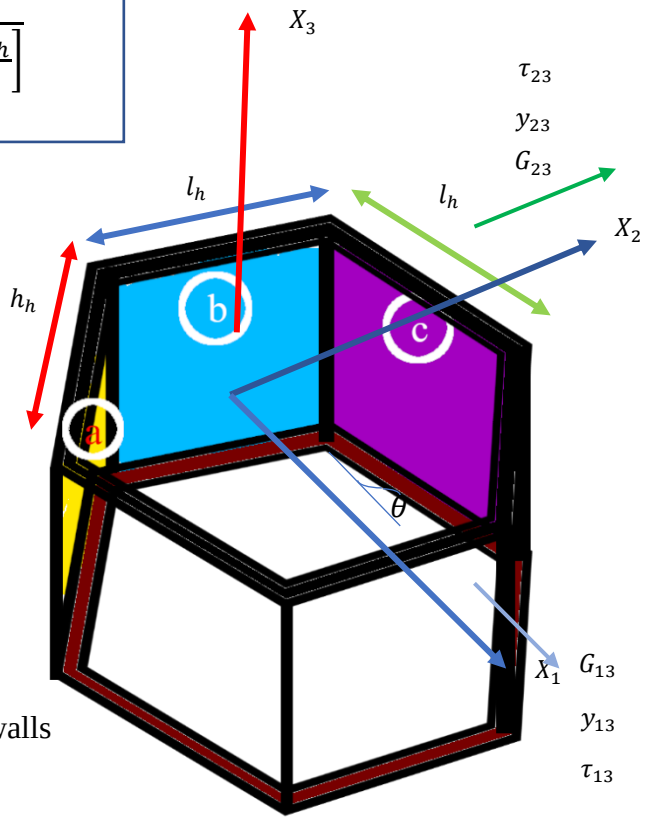

Fig 5.6.Shear force on cell walls

■Consider a uniform shear, γ_{13}, caused by a shear stress τ_{13} acting on the face normal to X_3 in the X_1 direction in fig. 5.6.

■Isolate a unit-element of the honeycomb structure, as shown, which repeats exactly to build up the entire honeycomb.

■Almost all the elastic strain energy is stored in the shear displacements in the cell walls; the bending stiffness & energies associated with bending are much smaller.

❖ G13:-

The shear strains in the wall a, b, c are

$$\gamma_a = 0$$
$$\gamma_b = \gamma_{13}\cos\theta$$
$$\gamma_c = \gamma_{13}\cos\theta$$

By first theorem, for shear in the X_1 direction,

$$\frac{1}{2}G_{13}\gamma_{13}{}^2V \leqslant \frac{1}{2}\sum_i (G_s\gamma_i{}^2V_i)$$

Where G_s is the shear modulus of the cell material,

$\gamma_i =$ shear strains in the three cell walls

Summation is carried out over the three cell walls a, b, c of volume V_a, V_b, V_c

$$\frac{1}{2}\sum_i G_a\gamma_i{}^2v_i$$
$$= \frac{1}{2}\left[G_a \times 0 \times V_a + G_a\gamma_{13}{}^2\cos^2\theta V_b + G_a\gamma_{13}{}^2\cos^2\theta \underline{V_b}\right]$$
$$\because \quad Vc = V_b$$
$$= \frac{1}{2}[2G_a\gamma_{13}{}^2V_b\cos^2\theta] = \frac{1}{2}[2G_a\gamma_{13}^2 l_h t_h h_c\cos^2\theta]$$

$V =$ Total volume of the honeycomb (cross section)

$$= \left[\frac{1}{2}[h_h + (h_h + 2l_h\sin\theta)][l_h\cos\theta\ h_c] \times 2\right.$$
$$= 2[h_h + l_h\sin\ \theta]l_h\cos\theta h_c$$
$$\frac{1}{2}G_{13}\gamma_{13}{}^2 \times 2[h_h + l_h\sin\theta]l_h\cos\theta h_c \leqslant \frac{1}{2}[2G_a\gamma_{13}^2 l_h t_h h_c\cos^2\theta]$$
$$\Rightarrow G_{13} \leq \frac{G_a t_h\cos\theta}{(h_h + l_h\sin\theta)} \Rightarrow G_{13} \leq \left(\frac{t_h}{l_h}\right)\frac{\cos\theta}{\left(\frac{h_h}{l_h} + \sin\theta\right)} \qquad (5.27)$$

The second theorem gives the lower bound for the moduli. It states, that, among the stress distributions that satisfy equilibrium at each point and are in equilibrium with external loads, the strain energy of minimum for the exact stress distribution.

For shear in X_1 direction,

$$\frac{1}{2}\frac{\tau_{13}^2}{G_{13}}V \leqslant \frac{1}{2}\sum_i \frac{\tau_i^2}{G_a}V_i$$

consider, first, loading in the X_1 direction. We postulate that external stress τ_{13} induces a set of shear stresses τ_a, τ_b, τ_c in the three cells.

by symmetry, $\tau_b = \tau_c$ and as the wall ' a ' is loaded in simple bending, it carries no significant load.

$\tau_a = 0$

Equilibrium requires,

$\tau_{13} \times$ [area of honeycomb] = [shear force on a + shear force on b +shear force on C] along one direction

$$\Rightarrow \tau_{13} \times 2 \times \frac{1}{2} \times [h_h + h_h + 2l_h\sin\theta] \times l\cos\theta = 0 + \tau_b t_h l_h \cos\theta + \tau_b l_h t_h \cos\theta$$
$$\Rightarrow 2\tau_{13}[h_h + l_h\sin\theta]l_h\cos\theta = 2\tau_b t_h l_h \cos\theta$$
$$\Rightarrow \tau_{13} = \frac{\tau_b t_h}{(h_h + l_h\sin\theta)} \tag{5.28}$$

$$\frac{1}{2} \times \frac{\tau_{13}^2}{\mathrm{G}_{13}} \times V \leqslant \frac{1}{2}\sum_i \frac{\tau_{\mathrm{i}}^2}{\mathrm{G_a}}V_i$$
$$\Rightarrow \frac{1}{2} \times \frac{{\tau_{13}}^2}{G_{13}} \times 2[h_h + l_h\sin\theta]l_h\cos\theta h_c \leq \frac{1}{2}\frac{\tau_b^2}{G_a}\ l_h \mathrm{b} t_h + \frac{1}{2}\frac{\tau_c^2}{G_a} l_h h_c t_h$$

$because\ \tau_a = 0\ \ \&\ \ \tau_c = \tau_b$

$$\Rightarrow \frac{1}{2}\frac{\tau_{13}^2}{G_{13}} 2[h_h + l_h\sin\theta]l\cos\theta h_c \leqslant \frac{1}{2}\left(\frac{2\tau_b^2 l_h h_c t_h}{\mathrm{G_a}}\right)$$
$$\Rightarrow \frac{G_{13}}{\mathrm{G}_a} \geqslant \frac{[h_h + l_h\sin\theta]\cos\theta}{t_h}\left(\frac{\tau_{13}}{\tau_b}\right)^2$$
$$\Rightarrow \frac{G_{13}}{\mathrm{G}_a} \geqslant \left[\frac{h_h + l_h\sin\theta}{t_h}\right]\cos\theta\ \left(\frac{t_h}{h_h + l_h\sin\theta}\right)^2$$
$$\Rightarrow \frac{G_{13}}{G_{\mathrm{a}}} \geqslant \frac{\cos\theta}{\left(\frac{h_h}{l_h} + \sin\theta\right)}\frac{t_h}{l_h} \tag{5.29}$$
$$\Rightarrow \frac{\cos\theta}{\left(\frac{h_h}{l_h} + \sin\theta\right)}\left(\frac{t_h}{l_h}\right) \leqslant \frac{\mathrm{G}_{13}}{G_{\mathrm{a}}} \leqslant \frac{\cos\theta}{\left(\frac{h_h}{l_h} + \sin\theta\right)}\left(\frac{t_h}{l_h}\right) \tag{5.30}$$

Now from second theorem, (5.31)

so, only equality holds.

$$\frac{G_{13}}{G_a} = \frac{\cos\theta}{\left(\frac{h_h}{l_h}+\sin\theta\right)}\left(\frac{t_h}{l_h}\right)$$

G_{23}: Maximum & Minimum value along X_2 direction,

$$\left.\begin{aligned}\gamma_a &= \gamma_{23}\\ \gamma_b &= \gamma_{23}\sin\theta\\ \gamma_b &= \gamma_{23}\sin\theta\end{aligned}\right\}$$

Applying first theorem,

$$\frac{1}{2}G_{23}\gamma_{23}^2 V \leqslant \frac{1}{2}\sum_i G_a\gamma_i^2 V_i$$

$$\Rightarrow \frac{1}{2}G_{23}\gamma_{23}{}^2 \times 2[h_h + l_h\sin\theta]l_h\cos\theta h_c$$

$$\leq \frac{G_a}{2}[y_{23}^2 h_h t_h h_c + \gamma_{23}^2 l_h t_h h_c\sin^2\theta + y_{23}^2\sin^2\theta l_h t_h h_c]$$

$$\leqslant \frac{G_a}{2}y_{23}^2 t_h h_c[h_h + 2l_h\sin^2\theta]$$

$$\Rightarrow G_{23} \leqslant \frac{G_a t_h}{2}\frac{[h_h + 2l_h\sin^2\theta]}{[h_h + l_h\sin\theta]l_h\cos\theta}$$

$$\Rightarrow \frac{G_{23}}{G_a} \leqq \frac{1}{2}\left(\frac{t_h}{l_h}\right)\frac{\left[\frac{h_h}{l_h} + 2\sin^2\theta\right]}{\left[\frac{h_h}{l_h} + \sin\theta\right]\cos\theta}$$

$$\Rightarrow \quad \frac{G_{23}}{G_a} \leqslant \frac{1}{2}\left(\frac{t_h}{l_h}\right)\frac{\left[\frac{h_h}{l_h} + 2\sin^2\theta\right]}{\left[\frac{h_h}{l_h} + \sin\theta\right]cos\theta} \qquad (5.32)$$

Applying 2nd theorem & equilibrium equation,

$\tau_b = \tau_c$ (By symmetry)

equilibrium in X_3 direction,

$$\tau_{a=}\tau_{b+}\tau_c = 2\tau_b \qquad (5.33)$$

equilibrium of external stress,

$$2\tau_{23} l_h (h_h + l_h \sin\theta)\cos\theta = 2\tau_b t_h l_h \sin\theta + \tau_a\, t_h h_h \tag{5.34}$$

So that, $\tau_{\mathrm{b}} = \tau_{23} \cos\theta \frac{l_h}{t}$

Putting in 2nd theorem,

$$\frac{1}{2}\frac{\tau_{23}^2}{\mathrm{G}_{23}}\mathrm{V} \leqslant \frac{1}{2}\sum_i \frac{\tau_l^2}{G_a} V_i$$

$$\frac{G_{23}}{\mathrm{G_a}} \geqslant \frac{\left(\frac{h_h}{l_h} + \sin\theta\right)}{\left(1 + \frac{2\mathrm{h}_h}{l_h}\right)\cos\theta}\left(\frac{t_h}{l}\right)$$

$$\frac{t_h}{l_h}\frac{\left(\frac{h_h}{l_h} + \sin\theta\right)}{\left(\frac{2h_h}{l_h} + 1\right)\cos\theta} \leqslant \frac{G_{23}}{G_a} \leqslant \frac{1}{2}\frac{\left(\frac{h_h}{l_h} + 2\sin^2\theta\right)}{\left(\frac{h_h}{l_h} + \sin\theta\right)\cos\theta}\left(\frac{t_h}{l_h}\right) \tag{5.35}$$

The lengths of the honeycomb unit cell at the middle is given by, $X_{2T} = 2l_h \sin(\theta)$ $X_{1T} = 2h_h \pm 2l_h \cos(\theta)$	+ve for non re-entrant honeycomb core -ve for re-entrant auxetic honeycomb core
The coefficients of thermal expansion , $\alpha_h = coefficient\ of\ thermal\ expansion\ along\ vertical\ strut$ $\alpha_l = coefficient\ of\ thermal\ expansion\ along\ re-entrant\ strut$ $\alpha_h = \frac{1}{h_h}(\frac{\partial h_h}{\partial T})_p = \alpha_m$ (5.36) $\alpha_l = \frac{1}{l_h}(\frac{\partial l_h}{\partial T})_p = (\frac{h_h}{l_h \cos\theta})\alpha_h$ (5.37)	
$\alpha_1 = \frac{1}{X_{1T}}(\frac{dX_{1T}}{dT})_p = \frac{h_h\alpha_h \pm l_h \cos(\theta)\alpha_l}{h_h \pm l_h \cos(\theta)} = \frac{(h_h/l_h)\alpha_h \pm \cos(\theta)\alpha_l}{(h_h/l_h) \pm \cos(\theta)}$ (5.38) $\alpha_2 = \frac{1}{X_{2T}}(\frac{dX_{2T}}{dT})_p = \alpha_l$ (5.39)	

CH 6: THEORITICAL FORMULATION:HIGHER ORDER SHEAR DEFORMATION (HSDT)FINITE ELEMENT METHOD

6.1 INTRODUCTION

This chapter contains the theoretical formulation and solution procedures for dynamic analysis of the rotating pre-twisted composite sandwich plate. At first, the sandwich plate model along with the geometrical features is introduced. A higher-order shear deformation theory is employed to define the displacement field within the sandwich plate. Afterward, stress resultants acting on the composite sandwich plate are derived from the stress-strain relationship considering the thermal effect. The entire planform of the sandwich plate is then discretized into eight-node iso-parametric plate element and the relevant finite element formulation for the present analysis is developed. The general dynamic equilibrium equation of the rotating plate is formulated using the Lagrange's equation of motion. The solution of the standard eigen value problem is obtained by using QR iteration scheme to compute the natural frequencies. Then results of the first mode and the second mode of frequencies of the sandwich plate is computed.

6.2 BASIC EQUATIONS

In this section, the basic equations are derived for sandwich plates with nanocomposite face sheets assuming a higher-order displacement field. After evaluating the strain components, the stress-strain relationship is presented considering the thermal effect.

6.2.1 SANDWICH PLATE MODEL

Consider an untwisted sandwich plate as depicted in **Fig. 6.1(a)**. The span length, width thicknesses of core and facings of the sandwich plate are indicated by a, b, and h_c and h_f, respectively. Accordingly, the overall thickness of the sandwich panel is $h = h_c + h_f$. The pre-twisted sandwich plate having reference width b is fixed at the periphery of a stiff hub of radius r_{HUB} rotating with a rotational speed Ω about z −axis as depicted in **Fig. 6.1 (b)**.

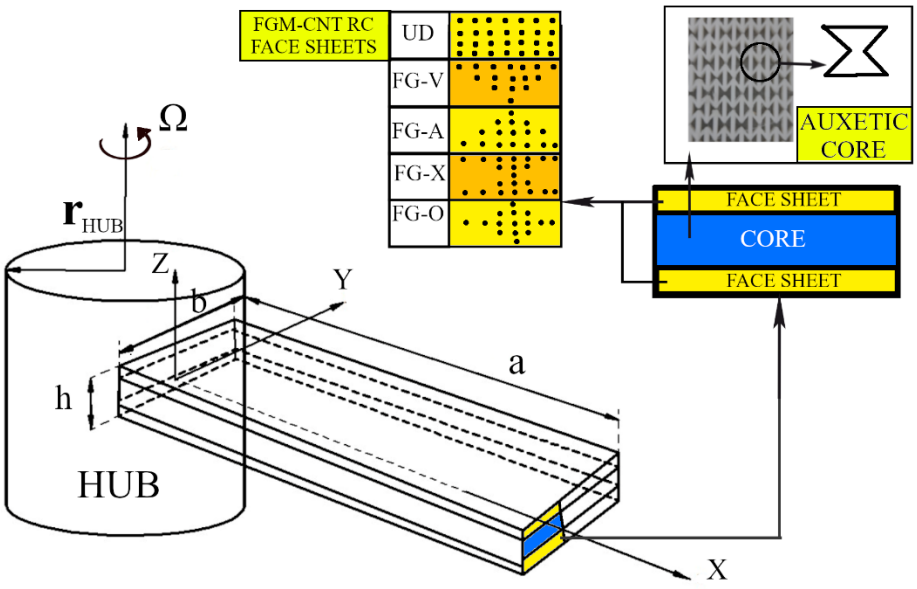

(a)

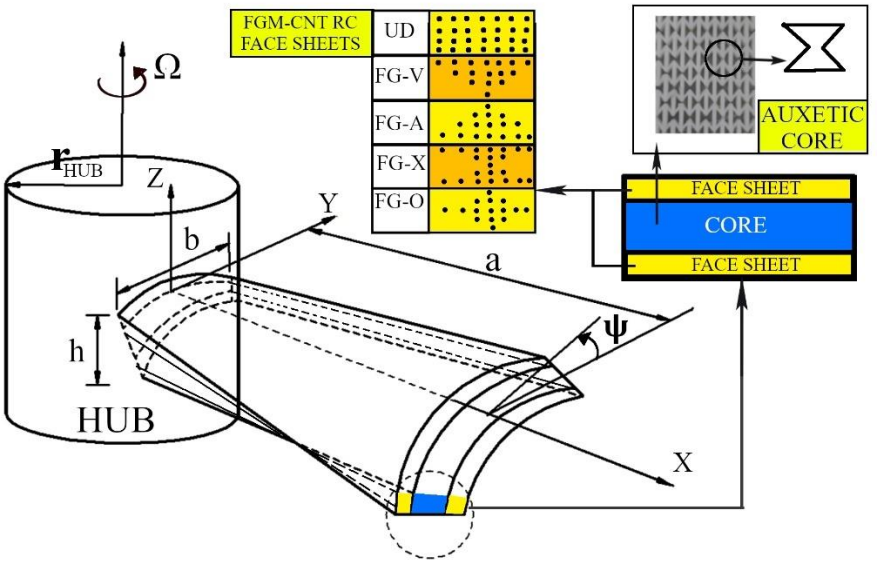

(b)

Fig. 6.1 Schematic diagram of sandwich plate model: (a) untwisted plate and (b) pre-twisted sandwich plate mounted on a rotating hub

According to Leissa *et al*. [29], the mid-surface of any pre-twisted sandwich plate is characterized by

$$z = -\frac{1}{2}\left\{\frac{x^2}{r_x} + \frac{2xy}{r_{xy}} + \frac{y^2}{r_y}\right\} \tag{6.1}$$

where r_x and r_y are the curvature radii in *x* and *y*-directions, respectively, and r_{xy} is the pretwist radius. For a sandwich plate, r_x is infinity ($r_x = \infty$), while r_y is infinity($r_y = \infty$).

The pre-twist radius of curvature (r_{xy}) can be expressed as

$$r_{xy} = -\frac{a}{\tan\psi} \tag{6.2}$$

6.2.2 NANOCOMPOSITE FACE SHEET LAYERS

One type of nanocomposite face sheets are considered to be bonded with a homogeneous core to obtain the sandwich plate. These are CNTs-reinforced composite (CNTRC) face sheets .

CNTRC Face Sheets

The CNTRC face sheets are obtained by reinforcing the (10, 10) single-walled carbon nanotubes (SWCNTs) into a polymeric matrix. The SWCNTs are considered to align with span length and distributed either uniformly (UD) or functionally graded (FG) along its thickness direction. Five different types of CNTs distribution patterns, namely FG-UU, FG-VΛ, FG-ΛV, FG-OO, and FG-XX, are considered in the sandwich plate, as shown schematically in **Fig. 6.2**. The CNTs distribution functions across the thickness of both top and bottom face sheets for these five different patterns are given in **Table 6.1,** wherein the total volume fraction of CNTs is expressed as

$$V_{CNT}^{*} = \frac{w_{CNT}}{w_{CNT} + \frac{\rho^{CNT}}{\rho^{m}} - \frac{\rho^{CNT}}{\rho^{m}} w_{CNT}} \tag{6.3}$$

in which w_{CNT} and ρ^{CNT} are mass fraction and mass density of the CNTs, respectively, whereas ρ^{m} is the mass density of matrix.

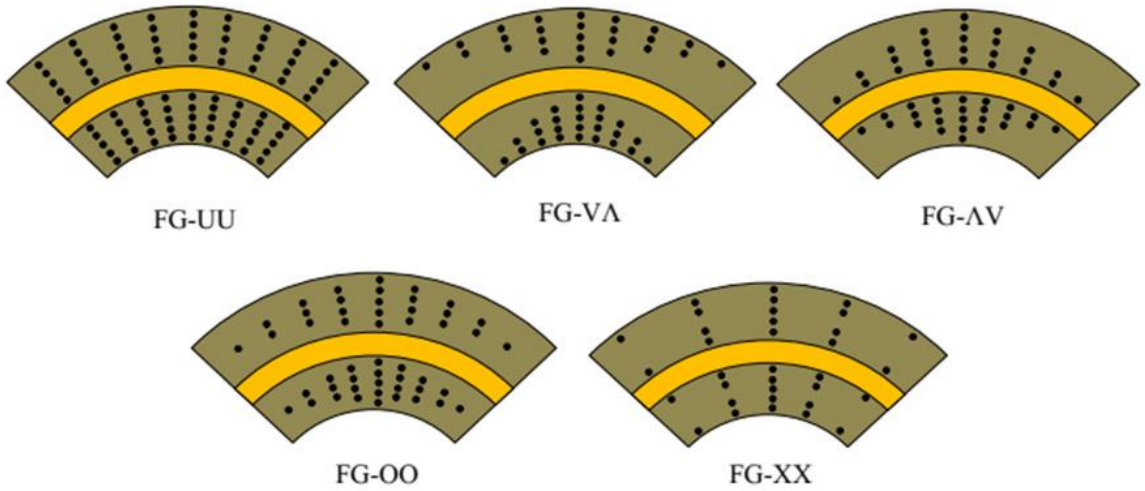

Fig. 6.2 Types of CNTs distribution patterns in sandwich plate

In FG-UU type of grading profile, the CNTs volume fraction is uniform along its thickness direction for both CNTRC face sheets. In FG-VΛ type, the outermost surfaces of both face sheets contain maximum proportions of CNTs, while innermost surfaces neighbouring to the core are free of CNTs. Besides, FG-ΛV type possesses a completely reverse distribution pattern of CNTs, i.e., outermost and innermost layers of the face sheets are free of CNTs and enriched with maximum proportions of CNTs, respectively. In FG-OO type, outermost and innermost layers of both face sheets are free of CNTs, whereas middle layers of the face sheets contain maximum proportions of CNTs. In FG-XX type, the outermost and innermost layers of the face sheets possess maximum proportions of CNTs, and the mid-surface layers of the face sheets are free of CNTs.

The effective elastic moduli of the CNTRC face sheets can be estimated using the extended rule of mixture (EROM) given as (Shen, 2009[30])

$$E_{11} = \eta_1 V_{CNT} E_{11}^{CNT} + V_m E^m \tag{6.4}$$

$$\frac{\eta_2}{E_{22}} = \frac{V_{CNT}}{E_{22}^{CNT}} + \frac{V_m}{E^m} \tag{6.5}$$

$$\frac{\eta_3}{G_{12}} = \frac{V_{CNT}}{G_{12}^{CNT}} + \frac{V_m}{G^m} \tag{6.6}$$

In the above expressions, E_{11}^{CNT}, E_{22}^{CNT}, and G_{12}^{CNT} are Young's and shear moduli of SWCNTs, respectively, while E^m and G^m signify the corresponding elastic moduli of the polymeric matrix.

Table 6.1 Volume fractions of CNTs for different distribution patterns

CNTs grading profiles	V_{CNT}	
	Top face sheet	Bottom face sheet
FG-UD	V_{CNT}^{*}	V_{CNT}^{*}

FG-V	$2V_{CNT}^{*}\left(\frac{2z-h_c}{h_f}\right)$	$-2V_{CNT}^{*}\left(\frac{2z+h_c}{h_f}\right)$
FG-Λ	$2V_{CNT}^{*}\left(\frac{h_c+h_f-2z}{h_f}\right)$	$2V_{CNT}^{*}\left(\frac{h_c+h_f+2z}{h_f}\right)$
FG-O	$2V_{CNT}^{*}\left(1-\left\|\frac{4z-2h_c-h_f}{h_f}\right\|\right)$	$2V_{CNT}^{*}\left(1-\left\|\frac{4z+2h_c+h_f}{h_f}\right\|\right)$
FG-X	$2V_{CNT}^{*}\left\|\frac{4z-2h_c-h_f}{h_f}\right\|$	$2V_{CNT}^{*}\left\|\frac{4z+2h_c+h_f}{h_f}\right\|$

Since the load transfer between the CNTs and polymeric matrix is not perfect (Qian et al., [31]; Seidel and Lagoudas,[32], the terms $\eta_i(i=1,2,3)$ known as efficiency parameters are introduced into **Eqs. (6.4)-(6.6)** to capture the size-dependent material properties. The efficiency parameters are estimated by matching the values of the elastic moduli of CNTRCs computed using EROM with corresponding values obtained from the molecular dynamics (MD) simulation (Shen,[29]). Furthermore, V_{CNT} and V_m denote the volume fractions of CNTs and matrix, respectively, and are interrelated as

$$V_{CNT}+V_m=1 \tag{6.7}$$

It is assumed that the material properties of CNTs and polymeric matrix are dependent on temperature change. Therefore, effective material properties of CNTRCs like Young's and shear moduli and thermal expansion coefficients are dependent on the temperature change and thickness coordinate. Besides, the Poisson's ratio depends weakly on temperature change and thickness coordinate and can be given as

$$\nu_{12}=V_{CNT}\nu_{12}^{CNT}+V_m\nu^m \tag{6.8}$$

where ν_{12}^{CNT} and ν_{12}^{m} signify Poisson's ratios of the SWCNTs and matrix, respectively.

The effective mass density ρ of the CNTRC layers is determined using a conventional rule of mixture (ROM) given as

$$\rho=V_{CNT}\rho^{CNT}+V_m\rho^m \tag{6.9}$$

The longitudinal and transverse thermal expansion coefficients of the CNTRCs can be expressed as

$$\alpha_{11}=V_{CNT}\alpha_{11}^{CNT}+V_m\alpha^m \tag{6.10}$$

$$\alpha_{22}=(1+\nu_{12}^{CNT})V_{CNT}\alpha_{22}^{CNT}+(1+\nu^m)V_m\alpha^m-\nu_{12}\alpha_{11} \tag{6.11}$$

in which α_{11}^{CNT}, α_{22}^{CNT}, and α^m denote the thermal expansion coefficients of the CNTs and matrix, respectively.

6.2.3 DISPLACEMENT FIELD AND STRAINS

The displacement field within the sandwich plate panel is defined according to the HSDT as

$$u(x,y,z)=u_0(x,y)+z\beta_x(x,y)+z^2u_0^*(x,y)+z^3\beta_x^*(x,y) \tag{6.12}$$

$$v(x,y,z)=v_0(x,y)+z\beta_y(x,y)+z^2v_0^*(x,y)+z^3\beta_y^*(x,y) \tag{6.13}$$

$$w(x,y,z)=w_0(x,y) \tag{6.14}$$

where u, v, and w represent the displacement variables along x, y, and z directions, while u_0, v_0, and w_0 signify the corresponding mid-surface displacement variables; β_x and β_y symbolize the rotations of the normal to the mid-surface about y- and x-axes,

respectively; u_0^*, v_0^*, β_x^*, and β_y^* signify the respective higher-order displacement variables. The modified expressions of the displacement variables can be obtained from **Eqs. (6.12)-(6.14)** by enforcing zero transverse shear stresses ($\tau_{xz} = \tau_{yz} = 0$) on both top and bottom surfaces of the sandwich panel as

$$u = u_0 + z\beta_x + z^3\beta_x^* \tag{6.15}$$

$$v = v_0 + z\beta_y + z^3\beta_y^* \tag{6.16}$$

$$w = w_0 \tag{6.17}$$

where $\beta_x^* = -\frac{4}{3h^2}\left(\beta_x + \frac{\partial w_0}{\partial x}\right)$ and $\beta_y^* = -\frac{4}{3h^2}\left(\beta_y + \frac{\partial w_0}{\partial y}\right)$

Finally, the displacement variables can be rewritten as

$$\{\bar{u}\} = [\bar{Z}]\{\Delta\} \tag{6.18}$$

where $\{\bar{u}\}$, $\{\Delta\}$, and $[\bar{Z}]$ denote the displacement component vector, generalized displacement parameter vector, and transformation matrix, respectively, and are expressed as

$$\{\bar{u}\} = [u \quad v \quad w]^T \tag{6.19}$$

$$\{\Delta\} = [u_0 \quad v_0 \quad w_0 \quad \beta_x \quad \beta_y \quad \beta_x^* \quad \beta_y^*]^T \tag{6.20}$$

$$[\bar{Z}] = \begin{bmatrix} 1 & 0 & 0 & z & 0 & z^2 & 0 \\ 0 & 1 & 0 & 0 & z & 0 & z^2 \\ 0 & 0 & 1 & 0 & 0 & 0 & 0 \end{bmatrix} \tag{6.21}$$

Using **Eq.(6.18),** the velocity component vector $\{V\}$ can be obtained as

$$\{V\} = \frac{d\{\bar{u}\}}{dt} = [\bar{Z}]\{\dot{\Delta}\} \tag{6.22}$$

The expressions of the linear strain components are given as

$$\begin{Bmatrix} \varepsilon_{xx} \\ \varepsilon_{yy} \\ \gamma_{xy} \\ \gamma_{xz} \\ \gamma_{yz} \end{Bmatrix} = \begin{Bmatrix} u_{,x} \\ v_{,y} + w/r_y \\ u_{,y} + v_{,x} + w/r_{xy} \\ u_{,z} + w_{,x} \\ v_{,z} + w_{,y} - v/r_y \end{Bmatrix} = \begin{Bmatrix} \varepsilon_{xx}^0 \\ \varepsilon_{yy}^0 \\ \gamma_{xy}^0 \\ \varphi_{xz} \\ \varphi_{yz} \end{Bmatrix} + z\begin{Bmatrix} \kappa_{xx} \\ \kappa_{yy} \\ \kappa_{xy} \\ \kappa_{xz} \\ \kappa_{yz} \end{Bmatrix} + z^2\begin{Bmatrix} 0 \\ 0 \\ 0 \\ \varphi_{xz}^* \\ \varphi_{yz}^* \end{Bmatrix} + z^3\begin{Bmatrix} \kappa_{xx}^* \\ \kappa_{yy}^* \\ \kappa_{xy}^* \\ \kappa_{xz}^* \\ \kappa_{yz}^* \end{Bmatrix} \tag{6.23}$$

where

$$\begin{aligned} &\left[\varepsilon_{xx}^0 \quad \varepsilon_{yy}^0 \quad \gamma_{xy}^0 \quad \varphi_{xz} \quad \varphi_{yz}\right]^T \\ &= [u_{0,x} \quad v_{0,y} + w_0/r_y \quad u_{0,y} + v_{0,x} + 2w_0/r_{xy} \quad \beta_x + w_{0,x} \quad \beta_y + w_{0,y} - v_0/r_y]^T \end{aligned} \tag{6.24}$$

$$[\kappa_{xx} \quad \kappa_{yy} \quad \kappa_{xy} \quad \kappa_{xz} \quad \kappa_{yz}] = [\beta_{x,x} \quad \beta_{y,y} \quad \beta_{x,y} + \beta_{y,x} \quad 0 \quad \beta_y/r_y] \tag{6.25}$$

$$[0 \quad 0 \quad 0 \quad \varphi_{xz}^* \quad \varphi_{yz}^*] = [0 \quad 0 \quad 0 \quad 3\beta_x^* \quad 3\beta_y^*] \tag{6.26}$$

$$[\kappa_{xx}^* \quad \kappa_{yy}^* \quad \kappa_{xy}^* \quad \kappa_{xz}^* \quad \kappa_{yz}^*] = [\beta_{x,x}^* \quad \beta_{y,y}^* \quad \beta_{x,y}^* + \beta_{y,x}^* \quad 0 \quad \beta_y^*/r_y] \tag{6.27}$$

The linear strain component vector $\{\varepsilon_l\}$, as given in **Eq. (6.23)**, can be expressed in terms of mid-plane strain vector in the following compact form

$$\{\varepsilon_l\} = [\bar{T}]\{\varepsilon^0\} \tag{6.28}$$

where the mid-plane strain vector $\{\varepsilon^0\}$ and thickness coordinate matrix $[\bar{T}]$ are defined as

$$\begin{aligned} &\{\varepsilon^0\} \\ &= \left[\varepsilon_{xx}^0 \ \varepsilon_{yy}^0 \ \gamma_{xy}^0 \ \kappa_{xx} \ \kappa_{yy} \ \kappa_{xy} \ \kappa_{xx}^* \ \kappa_{yy}^* \ \kappa_{xy}^* \ \varphi_{xz} \ \varphi_{yz} \ \kappa_{xz} \ \kappa_{yz} \ \varphi_{xz}^* \ \varphi_{yz}^* \ \kappa_{xz}^* \ \kappa_{yz}^*\right]^T \end{aligned} \tag{6.29}$$

$$[\bar{T}] = \begin{bmatrix} 1 & 0 & 0 & z & 0 & 0 & z^3 & 0 & 0 & 0 & 0 & 0 & 0 & 0 & 0 & 0 & 0 \\ 0 & 1 & 0 & 0 & z & 0 & 0 & z^3 & 0 & 0 & 0 & 0 & 0 & 0 & 0 & 0 & 0 \\ 0 & 0 & 1 & 0 & 0 & z & 0 & 0 & z^3 & 0 & 0 & 0 & 0 & 0 & 0 & 0 & 0 \\ 0 & 0 & 0 & 0 & 0 & 0 & 0 & 0 & 0 & 1 & 0 & z & 0 & z^2 & 0 & z^3 & 0 \\ 0 & 0 & 0 & 0 & 0 & 0 & 0 & 0 & 0 & 0 & 1 & 0 & z & 0 & z^2 & 0 & z^3 \end{bmatrix} \quad (6.30)$$

6.2.4 STRESS-STRAIN RELATIONSHIP

The composite sandwich plate is assumed to consist of a number of thin laminae, each with their different orientation of principal material coordinates with respect to the plate coordinates. For a typical lamina, the principal material axes 1 and 2 are considered to lie along and transverse to the fiber direction, respectively, as shown in **Fig. 6.3.** In reference to the material coordinates, Young's moduli are indicated as E_{11} and E_{22}, the shear moduli are indicated as G_{12}, G_{13}, and G_{23}, Poisson's ratio are indicated as ν_{12} and ν_{21}, and the thermal expansion coefficients are indicated by $\alpha_{11}$and α_{22}.

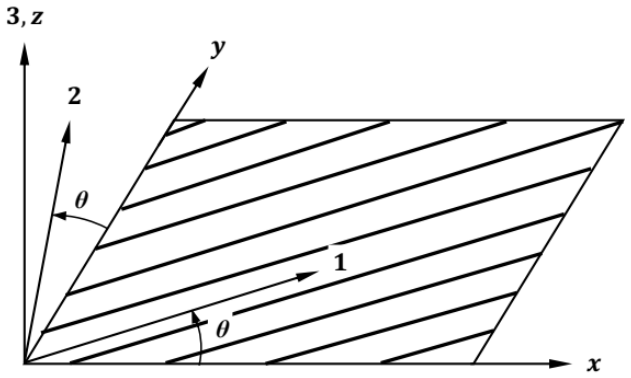

(1,2,3)- Lamina reference axes; (*x, y, z*)- Shell reference axes

Fig. 6.3 A typical lamina with two reference systems

The stress-strain relations for a typical k^{th} lamina of linear thermoelastic materials with reference to material coordinates (1, 2, 3) can be expressed as

$$\begin{Bmatrix} \sigma_{11} \\ \sigma_{22} \\ \tau_{12} \\ \tau_{13} \\ \tau_{23} \end{Bmatrix}_k = \begin{bmatrix} Q_{11} & Q_{12} & 0 & 0 & 0 \\ Q_{12} & Q_{22} & 0 & 0 & 0 \\ 0 & 0 & Q_{66} & 0 & 0 \\ 0 & 0 & 0 & Q_{44} & 0 \\ 0 & 0 & 0 & 0 & Q_{55} \end{bmatrix}_k \left(\begin{Bmatrix} \varepsilon_{11} \\ \varepsilon_{22} \\ \gamma_{12} \\ \gamma_{13} \\ \gamma_{23} \end{Bmatrix} - \begin{Bmatrix} \alpha_{11} \\ \alpha_{22} \\ 0 \\ 0 \\ 0 \end{Bmatrix} \Delta T \right)_k \quad (6.31)$$

where Q_{ij}'s are the on-axis reduced elastic constants of the k^{th} layer and can be expressed as

$$Q_{11} = \frac{E_{11}}{1-\nu_{12}\nu_{21}},\ Q_{22} = \frac{E_{22}}{1-\nu_{12}\nu_{21}},\ Q_{12} = \frac{\nu_{21}E_{11}}{1-\nu_{12}\nu_{21}},$$
$$Q_{66} = G_{12}, Q_{44} = G_{23},\ Q_{55} = G_{13} \quad (6.32)$$

and $\Delta T = T - T_0$ is the rise in temperature from reference temperature T_0 to any elevated temperature T.

Employing the usual transformation rule of stresses/strains as given by Jones (1975[33]), the following stress-strain relations for the k^{th} lamina in the plate coordinates $(x - y - z)$ are obtained

$$\begin{Bmatrix}\sigma_{xx}\\ \sigma_{yy}\\ \tau_{xy}\\ \tau_{xz}\\ \tau_{yz}\end{Bmatrix}_k = \begin{bmatrix}\bar{Q}_{11} & \bar{Q}_{12} & \bar{Q}_{16} & 0 & 0\\ \bar{Q}_{12} & \bar{Q}_{22} & \bar{Q}_{26} & 0 & 0\\ \bar{Q}_{16} & \bar{Q}_{26} & \bar{Q}_{26} & 0 & 0\\ 0 & 0 & 0 & \bar{Q}_{44} & \bar{Q}_{45}\\ 0 & 0 & 0 & \bar{Q}_{45} & \bar{Q}_{55}\end{bmatrix}_k \left(\begin{Bmatrix}\varepsilon_{xx}\\ \varepsilon_{yy}\\ \gamma_{xy}\\ \gamma_{xz}\\ \gamma_{yz}\end{Bmatrix} - \begin{Bmatrix}\varepsilon_{xx}^{TH}\\ \varepsilon_{yy}^{TH}\\ \gamma_{xy}^{TH}\\ 0\\ 0\end{Bmatrix} \right)_k \tag{6.33}$$

where $\bar{Q}_{ij}$'s denote the off-axis reduced elastic coefficients and can be defined as

$$\begin{Bmatrix}\bar{Q}_{11}\\ \bar{Q}_{12}\\ \bar{Q}_{22}\\ \bar{Q}_{16}\\ \bar{Q}_{26}\\ \bar{Q}_{66}\\ \bar{Q}_{44}\\ \bar{Q}_{45}\\ \bar{Q}_{55}\end{Bmatrix} \tag{6.34}$$

$$= \begin{bmatrix} m^4 & 2m^2n^2 & n^4 & 4m^2n^2 & 0 & 0\\ m^2n^2 & m^4+n^4 & m^2n^2 & -4m^2n^2 & 0 & 0\\ n^4 & 2m^2n^2 & m^4 & 4m^2n^2 & 0 & 0\\ m^3n & mn^3-m^3n & -mn^3 & -2m^3n+2mn^3 & 0 & 0\\ mn^3 & m^3n-mn^3 & -m^3n & 2m^3n-2mn^3 & 0 & 0\\ m^2n^2 & -2m^2n^2 & m^2n^2 & (m^2-n^2)^2 & 0 & 0\\ 0 & 0 & 0 & 0 & m^2 & n^2\\ 0 & 0 & 0 & 0 & -mn & mn\\ 0 & 0 & 0 & 0 & n^2 & m^2\end{bmatrix} \begin{Bmatrix}Q_{11}\\ Q_{12}\\ Q_{22}\\ Q_{66}\\ Q_{44}\\ Q_{45}\end{Bmatrix}$$

in which $m = \cos\theta$ and $n = \sin\theta$; θ is the lamination angle with the positive x −axis.
In the stress-strain relationship as expressed **Eq. (6.33),** the expressions of the thermal strains $(\varepsilon_{xx}^{TH}, \varepsilon_{yy}^{TH}, \gamma_{xy}^{TH})$ in reference to the plate coordinates can be obtained as

$$\begin{Bmatrix}\varepsilon_{xx}^{TH}\\ \varepsilon_{yy}^{TH}\\ \gamma_{xy}^{TH}\end{Bmatrix} = \begin{bmatrix} m^2 & n^2\\ n^2 & m^2\\ 2mn & -2mn\end{bmatrix} \begin{Bmatrix}\alpha_{11}\\ \alpha_{22}\end{Bmatrix} (T - T_0) \tag{6.35}$$

The resultant forces and moments acting on the composite sandwich plate obtained upon integration of the stresses through its thickness are given as

$$[\{N\} \quad \{M\} \quad \{M^*\}] = \left[\begin{Bmatrix}N_{xx}\\ N_{yy}\\ N_{xy}\end{Bmatrix} \quad \begin{Bmatrix}M_{xx}\\ M_{yy}\\ M_{xy}\end{Bmatrix} \quad \begin{Bmatrix}M_{xx}^*\\ M_{yy}^*\\ M_{xy}^*\end{Bmatrix} \right] = \int_{-h/2}^{h/2} \begin{Bmatrix}\sigma_{xx}\\ \sigma_{yy}\\ \tau_{xy}\end{Bmatrix}_k [1 \quad z \quad z^3] dz \tag{6.36}$$

$$[\{Q\} \quad \{Q^*\}] = \left[\begin{Bmatrix}Q_{xz}\\ Q_{yz}\end{Bmatrix} \quad \begin{Bmatrix}Q_{xz}^*\\ Q_{yz}^*\end{Bmatrix} \right] = \int_{-h/2}^{h/2} \begin{Bmatrix}\tau_{xz}\\ \tau_{yz}\end{Bmatrix}_k [1 \quad z^2]\, dz \tag{6.37}$$

$$[\{R\} \quad \{R^*\}] = \left[\begin{Bmatrix}R_{xz}\\ R_{yz}\end{Bmatrix} \quad \begin{Bmatrix}R_{xz}^*\\ R_{yz}^*\end{Bmatrix} \right] = \int_{-h/2}^{h/2} \begin{Bmatrix}\tau_{xz}\\ \tau_{yz}\end{Bmatrix}_k [z \quad z^3]\, dz \tag{6.38}$$

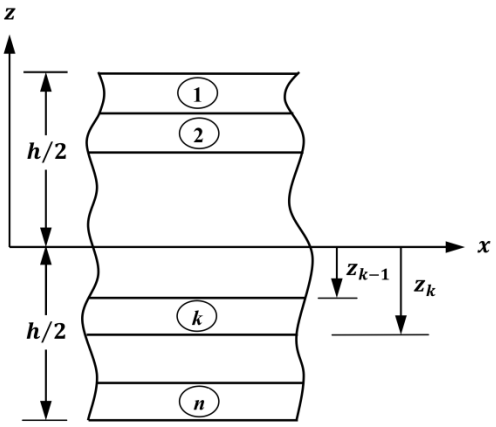

Fig. 6.4. Geometrical details of an n-layered laminate

Substituting the stress-strain relations in **Eq. (6.33)** into **Eqs. (6.36)-(6.38)**, the resultant forces and moments of laminate having n numbers of laminae **(Fig. 6.4)** becomes

$$\begin{Bmatrix} N_{xx} \\ N_{yy} \\ N_{xy} \end{Bmatrix} = \sum_{k=1}^{n} \begin{bmatrix} \bar{Q}_{11} & \bar{Q}_{12} & \bar{Q}_{16} \\ \bar{Q}_{12} & \bar{Q}_{22} & \bar{Q}_{26} \\ \bar{Q}_{16} & \bar{Q}_{26} & \bar{Q}_{66} \end{bmatrix}_k \left\{ \int_{z_{k-1}}^{z_k} \begin{Bmatrix} \varepsilon_{xx}^0 \\ \varepsilon_{yy}^0 \\ \gamma_{xy}^0 \end{Bmatrix} dz + \int_{z_{k-1}}^{z_k} \begin{Bmatrix} \kappa_{xx} \\ \kappa_{yy} \\ \kappa_{xy} \end{Bmatrix} z\, dz + \int_{z_{k-1}}^{z_k} \begin{Bmatrix} \kappa_{xx}^* \\ \kappa_{yy}^* \\ \kappa_{xy}^* \end{Bmatrix} z^3\, dz \right\} \tag{6.39}$$

$$\begin{Bmatrix} M_{xx} \\ M_{yy} \\ M_{xy} \end{Bmatrix} = \sum_{k=1}^{n} \begin{bmatrix} \bar{Q}_{11} & \bar{Q}_{12} & \bar{Q}_{16} \\ \bar{Q}_{12} & \bar{Q}_{22} & \bar{Q}_{26} \\ \bar{Q}_{16} & \bar{Q}_{26} & \bar{Q}_{66} \end{bmatrix}_k \left\{ \int_{z_{k-1}}^{z_k} \begin{Bmatrix} \varepsilon_{xx}^0 \\ \varepsilon_{yy}^0 \\ \gamma_{xy}^0 \end{Bmatrix} z dz + \int_{z_{k-1}}^{z_k} \begin{Bmatrix} \kappa_{xx} \\ \kappa_{yy} \\ \kappa_{xy} \end{Bmatrix} z^2 dz + \int_{z_{k-1}}^{z_k} \begin{Bmatrix} \kappa_{xx}^* \\ \kappa_{yy}^* \\ \kappa_{xy}^* \end{Bmatrix} z^4\, dz \right\} \tag{6.40}$$

$$\begin{Bmatrix} M_{xx}^* \\ M_{yy}^* \\ M_{xy}^* \end{Bmatrix} = \sum_{k=1}^{n} \begin{bmatrix} \bar{Q}_{11} & \bar{Q}_{12} & \bar{Q}_{16} \\ \bar{Q}_{12} & \bar{Q}_{22} & \bar{Q}_{26} \\ \bar{Q}_{16} & \bar{Q}_{26} & \bar{Q}_{66} \end{bmatrix}_k \left\{ \int_{z_{k-1}}^{z_k} \begin{Bmatrix} \varepsilon_{xx}^0 \\ \varepsilon_{yy}^0 \\ \gamma_{xy}^0 \end{Bmatrix} z^3 dz + \int_{z_{k-1}}^{z_k} \begin{Bmatrix} \kappa_{xx} \\ \kappa_{yy} \\ \kappa_{xy} \end{Bmatrix} z^4 dz + \int_{z_{k-1}}^{z_k} \begin{Bmatrix} \kappa_{xx}^* \\ \kappa_{yy}^* \\ \kappa_{xy}^* \end{Bmatrix} z^6\, dz \right\} \tag{6.41}$$

$$\begin{Bmatrix} Q_{xz} \\ Q_{yz} \end{Bmatrix} = \sum_{k=1}^{n} \begin{bmatrix} \bar{Q}_{44} & \bar{Q}_{45} \\ \bar{Q}_{45} & \bar{Q}_{55} \end{bmatrix}_k \left\{ \int_{z_{k-1}}^{z_k} \begin{Bmatrix} \varphi_{xz} \\ \varphi_{yz} \end{Bmatrix} dz + \int_{z_{k-1}}^{z_k} \begin{Bmatrix} \kappa_{xz} \\ \kappa_{yz} \end{Bmatrix} z dz + \int_{z_{k-1}}^{z_k} \begin{Bmatrix} \varphi_{xz}^* \\ \varphi_{yz}^* \end{Bmatrix} z^2 dz + \int_{z_{k-1}}^{z_k} \begin{Bmatrix} \kappa_{xz}^* \\ \kappa_{yz}^* \end{Bmatrix} z^3 dz \right\} \tag{6.42}$$

$$\begin{Bmatrix} Q_{xz}^* \\ Q_{yz}^* \end{Bmatrix} = \sum_{k=1}^{n} \begin{bmatrix} \bar{Q}_{44} & \bar{Q}_{45} \\ \bar{Q}_{45} & \bar{Q}_{55} \end{bmatrix}_k \left\{ \int_{z_{k-1}}^{z_k} \begin{Bmatrix} \varphi_{xz} \\ \varphi_{yz} \end{Bmatrix} z dz + \int_{z_{k-1}}^{z_k} \begin{Bmatrix} \kappa_{xz} \\ \kappa_{yz} \end{Bmatrix} z^2 dz + \int_{z_{k-1}}^{z_k} \begin{Bmatrix} \varphi_{xz}^* \\ \varphi_{yz}^* \end{Bmatrix} z^3 dz + \int_{z_{k-1}}^{z_k} \begin{Bmatrix} \kappa_{xz}^* \\ \kappa_{yz}^* \end{Bmatrix} z^4 dz \right\} \tag{6.43}$$

$$\begin{Bmatrix} R_{xz} \\ R_{yz} \end{Bmatrix} = \sum_{k=1}^{n} \begin{bmatrix} \bar{Q}_{44} & \bar{Q}_{45} \\ \bar{Q}_{45} & \bar{Q}_{55} \end{bmatrix}_k \left\{ \int_{z_{k-1}}^{z_k} \begin{Bmatrix} \varphi_{xz} \\ \varphi_{yz} \end{Bmatrix} z^2 dz + \int_{z_{k-1}}^{z_k} \begin{Bmatrix} \kappa_{xz} \\ \kappa_{yz} \end{Bmatrix} z^3 dz + \int_{z_{k-1}}^{z_k} \begin{Bmatrix} \varphi^*_{xz} \\ \varphi^*_{yz} \end{Bmatrix} z^4 dz + \int_{z_{k-1}}^{z_k} \begin{Bmatrix} \kappa^*_{xz} \\ \kappa^*_{yz} \end{Bmatrix} z^5 dz \right\} \tag{6.44}$$

$$\begin{Bmatrix} R^*_{xz} \\ R^*_{yz} \end{Bmatrix} = \sum_{k=1}^{n} \begin{bmatrix} \bar{Q}_{44} & \bar{Q}_{45} \\ \bar{Q}_{45} & \bar{Q}_{55} \end{bmatrix}_k \left\{ \int_{z_{k-1}}^{z_k} \begin{Bmatrix} \varphi_{xz} \\ \varphi_{yz} \end{Bmatrix} z^3 dz + \int_{z_{k-1}}^{z_k} \begin{Bmatrix} \kappa_{xz} \\ \kappa_{yz} \end{Bmatrix} z^4 dz + \int_{z_{k-1}}^{z_k} \begin{Bmatrix} \varphi^*_{xz} \\ \varphi^*_{yz} \end{Bmatrix} z^5 dz + \int_{z_{k-1}}^{z_k} \begin{Bmatrix} \kappa^*_{xz} \\ \kappa^*_{yz} \end{Bmatrix} z^6 dz \right\} \tag{6.45}$$

where z_k and z_{k-1} are the distances of the bottom of the kth and $(k-1)$th layer from the mid-surface.

The thermal in-plane stress resultant forces and moments

$$\begin{Bmatrix} N^{TH}_{xx} \\ N^{TH}_{yy} \\ N^{TH}_{xy} \end{Bmatrix} = \sum_{k=1}^{n} \begin{bmatrix} \bar{Q}_{11} & \bar{Q}_{12} & \bar{Q}_{16} \\ \bar{Q}_{12} & \bar{Q}_{22} & \bar{Q}_{26} \\ \bar{Q}_{16} & \bar{Q}_{26} & \bar{Q}_{66} \end{bmatrix}_k \int_{z_{k-1}}^{z_k} \begin{Bmatrix} \varepsilon^{TH}_{xx} \\ \varepsilon^{TH}_{yy} \\ \gamma^{TH}_{xy} \end{Bmatrix} dz \tag{6.46}$$

$$\begin{Bmatrix} M^{TH}_{xx} \\ M^{TH}_{yy} \\ M^{TH}_{xy} \end{Bmatrix} = \sum_{k=1}^{n} \begin{bmatrix} \bar{Q}_{11} & \bar{Q}_{12} & \bar{Q}_{16} \\ \bar{Q}_{12} & \bar{Q}_{22} & \bar{Q}_{26} \\ \bar{Q}_{16} & \bar{Q}_{26} & \bar{Q}_{66} \end{bmatrix}_k \int_{z_{k-1}}^{z_k} \begin{Bmatrix} \varepsilon^{TH}_{xx} \\ \varepsilon^{TH}_{yy} \\ \gamma^{TH}_{xy} \end{Bmatrix} z dz \tag{6.47}$$

$$\begin{Bmatrix} M^{*TH}_{xx} \\ M^{*TH}_{yy} \\ M^{*TH}_{xy} \end{Bmatrix} = \sum_{k=1}^{n} \begin{bmatrix} \bar{Q}_{11} & \bar{Q}_{12} & \bar{Q}_{16} \\ \bar{Q}_{12} & \bar{Q}_{22} & \bar{Q}_{26} \\ \bar{Q}_{16} & \bar{Q}_{26} & \bar{Q}_{66} \end{bmatrix}_k \int_{z_{k-1}}^{z_k} \begin{Bmatrix} \varepsilon^{TH}_{xx} \\ \varepsilon^{TH}_{yy} \\ \gamma^{TH}_{xy} \end{Bmatrix} z^3 dz \tag{6.48}$$

Combining **Eqs. (6.39)-(6.48),** the relations of the stress resultants, mid-plane strain, and curvature components can be expressed as

$$\{F\} = [D]\{\varepsilon^0\} - \{F^{TH}\} \tag{6.49}$$

where $\{F\}$, $\{F^{TH}\}$, $\{\varepsilon^0\}$, and $[D]$ are the stress resultant vector, thermal stress resultant vector, mid-plane strain vector, and elasticity matrix, respectively, and are given by

$$\{F_e\} = \left(N_{xx}, N_{yy}, N_{xy}, M_{xx}, M_{yy}, M_{xy}, M^*_{xx}, M^*_{yy}, M^*_{xy}, Q_{xz}, Q_{yz}, Q^*_{xz}, Q^*_{yz}, R_{xz}, R_{yz}, R^*_{xz}, R^*_{yz}\right)^T \tag{6.50}$$

$$\{F^{TH}\} = \left(N^{TH}_{xx}, N^{TH}_{yy}, N^{TH}_{xy}, M^{TH}_{xx}, M^{TH}_{yy}, M^{TH}_{xy}, M^{*TH}_{xx}, M^{*TH}_{yy}, M^{*TH}_{xy}, 0, 0, 0, 0, 0, 0, 0, 0\right)^T \tag{6.51}$$

$$\{\varepsilon^0\} = \left[\varepsilon^0_{xx}\ \ \varepsilon^0_{yy}\ \ \gamma^0_{xy}\ \ \kappa_{xx}\ \ \kappa_{yy}\ \ \kappa_{xy}\ \ \kappa^*_{xx}\ \ \kappa^*_{yy}\ \ \kappa^*_{xy}\ \ \varphi_{xz}\ \ \varphi_{yz}\ \ \kappa_{xz}\ \ \kappa_{yz}\ \ \varphi^*_{xz}\ \ \varphi^*_{yz}\ \ \kappa^*_{xz}\ \ \kappa^*_{yz}\right]^T \tag{6.52}$$

$$[D] = \begin{bmatrix} [A_{ij}] & [B_{ij}] & [C_{ij}] & 0 & 0 & 0 & 0 \\ [B_{ij}] & [D_{ij}] & [E_{ij}] & 0 & 0 & 0 & 0 \\ [C_{ij}] & [E_{ij}] & [F_{ij}] & 0 & 0 & 0 & 0 \\ 0 & 0 & 0 & [A^*_{ij}] & [B^*_{ij}] & [D^*_{ij}] & [C^*_{ij}] \\ 0 & 0 & 0 & [B^*_{ij}] & [D^*_{ij}] & [C^*_{ij}] & [E^*_{ij}] \\ 0 & 0 & 0 & [D^*_{ij}] & [C^*_{ij}] & [E^*_{ij}] & [G^*_{ij}] \\ 0 & 0 & 0 & [C^*_{ij}] & [E^*_{ij}] & [G^*_{ij}] & [F^*_{ij}] \end{bmatrix}_{17\times 17} \tag{6.53}$$

where the stress resultants are defined as

$$\left(A_{ij}, B_{ij}, D_{ij}, C_{ij}, E_{ij}, F_{ij}\right) = \sum_{k=1}^{n} \int_{z_{k-1}}^{z_k} \bar{Q}_{ij}\,(1, z, z^2, z^3, z^4, z^6)dz \quad i,j = 1,2,6 \tag{6.54}$$

$$\left(A^*_{ij}, B^*_{ij}, D^*_{ij}, C^*_{ij}, E^*_{ij}, G^*_{ij}, F^*_{ij}\right) = \sum_{k=1}^{n} \int_{z_{k-1}}^{z_k} \bar{Q}_{ij}(1, z, z^2, z^3, z^4, z^5, z^6)\, dz \quad i,j = 4,5 \tag{6.55}$$

6.3 FINITE ELEMENT FORMULATION

The rectangular planform of the sandwich plate surface is discretized into eight-node iso-parametric plate elements as shown in **Fig. 6.5.** Each node of the element has seven degrees of freedom ($u_0,\ v_0,\ w_0,\ \beta_x,\ \beta_y,\ \beta^*_x,$ and β^*_y). In order to formulate the finite element analysis, an 8-node square master element, as shown in **Fig. 6.6(a)**, is mapped into a real quadrilateral element with curved side as shown in **Fig. 6.6(b).** The displacement field in the master element and geometrical relationship between the master element and real element are governed by the same interpolation function called shape function.

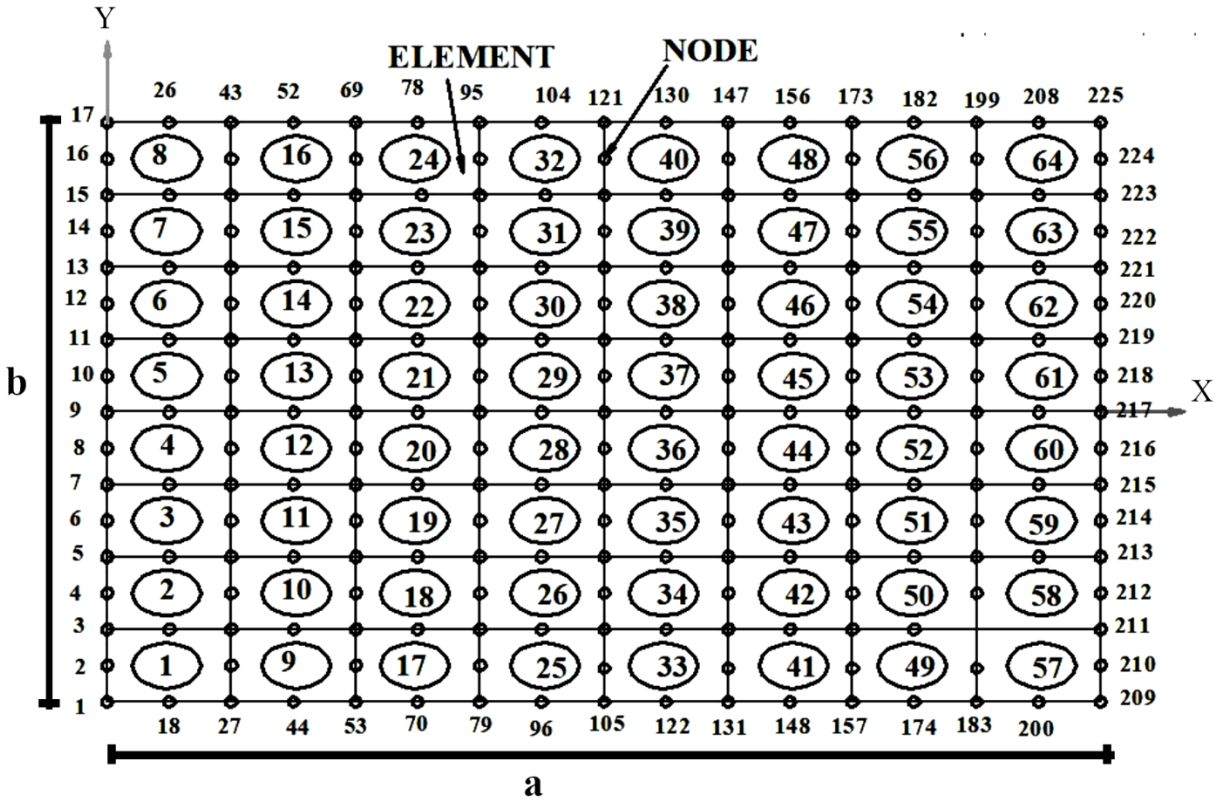

Fig. 6.5 Discretized rectangular planform of the sandwich plate

For satisfactory representation of the displacement field over the element, the shape functions are derived from an interpolation polynomial in terms of the natural or intrinsic co-ordinates ξ and η. The quadratic interpolation function or shape function that defines the variation of the displacement component u is assumed as

$$u(\xi,\eta) = c_1 + c_2\xi + c_3\eta + c_4\xi\eta + c_5\xi^2 + c_6\eta^2 + c_7\xi^2\eta + c_8\xi\eta^2 \tag{6.56}$$

where $c_i (i = 1,2,3, \ldots ,8)$ are the generalized degrees of freedom.

The shape functions N_i at i^{th} node are derived from the interpolation function as (Cook *et al*., 1989)

$$N_i = (1 + \xi\xi_i)(1 + \eta\eta_i)(\xi\xi_i + \eta\eta_i - 1)\ /4 \quad \text{(for } i = 1, 2, 3, 4\text{)} \tag{6.57}$$

$$N_i = (1 - \xi^2)(1 + \eta\eta_i)/2 \quad \text{(for } i = 5, 7\text{)} \tag{6.58}$$

$$N_i = (1 - \eta^2)(1 + \xi\xi_i)\ /2 \quad \text{(for } i = 6, 8\text{)} \tag{6.59}$$

where ξ_i and $\eta_i$are the natural coordinates at i^{th} node.
The accurateness of the shape functions is examined from the following relations

$$\sum_{i=1}^{8} N_i = 1, \quad \sum_{i=1}^{8} \frac{\partial N_i}{\partial \xi} = 1, \quad \sum_{i=1}^{8} \frac{\partial N_i}{\partial \eta} = 1, \tag{6.60}$$

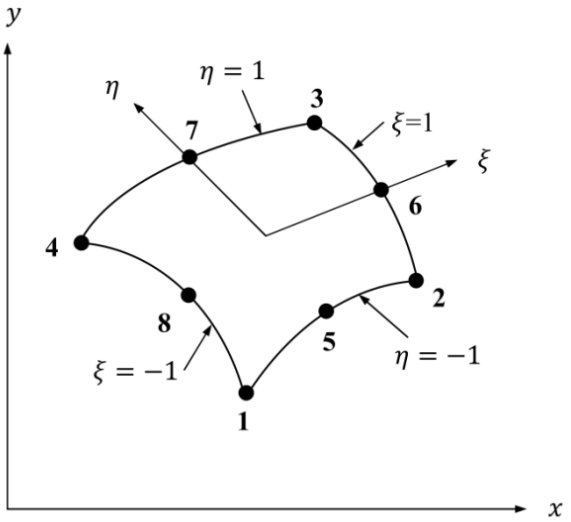

a.

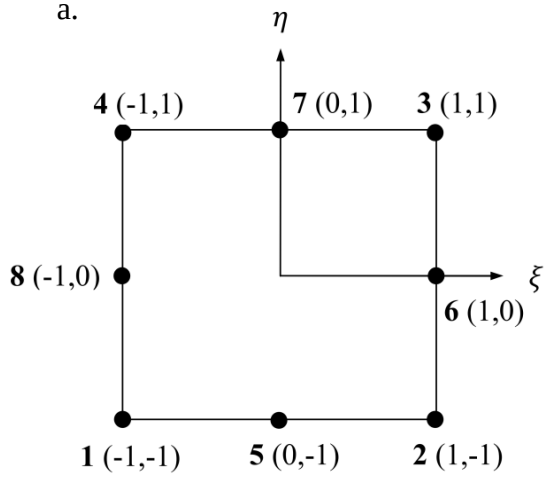

b.

Fig. 6.6 (a) Eight-node element in $x - y$ plane (b) The same element mapped into $\xi - \eta$ plane

The coordinates x and y of a point within the element can be expressed in terms of shape functions N_i and the nodal coordinates (x_i, y_i) as

$$x = \sum_{i=1}^{8} N_i\, x_i \qquad y = \sum_{i=1}^{8} N_i\, y_i \tag{6.61}$$

Using the iso-parametric relation, the mid-plane displacement variables within the element can be expressed in terms of the corresponding nodal displacement parameters as

$$u_0 = \sum_{i=1}^{8} N_i\, u_{0i}\ ; \quad v_0 = \sum_{i=1}^{8} N_i\, v_{0i}\ ; \quad w_0 = \sum_{i=1}^{8} N_i\, w_{0i}\ ; \quad \beta_x = \sum_{i=1}^{8} N_i\, \beta_{xi}\ ;$$
$$\beta_y = \sum_{i=1}^{8} N_i\, \beta_{yi}\ ; \quad \beta_x^* = \sum_{i=1}^{8} N_i\, \beta_{xi}^*\ ; \quad \beta_y^* = \sum_{i=1}^{8} N_i\, \beta_{yi}^* \tag{6.62}$$

and

$$\begin{Bmatrix} N_{i,x} \\ N_{i,y} \end{Bmatrix} = [J]^{-1} \begin{Bmatrix} N_{i,\xi} \\ N_{i,\eta} \end{Bmatrix} \tag{6.63}$$

where $[J]$ symbolizes Jacobian matrix and is given by

$$[J] = \begin{bmatrix} x_{,\xi} & y_{,\xi} \\ x_{,\eta} & y_{,\eta} \end{bmatrix} \tag{6.64}$$

The expressions of the displacement parameters in **Eq. (6.62)** can be expressed in the following compact form

$$\{\Delta\} = [N]\{\delta_e\} \tag{6.65}$$

where $\{\Delta\} = [u_0 \quad v_0 \quad w_0 \quad \beta_x \quad \beta_y \quad \beta_x^* \quad \beta_y^*]^T$ is the vector representing generalized displacement parameter and $\{\delta_e\} = [u_{0i} \quad v_{0i} \quad w_{0i} \quad \beta_{xi} \quad \beta_{yi} \quad \beta_{xi}^* \quad \beta_{yi}^*]^T$ represents nodal displacement parameter vector. The shape function matrix $[N]$ can be expressed as

$$[N] = \begin{bmatrix} N_i & 0 & 0 & 0 & 0 & 0 & 0 \\ 0 & N_i & 0 & 0 & 0 & 0 & 0 \\ 0 & 0 & N_i & 0 & 0 & 0 & 0 \\ 0 & 0 & 0 & N_i & 0 & 0 & 0 \\ 0 & 0 & 0 & 0 & N_i & 0 & 0 \\ 0 & 0 & 0 & 0 & 0 & N_i & 0 \\ 0 & 0 & 0 & 0 & 0 & 0 & N_i \end{bmatrix}_{i=1,2,3,\ldots,8} \tag{6.66}$$

Subsequently, the mid-plane strain vector $\{\varepsilon^0\}$ can be expressed in terms of nodal displacement parameter vector as

$$\{\varepsilon^0\} = [B]\{\delta_e\} \tag{6.67}$$

where $[B]$ is the strain-displacement matrix given as

$$[B] = \sum_{i=1}^{8} \begin{bmatrix} N_{i,x} & 0 & 0 & 0 & 0 & 0 & 0 \\ 0 & N_{i,y} & 0 & 0 & 0 & 0 & 0 \\ N_{i,y} & N_{i,x} & 2N_i/r_{xy} & 0 & 0 & 0 & 0 \\ 0 & 0 & 0 & N_{i,x} & 0 & 0 & 0 \\ 0 & 0 & 0 & 0 & N_{i,y} & 0 & 0 \\ 0 & 0 & 0 & N_{i,y} & N_{i,x} & 0 & 0 \\ 0 & 0 & 0 & 0 & 0 & N_{i,x} & 0 \\ 0 & 0 & 0 & 0 & 0 & 0 & N_{i,y} \\ 0 & 0 & 0 & 0 & 0 & N_{i,y} & N_{i,x} \\ 0 & 0 & N_{i,x} & N_i & 0 & 0 & 0 \\ 0 & 0 & N_{i,y} & 0 & N_i & 0 & 0 \\ 0 & 0 & 0 & 0 & 0 & 0 & 0 \\ 0 & 0 & 0 & 0 & 0 & 0 & 0 \\ 0 & 0 & 0 & 0 & 0 & 3N_i & 0 \\ 0 & 0 & 0 & 0 & 0 & 0 & 3N_i \\ 0 & 0 & 0 & 0 & 0 & 0 & 0 \\ 0 & 0 & 0 & 0 & 0 & 0 & 0 \end{bmatrix}_{i=1,8} \tag{6.68}$$

6.4 GENERAL DYNAMIC EQUILIBRIUM EQUATION

Hamilton's principle applied to the dynamic analysis of elastic bodies states that "among all admissible displacements which satisfy the specific boundary conditions, the actual solution makes the functional $\int (T_k + U)\, dt$ stationary, where T_k and U are the kinetic energy and work done by conservative and non-conservative forces, respectively. The stationary value is actually a minimum".

6.4.1 KINETIC ENERGY OF ROTATING SANDWICH PLATE

Consider two reference systems $\mathcal{R}_0(X, Y, Z)$ and $\mathcal{R}_1(x, y, z)$ to formulate the general dynamic equilibrium of a rotating sandwich plate as shown in the **Fig. 6.7**. The first one refers to the inertial Cartesian coordinate system with the unit vectors $(\mathbf{i_X}, \mathbf{i_Y}, \mathbf{i_Z})$ which is generally fixed to any arbitrary point with the axis of blade hub. The second one with the unit vectors $(\mathbf{i_x}, \mathbf{i_y}, \mathbf{i_z})$ is the plate coordinate system which is also known as local coordinate system. The vector $\mathbf{r_0} = \{X_0, \quad Y_0, \quad Z_0\}$ indicates the translational offsets of plate coordinate system from the inertial reference system.

The kinetic energy of the rotating sandwich plate can be described

$$T_K = \frac{1}{2} \int_{vol} \rho \mathbf{V}.\mathbf{V}\, d(vol) \tag{6.69}$$

where ρ symbolizes the mass density of the plate and $\mathbf{V}$ indicates the absolute velocity of an arbitrary point on the plate in $\mathcal{R}_0(X, Y, Z)$ reference system. The plate is assumed to rotate about the $\mathcal{R}_0(X, Y, Z)$ reference system with an angular velocity $\mathbf{\Omega} = \Omega \mathbf{i_Z}$

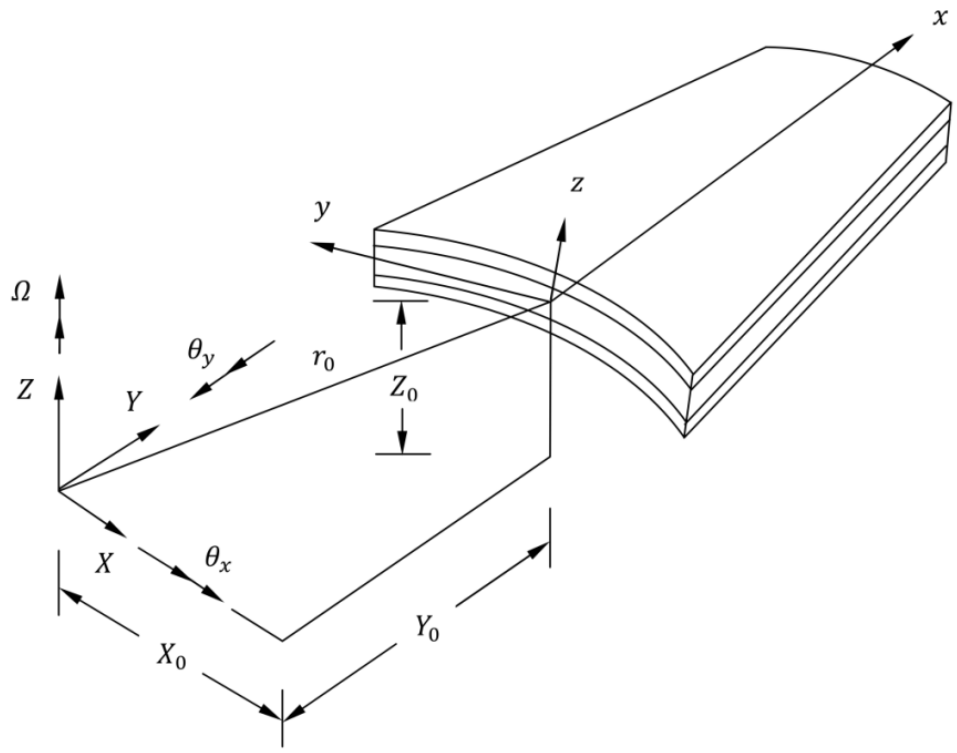

Fig. 6.7. Rotating sandwich plate with two reference systems and their offsets

The components of angular velocity in the $\mathcal{R}_1(x, y, z)$ system can be given by

$$\{\Omega_x,\ \Omega_x,\ \Omega_x\} = \{0,\quad 0,\quad \Omega\}\left[T_{\theta y}\right]^T [T_{\theta x}]^T \tag{6.70}$$

where

$$[T_{\theta x}]^T = \begin{bmatrix} 1 & 0 & 0 \\ 0 & \cos(\theta_x) & -\sin(\theta_x) \\ 0 & \sin(\theta_x) & \cos(\theta_x) \end{bmatrix} \tag{6.71}$$

$$\left[T_{\theta y}\right]^T = \begin{bmatrix} \cos(\theta_y) & 0 & -\sin(\theta_y) \\ 0 & 1 & 0 \\ \sin(\theta_y) & 0 & \cos(\theta_y) \end{bmatrix} \tag{6.72}$$

where Ω symbolizes the rotational speed of the plate about Z axis of the $\mathcal{R}_0(X, Y, Z)$ system, θ_x indicates skew angle and θ_y signifies the pre-cone angle. The order of rotations is θ_x and θ_y.

The fixed translational offsets expressed with reference to plate coordinate system are given as

$$\left\{l_x,\ l_y,\ l_z\right\} = \{X_0,\quad Y_0,\quad Z_0\}\left[T_{\theta y}\right]^T [T_{\theta x}]^T \tag{6.73}$$

According to Chasle's theorem,

$$\mathbf{V} = \frac{d\mathbf{r}}{dt} + \mathbf{\Omega} \times \mathbf{r} \tag{6.74}$$

where $\boldsymbol{r}$ indicates the position vector of the arbitrary point on the plate after deformation from the origin of the inertial reference frame and is given by

$$\mathbf{r} = (l_x + x + u)\mathbf{i_x} + \big(l_y + y + v\big)\mathbf{i_y} + (l_z + z + w)\mathbf{i_z} \tag{6.75}$$

where (x, y, z) are the coordinates of the point in the plate coordinate system (local coordinate axes), $\big(l_x, l_y, l_z\big)$ are the fixed translational offsets of the plate coordinate axes from the inertial axes expressed with reference to the plate coordinate system, and (u, v, w) are the elastic deflections.

The angular velocity vector **Ω** in **Eq. (6.74)** is given by

$$\mathbf{\Omega} = \Omega\mathbf{k_Z} = \Omega_x\mathbf{i_x} + \Omega_y\mathbf{i_y} + \Omega_z\mathbf{i_z} \tag{6.76}$$

where $\big(\Omega_x, \Omega_y, \Omega_z\big)$ are the components of angular velocity in the plate coordinate system.

Substituting the expressions of **r** and **Ω** into **Eq. (6.74)**, the absolute velocity **V** can be derived as

$$\begin{aligned} \boldsymbol{V} = &\big[\dot{u}+\Omega_y(l_z + z + w) - \Omega_z\big(l_y + y + v\big)\big]\mathbf{i_x} \\ &+ [\dot{v}+\Omega_z(l_x + x + u) - \Omega_x(l_z + z + w)]\mathbf{i_y} \\ &+ \big[\dot{w}+\Omega_x\big(l_y + y + v\big) - \Omega_y(l_x + x + u)\big]\mathbf{i_z} \end{aligned} \tag{6.77}$$

Computing $|\mathbf{V}|^2$and canceling the terms which give no contribution when Lagrange's equation
of motion is applied and substituting the result in kinetic energy expression, we have,

$$\begin{aligned} T_K = &\frac{1}{2}\int_{vol} \rho \begin{Bmatrix}\dot{u}\\ \dot{v}\\ \dot{w}\end{Bmatrix}^T \begin{Bmatrix}\dot{u}\\ \dot{v}\\ \dot{w}\end{Bmatrix} d(vol) + \frac{1}{2}\int_{vol} \rho \begin{Bmatrix}\dot{u}\\ \dot{v}\\ \dot{w}\end{Bmatrix}^T [A_1] \begin{Bmatrix}u\\ v\\ w\end{Bmatrix} d(vol) \\ &+ \frac{1}{2}\int_{vol} \rho \begin{Bmatrix}u\\ v\\ w\end{Bmatrix}^T [A_2] \begin{Bmatrix}u\\ v\\ w\end{Bmatrix} d(vol) \\ &+ \frac{1}{2}\int_{vol} \rho \begin{Bmatrix}l_x + x\\ l_y + y\\ l_z + z\end{Bmatrix}^T [A_2] \begin{Bmatrix}u\\ v\\ w\end{Bmatrix} d(vol) \end{aligned} \tag{6.78}$$

where the matrices $[A_1]$ and $[A_2]$ are given by

$$[A_1] = \begin{bmatrix} 0 & -2\Omega_z & 2\Omega_y \\ 2\Omega_z & 0 & -2\Omega_x \\ -2\Omega_y & 2\Omega_x & 0 \end{bmatrix} \tag{6.79}$$

$$[A_2] = \begin{bmatrix} \Omega_y^2 + \Omega_z^2 & -\Omega_x\Omega_y & -\Omega_x\Omega_z \\ -\Omega_x\Omega_y & \Omega_x^2 + \Omega_z^2 & -\Omega_y\Omega_z \\ -\Omega_x\Omega_z & -\Omega_y\Omega_z & \Omega_x^2 + \Omega_y^2 \end{bmatrix} \tag{6.80}$$

Substituting $[u, \quad v, \quad w]^T = [\bar{Z}]\{\Delta\}$ as expressed in **Eq. (6.18)** into **Eq.(6.78),** the elemental kinetic energy becomes

$$\begin{aligned} T_{Ke} = &\frac{1}{2}\int_{vol} \{\dot{\Delta}\}^T[\bar{Z}]^T\rho\,[\bar{Z}]\{\dot{\Delta}\}\,d(vol) + \frac{1}{2}\int_{vol} \{\dot{\Delta}\}^T[\bar{Z}]^T\rho[A_1]\,[\bar{Z}]\{\Delta\}\,d(vol) \\ &+ \frac{1}{2}\int_{vol} [\Delta]^T[\bar{Z}]^T\rho[A_2]\,[\bar{Z}]\{\Delta\}\,d(vol) + \int_{vol} \rho \begin{Bmatrix}l_x + x\\ l_y + y\\ l_z + z\end{Bmatrix}^T [A_2][\bar{Z}]\{\Delta\}d(vol) \end{aligned} \tag{6.81}$$

Where $[m_I]$ refers to the matrix of inertia per unit area and can be expressed as

$$[m_I] = \int_{-h/2}^{h/2} [\bar{Z}]^T \rho\, [\bar{Z}]\, dz \tag{6.82}$$

Further, putting $\Delta = [N]\{\delta_e\}$ into **Eq. (6.81),** the elemental kinetic energy is finally expressed in the following form

$$T_{Ke} = \frac{1}{2}\{\dot{\delta}_e\}^T [M_e]\{\dot{\delta}_e\} + \frac{1}{2}\{\dot{\delta}_e\}^T [C_e]\{\delta_e\} + \frac{1}{2}\{\delta_e\}^T [K_{Re}]\{\delta_e\} + \{\delta_e\}^T \{F_{ce}\} \tag{6.83}$$

where $[M_e]$, $[C_e]$, $[K_{Re}]$, and $\{F_{\Omega e}\}$ denote the mass matrix, Coriolis matrix (skew-symmetric), rotational stiffness matrix (symmetric and positive definite), and centrifugal force vector for the plate element, respectively, and are defined as

$$[M_e] = \int_{-1}^{1}\int_{-1}^{1} [N]^T [m_I]\, [N] |J| d\xi d\eta \tag{6.84}$$

$$[C_e] = \rho \int_{vol} [N]^T [\bar{Z}]^T [A_1][\bar{Z}][N]\, d(vol) \tag{6.85}$$

$$[K_{Re}] = \rho \int_{vol} [N]^T [\bar{Z}]^T [A_2][\bar{Z}][N]\, d(vol) \tag{6.86}$$

$$\{F_{\Omega e}\} = \rho \int_{vol} [N]^T [\bar{Z}][A_2] \begin{Bmatrix} l_x + x \\ l_y + y \\ l_z + z \end{Bmatrix}^T d(vol) \tag{6.87}$$

On substitution of the expression of the transformation matrix $[\bar{Z}]$ into **Eq. (6.82),** the inertia matrix becomes

$$[m_I] = \begin{bmatrix} I_1 & 0 & 0 & I_2 & 0 & I_4 & 0 \\ 0 & I_1 & 0 & 0 & I_2 & 0 & I_4 \\ 0 & 0 & I_1 & 0 & 0 & 0 & 0 \\ I_2 & 0 & 0 & I_3 & 0 & I_5 & 0 \\ 0 & I_2 & 0 & 0 & I_3 & 0 & I_5 \\ I_4 & 0 & 0 & I_5 & 0 & I_3 & 0 \\ 0 & I_4 & 0 & 0 & I_5 & 0 & I_3 \end{bmatrix} \tag{6.88}$$

where $I_1$is the normal inertia, $I_2$is the rotary inertia and (I_3, I_4, I_5, I_7) are the higher-order inertias and are defined by

$$(I_1, I_2, I_3, I_4, I_5, I_7) = \sum_{k=1}^{n} \int_{z_{k-1}}^{z_k} \rho_k (1, z, z^2, z^3, z^4, z^6)\, dz \tag{6.89}$$

where ρ_k is the mass density of the k^{th} layer.

6.4.2 STRAIN ENERGY OF ROTATING SANDWICH PLATE

The elastic strain energy of the sandwich plate element is expressed as

$$U_e^E = \frac{1}{2} \int_{vol} \{\varepsilon_l\}^T \{\sigma\}\, d(vol) \tag{6.90}$$

Using $\{\varepsilon_l\} = [\bar{T}]\{\varepsilon^0\}$ and $\{F\} = [D]\{\varepsilon^0\}$, the above expression can be rewritten

$$U_e^E = \frac{1}{2} \int_A \{\varepsilon^0\}^T\, [D]\{\varepsilon^0\} dA \tag{6.91}$$

in which $[D] = \int_{-h/2}^{h/2} [\bar{T}]^T \left[\bar{Q}_{ij}\right][\bar{T}] dz$ is the elasticity matrix.

Substituting $\{\varepsilon^0\} = [B]\{\delta_e\}$ in **Eq. (6.90),** the elemental elastic strain energy becomes

$$U_e^E = \frac{1}{2}\int_A \{\delta_e\}^T [B]^T [D][B]\{\delta_e\} dA = \frac{1}{2}\{\delta_e\}^T [K_e]\{\delta_e\} \tag{6.92}$$

where $[K_e]$ is the elastic stiffness matrix for the plate element that can be written as

$$[K_e] = \int_{-1}^{1}\int_{-1}^{1} [B]^T [D][B]|J| d\xi d\eta \tag{6.93}$$

The non-linear strain components according to the Green-Lagrange relations are given as (Cook *et al.*,[32])

$$\{\varepsilon_{nl}\} = \begin{Bmatrix} \varepsilon_{xx} \\ \varepsilon_{yy} \\ \gamma_{xy} \\ \gamma_{xz} \\ \gamma_{yz} \end{Bmatrix}_{nl} = \frac{1}{2}\begin{Bmatrix} (u_{,x})^2 + (v_{,x} + w/r_{xy})^2 + (w_{,x})^2 \\ (u_{,y} + w/r_{xy})^2 + (v_{,y})^2 + (w_{,y})^2 \\ 2[u_{,x}(u_{,y} + w/r_{xy}) + (v_{,x} + w/r_{xy})(v_{,y}) + w_{,x}(w_{,y})] \\ 2[u_{,z}u_{,x} + v_{,z}(v_{,x} + w/r_{xy}) + w_{,z}w_{,x}] \\ 2[u_{,z}(u_{,y} + w/r_{xy}) + v_{,z}(v_{,y}) + w_{,z}(w_{,y})] \end{Bmatrix} \tag{6.94}$$

The expressions of the nonlinear strain components in the **Eq. (6.94)** can be written in compact form as

$$\{\varepsilon_{nl}\} = \frac{1}{2}[\Gamma][G]\{\delta_e\} \tag{6.95}$$

where $[\Gamma]$ is obvious from **Eq. (6.94)** and **Eq. (6.95),** and $[G]$ is the matrix that contains the derivatives of shape functions as given below

$$[G] = \sum_{i=1}^{8} \begin{bmatrix} N_{i,x} & 0 & 0 & 0 & 0 & 0 & 0 \\ N_{i,y} & 0 & N_i/r_{xy} & 0 & 0 & 0 & 0 \\ 0 & N_{i,x} & N_i/r_{xy} & 0 & 0 & 0 & 0 \\ 0 & N_{i,y} & 0 & 0 & 0 & 0 & 0 \\ 0 & 0 & N_{i,x} & 0 & 0 & 0 & 0 \\ 0 & 0 & N_{i,y} & 0 & 0 & 0 & 0 \\ 0 & 0 & 0 & N_{i,x} & 0 & 0 & 0 \\ 0 & 0 & 0 & N_{i,y} & 0 & 0 & 0 \\ 0 & 0 & 0 & 0 & N_{i,x} & 0 & 0 \\ 0 & 0 & 0 & 0 & N_{i,y} & 0 & 0 \\ 0 & 0 & 0 & 0 & 0 & N_{i,x} & 0 \\ 0 & 0 & 0 & 0 & 0 & N_{i,y} & 0 \\ 0 & 0 & 0 & 0 & 0 & 0 & N_{i,x} \\ 0 & 0 & 0 & 0 & 0 & 0 & N_{i,y} \\ 0 & 0 & 0 & 0 & 0 & 0 & 0 \\ 0 & 0 & 0 & 0 & 0 & 0 & 0 \\ 0 & 0 & 0 & 0 & 0 & 0 & 0 \\ 0 & 0 & 0 & 0 & 0 & 0 & 0 \end{bmatrix} \tag{6.96}$$

The elemental strain energy resulting from the initial stresses due to thermal and rotational loads is given as

$$U_e^{IS} = \int_{vol} \{\varepsilon_{nl}\}^T \{\sigma_{0TH}\}\, d(vol) + \int_{vol} \{\varepsilon_{nl}\}^T \{\sigma_{0R}\}\, d(vol) \tag{6.97}$$

where $\{\sigma_{0TH}\}$ and $\{\sigma_{0R}\}$ are the initial stress vectors induced due to the thermal and rotational loads, respectively.

The strain energy due to initial stresses, as given in **Eq. (6.97)**, can be rewritten using **Eq. (6.95)** as

$$U_e^{IS} = \frac{1}{2} \int_{vol} \{\delta_e\}^T [G]^T [\Gamma]^T \{\sigma_{0TH}\}\, d(vol) + \frac{1}{2} \int_{vol} \{\delta_e\}^T [G]^T [\Gamma]^T \{\sigma_{0R}\}\, d(vol) \tag{6.98}$$

Now the following integrations are obtained as

$$\int_{-h/2}^{h/2} [\Gamma]^T \{\sigma_{0TH}\} dz = [S_{TH}][G]\,\{\delta_e\} \tag{6.99}$$

$$\int_{-h/2}^{h/2} [\Gamma]^T \{\sigma_{0R}\} dz = [S_R][G]\,\{\delta_e\} \tag{6.100}$$

where $[S_{TH}]$ and $[S_R]$ are the matrices consisting of in-plane stress resultants induced due to thermal and rotational effects, respectively, as given in **Appendix.**

Finally, the elemental strain energy due to initial stresses can be reduced as

$$U_e^{IS} = \frac{1}{2}\{\delta_e\}^T [K_{\sigma THe}]\{\delta_e\} + \frac{1}{2}\{\delta_e\}^T [K_{\sigma Re}]\{\delta_e\} \tag{6.101}$$

in which $[K_{\sigma THe}]$ and $[K_{\sigma Re}]$ refer to the element geometric stiffness matrices due to thermal and rotational effects, respectively, and are given by

$$[K_{\sigma THe}] = \int_{-1}^{1}\int_{-1}^{1} [G]^T\, [S_{TH}][G]|J| d\xi d\eta \tag{6.102}$$

$$[K_{\sigma Re}] = \int_{-1}^{1}\int_{-1}^{1} [G]^T\, [S_R][G]|J| d\xi d\eta \tag{6.103}$$

The total strain energy for the element of sandwich plate considering thermal and rotational effects is given by

$$U_e = U_e^E + U_e^{IS} = \tfrac{1}{2}\{\delta_e\}^T [K_e]\{\delta_e\} + \tfrac{1}{2}\{\delta_e\}^T [K_{\sigma THe}]\{\delta_e\} + \tfrac{1}{2}\{\delta_e\}^T [K_{\sigma Re}]\{\delta_e\} \tag{6.104}$$

6.4.3 GOVERNING EQUATION OF MOTION

The governing equation for the dynamic equilibrium of the rotating composite sandwich panel is derived using Lagrange's equation of motion as given by

$$\frac{d}{dt}\left[\frac{\partial}{\partial \dot{\delta}}(T_K - U)\right] - \frac{\partial}{\partial \delta}(T_K - U) = \{F^{EX}\} \tag{6.105}$$

where $\{F^{EX}\}$ is the externally applied load vector.

Substituting the expressions of T_{Ke} and U_e into **Eq. (6.105),** the dynamic equilibrium equation of the sandwich plate element is derived as

$$\begin{aligned}[M_e]\{\ddot{\delta}_e\} + [C_e]\{\dot{\delta}_e\} + ([K_e] + [K_{\sigma THe}] + [K_{\sigma Re}] - [K_{Re}])\{\delta_e\} \\ = \{F_{\Omega e}\} + \{P_e^{TH}\} + \{F_e\}\end{aligned} \tag{6.106}$$

In the case of moderate rotating speed for which the matrices $[C_e]$ and $[K_{Re}]$ are ignored, the dynamic equilibrium equation of the sandwich plate element is reduced to

$$[M_e]\{\ddot{\delta}_e\} + ([K_e] + [K_{\sigma THe}] + [K_{\sigma Re}])\{\delta_e\} = \{F_{\Omega e}\} + \{P_e^{TH}\} + \{F_e\} \quad (6.107)$$

where $[M_e]$, $[K_e]$, $[K_{\sigma THe}]$, $[K_{\sigma Re}]$, and $\{P_e^{TH}\}$ represent the elemental mass matrix, elemental elastic stiffness matrix, elemental geometric stiffness matrix due to thermal load, elemental geometric stiffness matrix due to rotational load, and elemental thermal load vector, respectively, and are defined as

$$[M_e] = \int_{-1}^{1}\int_{-1}^{1} [N]^T [m_l] [N] |J| d\xi d\eta \quad (6.108)$$

$$[K_e] = \int_{-1}^{1}\int_{-1}^{1} [B]^T [D][B] |J| d\xi d\eta \quad (6.109)$$

$$[K_{\sigma THe}] = \int_{-1}^{1}\int_{-1}^{1} [G]^T [S_{TH}][G] |J| d\xi d\eta \quad (6.110)$$

$$[K_{\sigma Re}] = \int_{-1}^{1}\int_{-1}^{1} [G]^T [S_R][G] |J| d\xi d\eta \quad (6.111)$$

$$\{P_e^{TH}\} = \int_{-1}^{1}\int_{-1}^{1} [B]^T [F^{TH}] |J| d\xi d\eta \quad (6.112)$$

The integrals in the above expressions are numerically evaluated by using Gaussian quadrature of orders 2 (4 points) (Cook *et al.*, [34]).

The following global form of the dynamic equilibrium equation is obtained by assembling all the elemental matrices and force vectors in reference to the common global coordinates

$$[M]\{\ddot{\delta}\} + ([K] + [K_{\sigma TH}] + [K_{\sigma R}])\{\delta\} = \{F(\Omega^2)\} + \{P^{TH}\} + \{F\} \quad (6.113)$$

where $[M]$, $[K]$, $[K_{\sigma TH}]$, and $[K_{\sigma R}]$ indicate the global mass matrix, global elastic stiffness matrix, global geometric stiffness matrices due to thermal and rotational loads, respectively, $\{\delta\}$ represents the global displacement vector, $F(\Omega^2)$ is the nodal equivalent centrifugal load vector, $\{F\}$ signifies the global externally applied load vector, and $\{P^{TH}\}$ signifies the global thermal load vector.

The matrix $[K_{\sigma R}]$ depends on initial stress distribution due to rotational load and is estimated by iterative procedure (Sreenivasamurthy and Ramamurti,[1]) upon solving:

$$([K] + [K_{\sigma TH}] + [K_{\sigma R}])\{\delta\} = \{F(\Omega^2)\} \quad (6.114)$$

First, stresses due to rotational load are converged to zero, and the above equation becomes

$$([K] + [K_{\sigma TH}])\{\delta\} = \{F(\Omega^2)\} \quad (6.115)$$

Solving **Eq. (6.115)** gives the first set of stress distribution, then **Eq. (6.114)** becomes

$$(([K] + [K_{\sigma TH}]) + [K_{\sigma R}]_1)\{\delta\} = \{F(\Omega^2)\} \quad (6.116)$$

The solution of the above equation gives a new set stress distribution and the stresses are found to converge within two iterations.

6.5 SOLUTION PROCEDURE

6.5.1 BOUNDARY CONDITIONS

In the finite element analysis, boundary conditions are imposed by considering or vanishing the generalized displacements $u, v, w, \beta_x, \beta_y, \beta_x^*$, and β_y^* at the different nodes of the discretized structure.

The essential boundary conditions of the cantilevered sandwich plate are:

$$u = v = w = \beta_x = \beta_y = \beta_x^* = \beta_y^* = 0 \ ; \ x = 0 \tag{6.117}$$

6.5.2 FORMULATING FREE VIBRATION PROBLEM

The natural frequencies and eigenvectors are obtained about the deformed configuration. For static analysis, the time-dependent terms in **Eq. (6.113)** are neglected and the following form is obtained

$$([K] + [K_{\sigma TH}] + [K_{\sigma R}])\{\delta_{static}\} = \{F(\Omega^2)\} \tag{6.118}$$

where δ_{static} is the static equilibrium solution as a result of the combined effects of thermal and centrifugal loads.

In case of the dynamic analyses, both the static as well as the time-dependent components are considered where the displacement vector $\{\delta\}$ is expressed as the sum of a static and a dynamic term. Thus,

$$\{\delta\} = \{\delta_{static}\} + \{\delta_p\} \tag{6.119}$$

where $\{\delta_p\}$ is a small linear time-dependent perturbation about the static deflected position $\{\delta_{static}\}$.

The equation of motion for free vibration is given by

$$[M]\{\ddot{\delta}\} + ([K] + [K_{\sigma TH}] + [K_{\sigma R}])\{\delta\} = 0 \tag{6.120}$$

Assuming harmonic vibrations, $\{\delta\} = \{\delta\} \exp(i\omega_n t)$ we have

$$\left[([K] + [K_{\sigma TH}] + [K_{\sigma R}]) - \omega_n^2[M]\right]\{\delta\} = 0 \tag{6.121}$$

This is a standard eigenvalue problem and is solved for the eigenvalues and eigenvectors by the QR iteration algorithm (Bathe, 1990[35])

$$[\mathcal{A}]\{\delta\} = \lambda\{\delta\} \tag{6.122}$$

where $[\mathcal{A}] = ([K] + [K_\sigma]_{TH} + [K_\sigma]_R)^{-1}[M]$, and $\lambda = 1/\omega_n^2$

Thus natural frequency and second mode of vibration of the sandwich plate was found

6.5.3.APPENDIX

Elements of the matrices $[S]$ matrix

$$
= \begin{bmatrix}
S_{11} & & & & & & & & & & & & & & & & \\
S_{21} & S_{22} & & & & & & & & & & & & & & & \\
0 & 0 & S_{33} & & & & & & & & & & & & & & \\
0 & 0 & S_{43} & S_{44} & & & & & & & & & & & & & \\
0 & 0 & 0 & 0 & S_{55} & & & & & & & & & & & & \\
0 & 0 & 0 & 0 & S_{65} & S_{66} & & & & & & & & & & & \\
S_{71} & S_{72} & 0 & 0 & 0 & 0 & S_{77} & & & & & & & & & & \\
S_{81} & S_{82} & 0 & 0 & 0 & 0 & S_{87} & S_{88} & & & & & & & & & \\
0 & 0 & S_{93} & S_{94} & 0 & 0 & 0 & 0 & S_{99} & & & & & & & & \\
0 & 0 & S_{103} & S_{104} & 0 & 0 & 0 & 0 & S_{109} & S_{1010} & & & & & & & \\
0 & 0 & 0 & 0 & S_{115} & S_{116} & 0 & 0 & 0 & 0 & S_{1111} & & & & & & \\
0 & 0 & 0 & 0 & S_{125} & S_{126} & 0 & 0 & 0 & 0 & S_{1211} & S_{1212} & & & & & \\
S_{131} & S_{132} & 0 & 0 & 0 & 0 & S_{137} & S_{138} & 0 & 0 & 0 & 0 & S_{1313} & & & & \\
S_{141} & S_{142} & 0 & 0 & 0 & 0 & S_{147} & S_{148} & 0 & 0 & 0 & 0 & S_{1413} & S_{1414} & & & \\
0 & 0 & S_{153} & S_{154} & 0 & 0 & 0 & 0 & S_{159} & S_{1510} & 0 & 0 & 0 & 0 & S_{1515} & & \\
0 & 0 & S_{163} & S_{164} & 0 & 0 & 0 & 0 & S_{169} & S_{1610} & 0 & 0 & 0 & 0 & S_{1615} & S_{1616} & \\
0 & 0 & 0 & 0 & S_{175} & S_{176} & 0 & 0 & 0 & 0 & S_{1711} & S_{1712} & 0 & 0 & 0 & 0 & S_{1717} \\
0 & 0 & 0 & 0 & S_{185} & S_{186} & 0 & 0 & 0 & 0 & S_{1811} & S_{1812} & 0 & 0 & 0 & 0 & S_{1817} & S_{1818}
\end{bmatrix}
$$

in which

$$S_{11} = S_{33} = S_{55} = N_x, \quad S_{22} = S_{44} = S_{66} = N_y\,, \quad S_{21} = S_{43} = S_{65} = N_{xy}\,,$$

$$S_{77} = S_{99} = S_{1111} = N_x h^2/12,\ S_{88} = S_{1010} = S_{1212} = N_y h^2/12,$$

$$S_{87} = S_{109} = S_{1211} = N_{xy} h^2/12,$$

$$S_{1313} = S_{1515} = S_{1717} = N_x h^6/448, \quad S_{1414} = S_{1616} = S_{1818} = N_y h^6/448,$$

$$S_{1413} = S_{1615} = S_{1817} = N_{xy} h^6/448\,, \quad S_{71} = S_{93} = S_{115} = M_x,$$

$$S_{82} = S_{104} = S_{126} = M_y, \quad S_{81} = S_{103} = S_{125} = M_{xy}\,,\ S_{137} = S_{159} = S_{1711} = N_x h^4/80,$$

$$S_{148} = S_{1610} = S_{1812} = N_y h^4/80,\ S_{147} = S_{169} = S_{1811} = N_{xy} h^4/80,$$

$$S_{131} = S_{153} = S_{175} = M_x^*,\ S_{142} = S_{164} = S_{186} = M_y^*,\ S_{141} = S_{163} = S_{185} = M_{xy}^*$$

CH7:-SIMULATIONS

7.1. MODEL OF SANDWICH STRUCTURE WITH HONEYCOMB CORE - AUXETIC AND NON RE-ENTRANT HONEYCOMB CORE

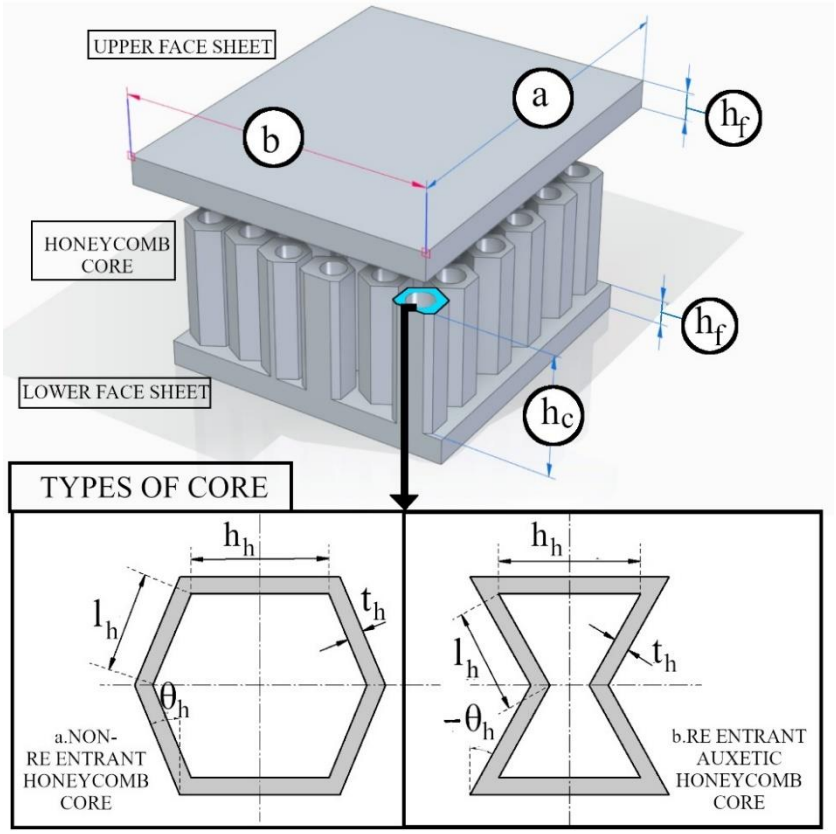

Fig7.1. Sandwich structure with Honeycomb Core

Sandwich structures consists of a core and two face plates or face sheets. In the sandwich models, re-entrant auxetic honeycomb and non re-entrant honeycomb core are chosen. This sandwich structures have high flexural stiffness and low weight. Face plates or face sheets helps to carry tension and compression load and core helps to carry the shear load. The length of the sandwich structure is 'a', width of the sandwich structure is 'b' and height of the sandwich structure is 'h. The face sheet thickness is h_f and the core thickness is h_c.

7.2. SIMULATION OF THE MODEL

Based on the above model, CAD models were first developed and simulated to get the natural frequency in ABAQUS^{TM} FEA environment. The element we used is C3D8R which is which is a brick element with reduced integration.Fig.7.4 shows the meshing details of the model. Lancos Eigen-solver was used to obtain the natural frequency of the assembly of a core and two face sheets. In the figure 7.2.,7.3,7.4,7.5 one out of many simulations is illustrated. In figure 7.2.,7.3,7.4,7.5, simulation processes of re-entrant auxetic honeycomb model are illustrated in chronological manner.

In fig.7.2. auxetic honeycomb core was imported to ABAQUS™ FEA environment. Then the core was given the material property of PLA.

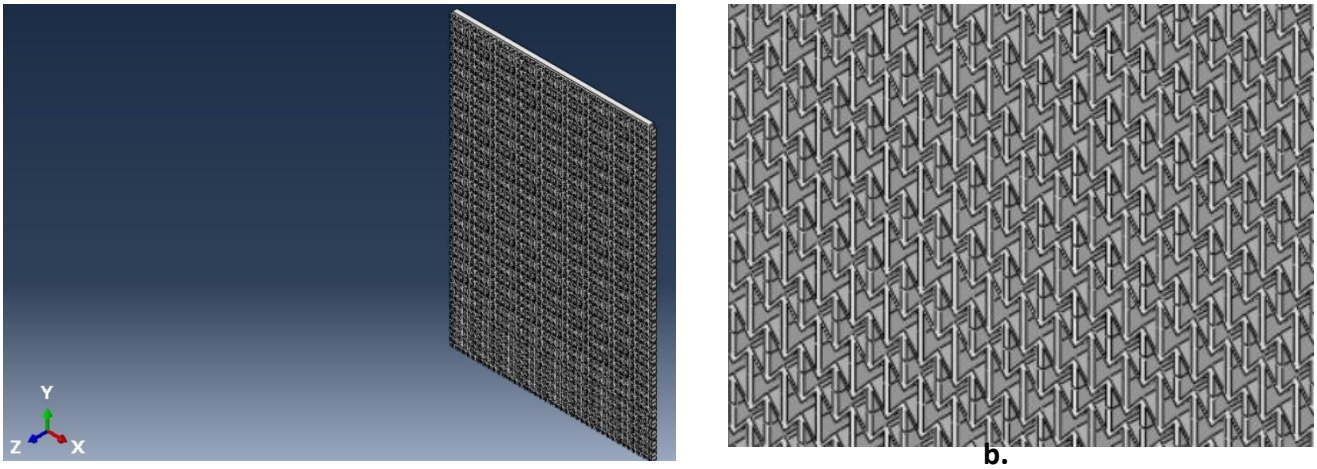

a. **b.**

Fig 7. 2.Auxetic core CAD model

a. Auxetic core CAD model used for FEA analysis in ABAQUS™

b. Zoomed view of the Auxetic Core

Then two face sheets were attached to the core. The material property of the face sheets was of aluminium. Assembly has a boundary condition of cantilever support and aluminium face sheets and the PLA core had tie constraints between them.

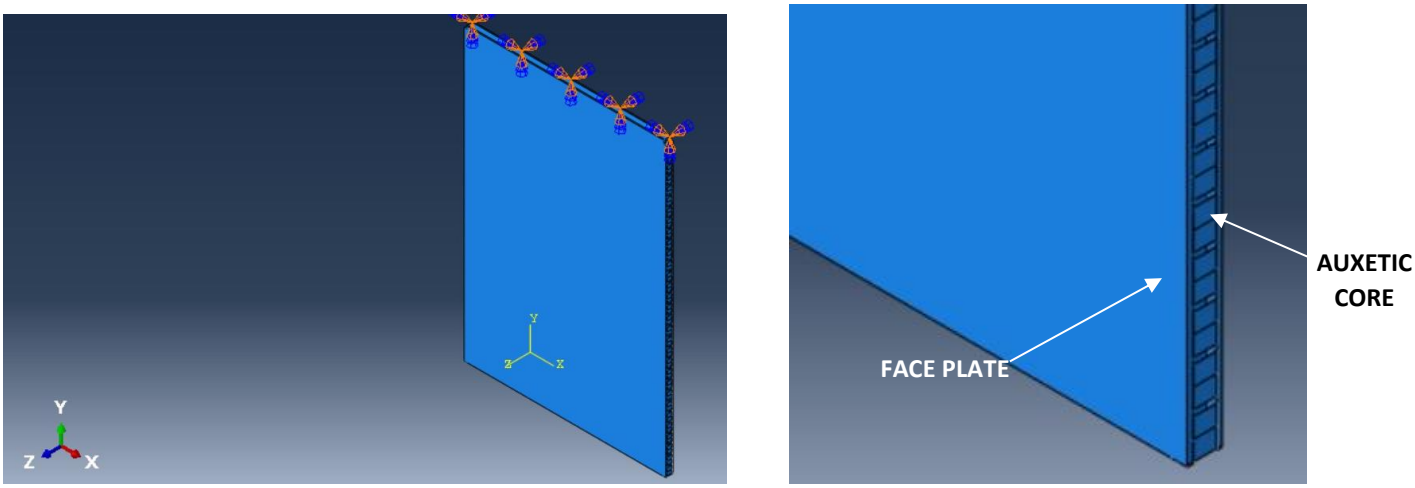

a. **b.**

Fig 7.3. Sandwich composite face plate auxetic core assembly

a. Cantilever support boundary condition

b. Zoomed view of the sandwich composite face plate auxetic core assembly

Length of the sandwich plate was varied. In one of the cases length was 350 mm, width was 250 mm and height was 9 mm with height of face sheet was 1.5 mm each and height of the core was 6 mm. The auxetic core parameters used in all the cases were: -

l_h=Length of re-entrant strut =5mm

h_h=Length of vertical strut=10 mm
t_h =Thickness of strut=0.5 mm
θ_h = Re − entrant angle=-40°

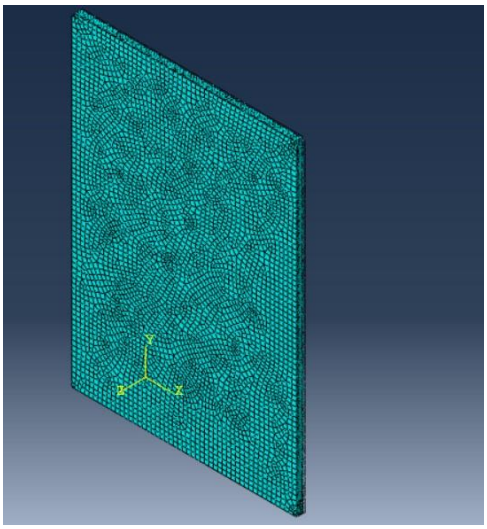

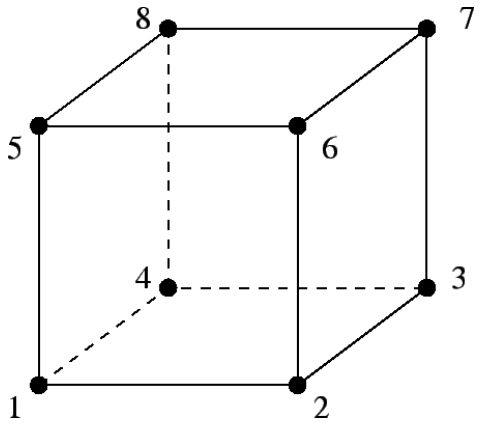

Fig 7.4.a. Mesh in Sandwich structure with auxetic core
b. C3D8R element in ABAQUS™

After simulations, results are shown in figure 7. 5.The natural frequency in this case was 71.786 Hz.

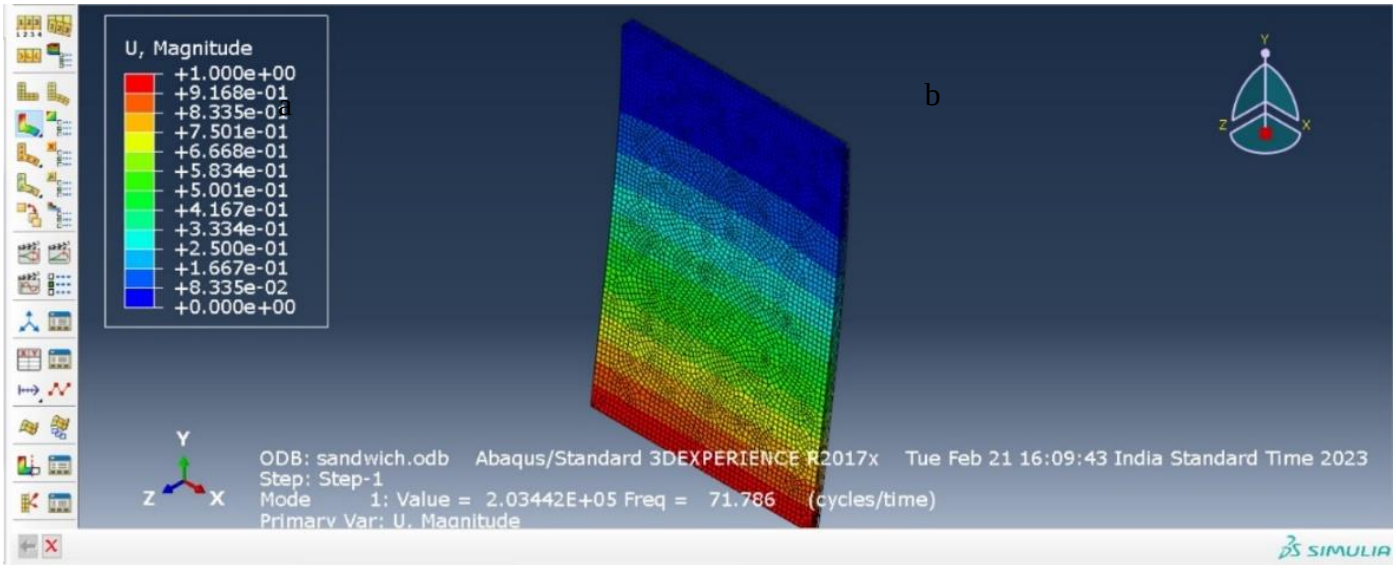

Fig 7.5. ABAQUS™ simulation post processing

CH 8: MANUFACTURE OF HONEYCOMB CORES AND ASSEMBLY OF SANDWICH STRUCTURE

8.1. DEVELOPMENT OF COMPUTER AIDED DESIGN (CAD) MODEL

The CAD models of the non re-entrant and auxetic core are prepared using Dassault CATIA^{TM} software. The following models are shown in the fig.8.1. Two types of cores were designed. Fig8.1. (a) is used for manufacture of auxetic honeycomb core and fig.8.1(b) is used for the manufacturing of manufacturing of non re-entrant honeycomb core.

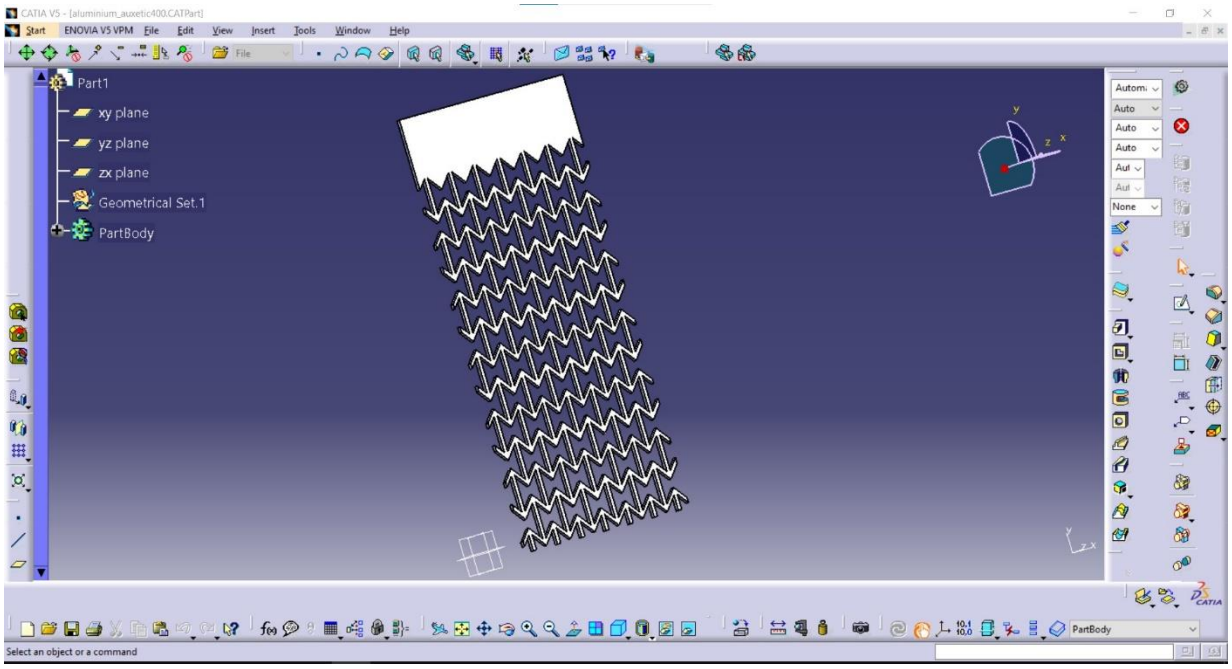

(a)

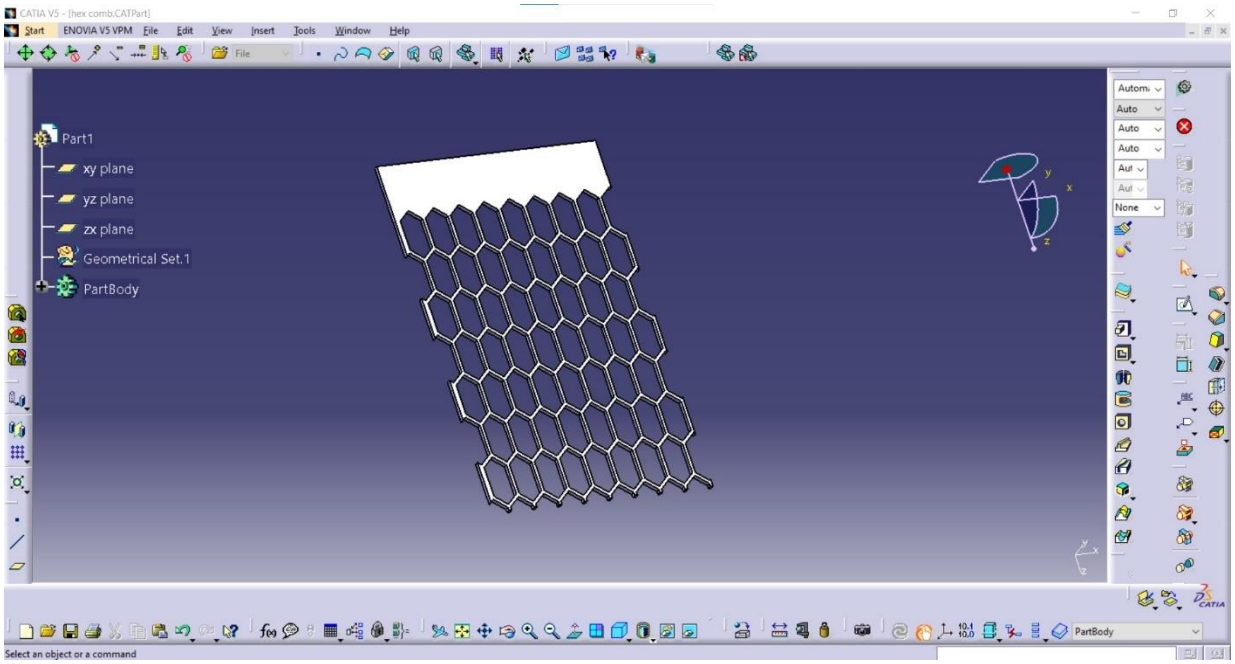

(b)

Figure 8.1.(a)Auxetic Honeycomb core CAD model (b)Non re-entrant Honeycomb core CAD Model

Types of material used for core in various experiments:

1.Polylactic acid polymer core manufactured by FDM method

2.Aluminium metal core manufactured by profile cutting by CNC milling

The face sheets for both the cases were Aluminium.

8.2. POLYLACTIC ACID (PLA) POLYMER CORE

The Polylactic core is first manufactured by FDM 3D printing technology. Then the polymer core is joined by adhesive bonding with two aluminium face sheets on both sides to form the sandwich structure.

8.2.1. FUSED DEPOSITION MODELING

- The Fused Deposition Modelling (FDM) process constructs three-dimensional objects directly from 3D CAD data. A temperature-controlled head extrudes thermoplastic material layer by layer.
- The FDM process starts with importing an STL file of a model into a pre-processing software. This model is oriented and mathematically sliced into horizontal layers varying from +/- t1 thickness to t2 mm thickness (depends on the 3D machine). A support structure is created where needed, based on the part's position and geometry. After reviewing the path data and generating the toolpaths, the data is downloaded to the FDM machine.
- The system operates in X, Y and Z axes, drawing the model one layer at a time. This process is similar to how a hot glue gun extrudes melted beads of glue. The temperature-controlled extrusion head is fed with thermoplastic modelling material that is heated to a semi-liquid state. The head extrudes and directs the material with precision in ultrathin layers onto a fixtureless base. The result of the solidified material laminating to the preceding layer is a plastic 3D model built up one strand at a time. Once the part is completed the support columns are removed and the surface is finished.
- Some of the model material filament types include:
    - Polylactic acid (PLA)
    - Polyethylene Terephthalate Glycol (PETG)
    - Acrylonitrile Butadiene Styrene (ABS)
    - Acrylonitrile Styrene Acrylate (ASA)
    - Nylon (Polyamide, or PA)
- Some of the support material filament types include:
    - SR-30^{TM}
    - SR-100^{TM}
    - SR-110^{TM}

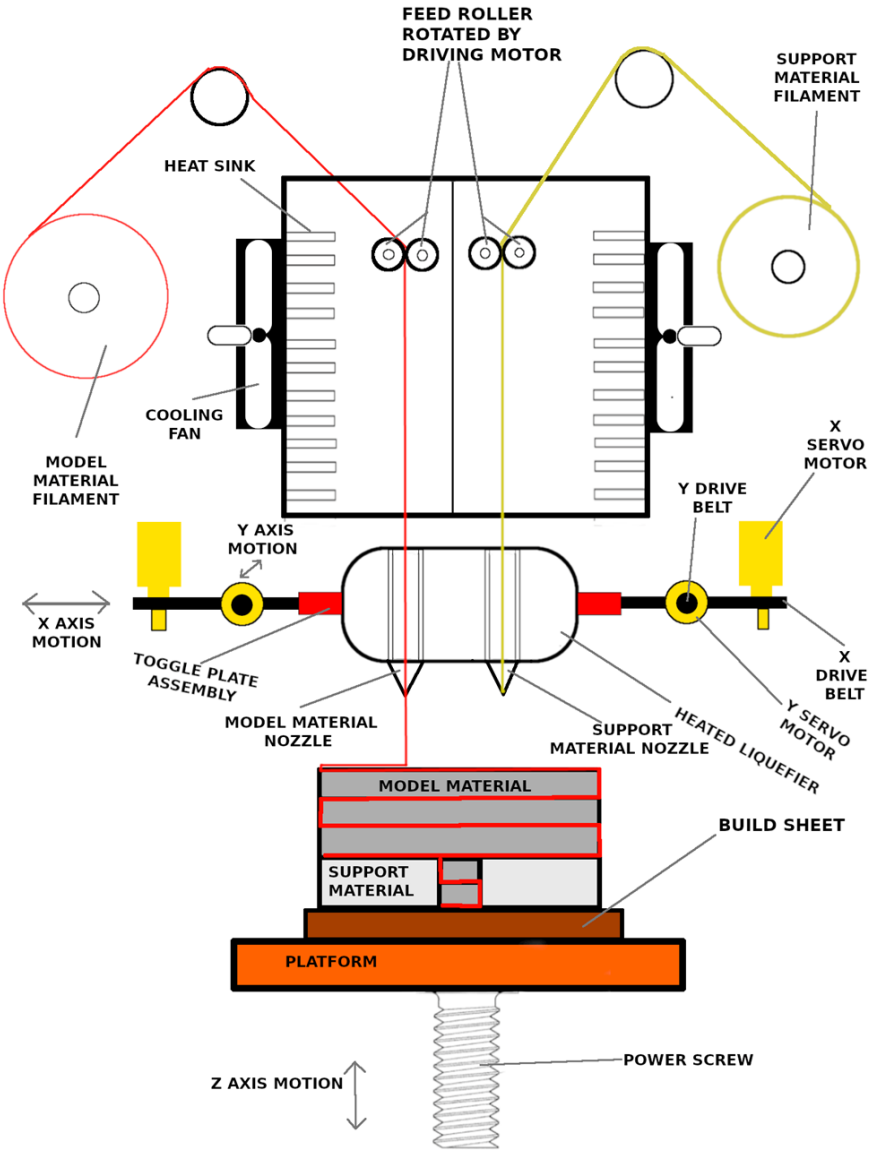

Figure 8.2. Fused Deposition Modeling

8.2.2. ADHESIVE BONDING

Adhesive bonding is a process of joining two or more solid parts with an adhesive substance. The materials of the joined parts (substrates) may be different or similar. Adhesive joint generally consists of two substrate surfaces with the adhesive material filled the gap between them. In our case ,3D printed PLA honeycomb core was attached to two aluminium face sheets on both faces of the core to form the sandwich structure. Fig.8.3(a) shows the structure of the adhesive bond and Fig.8.3(b) shows the assembly process of the sandwich structure prepared for the experiment.

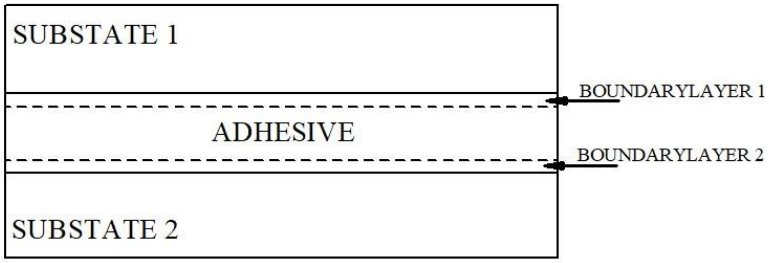

(a)

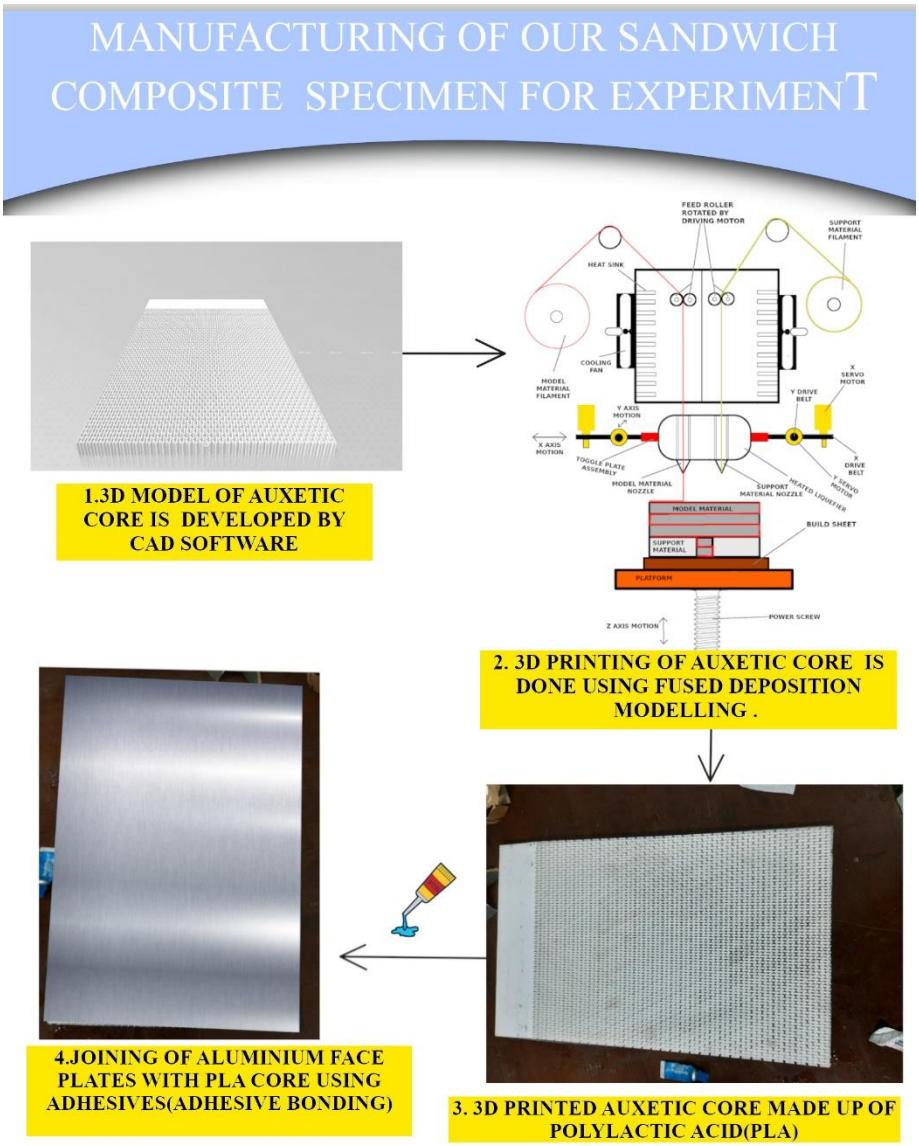

(b)

FIGURE.8.3(a)Structure of Adhesive joints

(b)Manufacturing of sandwich composite specimen with PLA core and aluminium face sheets

8.3. ALUMINIUM METAL CORE

Aluminium metal core was prepared by profile cutting technique based on CAD file exported in .iges format of CNC milling. Then the core was joined with Aluminium face sheets using TIG welding.

8.3.1.CNC MILLING

CNC milling is a machining process that combines computer numerical control machining systems and a multi-point cutting tool or milling cutter. As one type of CNC machining , it

involves mounting the workpiece on a machine bed and cutting materials from a solid block to produce products made of glass, metal, plastic, wood and more specialized materials.

To break it down in the simplest way possible, CNC milling involves a four-step process:

Step 1: Create a CAD model

Machinists use a design program such as Autodesk Fusion 360 to create a CAD model of a specific component.

Step 2: Convert CAD model for CNC machine

Next, import the CAD model into the CAM computer-aided manufacturing system. Done right, you'll end up with a series of digital instructions that tell the CNC machine what to do—otherwise known as G-code. G-code commands let machines identify where to move and how fast to do it to make a specific component.

Step 3: Set-up up the CNC milling machine

Attach the workpiece or block of material on the machine bed—and make sure it's properly aligned through metrology tools or touch probes. Install the machine spindle and do all steps required for setting up the milling machine.

Step 4: Begin the milling process

Load the program to start the CNC milling process. The specialized cutting tools rotate at high speed or a fixed revolution per minute to subtract material from the workpiece—until it accurately replicates the desired component.

Figure 8.4(a) shows manufacturing of re-entrant auxetic core using CNC milling and 8.4(b) shows manufacturing of non re-entrant honeycomb core using CNC milling .

(a)

(b)

Figure 8.4(a)Auxetic core (b) Non re-entrant honeycomb core manufactured by profile cutting using CNC milling

8.3.2. JOINING FACE SHEET USING TIG WELDING

Tungsten inert gas welding, also known as gas tungsten arc welding (GTAW), is a welding process that joins pieces of metal together through a welding current. An inert gas is supplied to the welding torch that flows along the welding arc to protect the metals from oxidation and from forming small circular gaps. A tungsten electrode is assembled within the welding torch, which has a higher melting point than most metals.

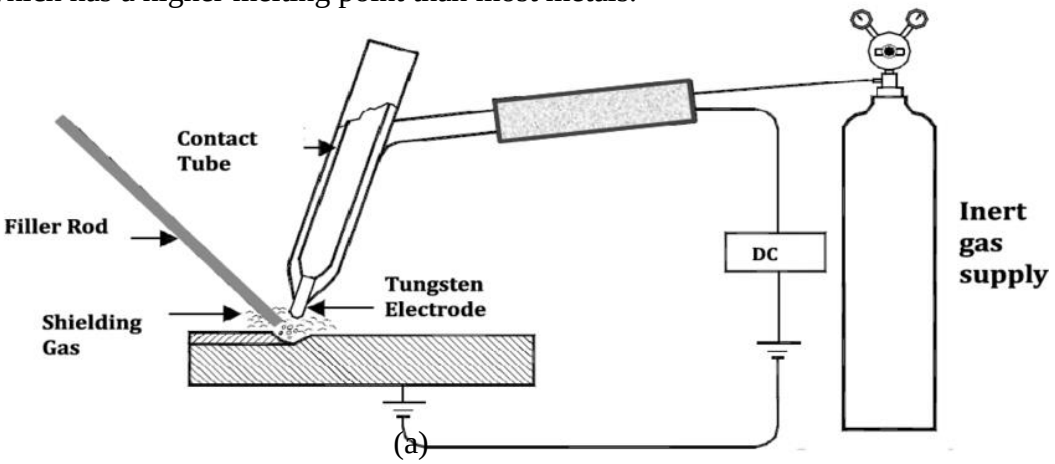

(a)

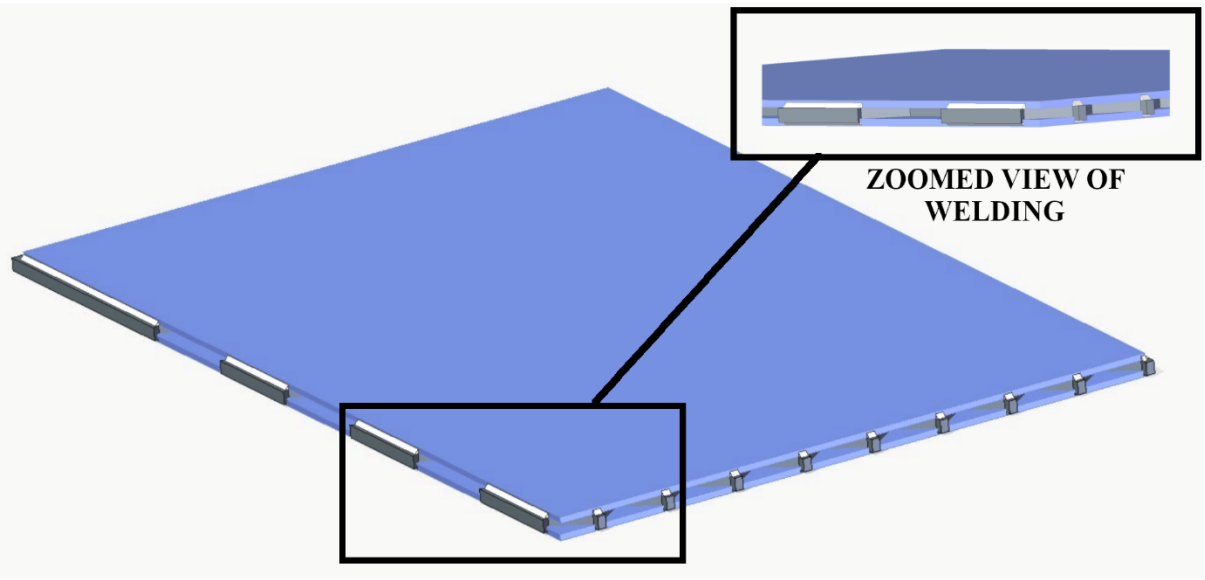

(b)

Figure.8.5(a)Tig Welding (b)Connection weldment model of Honeycomb core with metal plate by stitch welding by TIG welding technique to form metal sandwich structure

Fig.8.5(b) depicts the weldment model of connection of aluminium honeycomb core with aluminium face sheets by stitch welding.

CH 9: EXPERIMENTS

Then once the sandwich composites structure is developed, we starts our vibration testing to find the natural frequency. We fitted the specimen to a cantilever support. The specimen was hit by an impact hammer. Then the vibration response was captured by the analyser and using a software Fast Fourier Transform(FFT) was performed on the vibration responses that were obtained .The peak represented the point where the natural frequency of the specimen could be found .The experimental setup and the process of our experiment is illustrated below in the fig.9.1

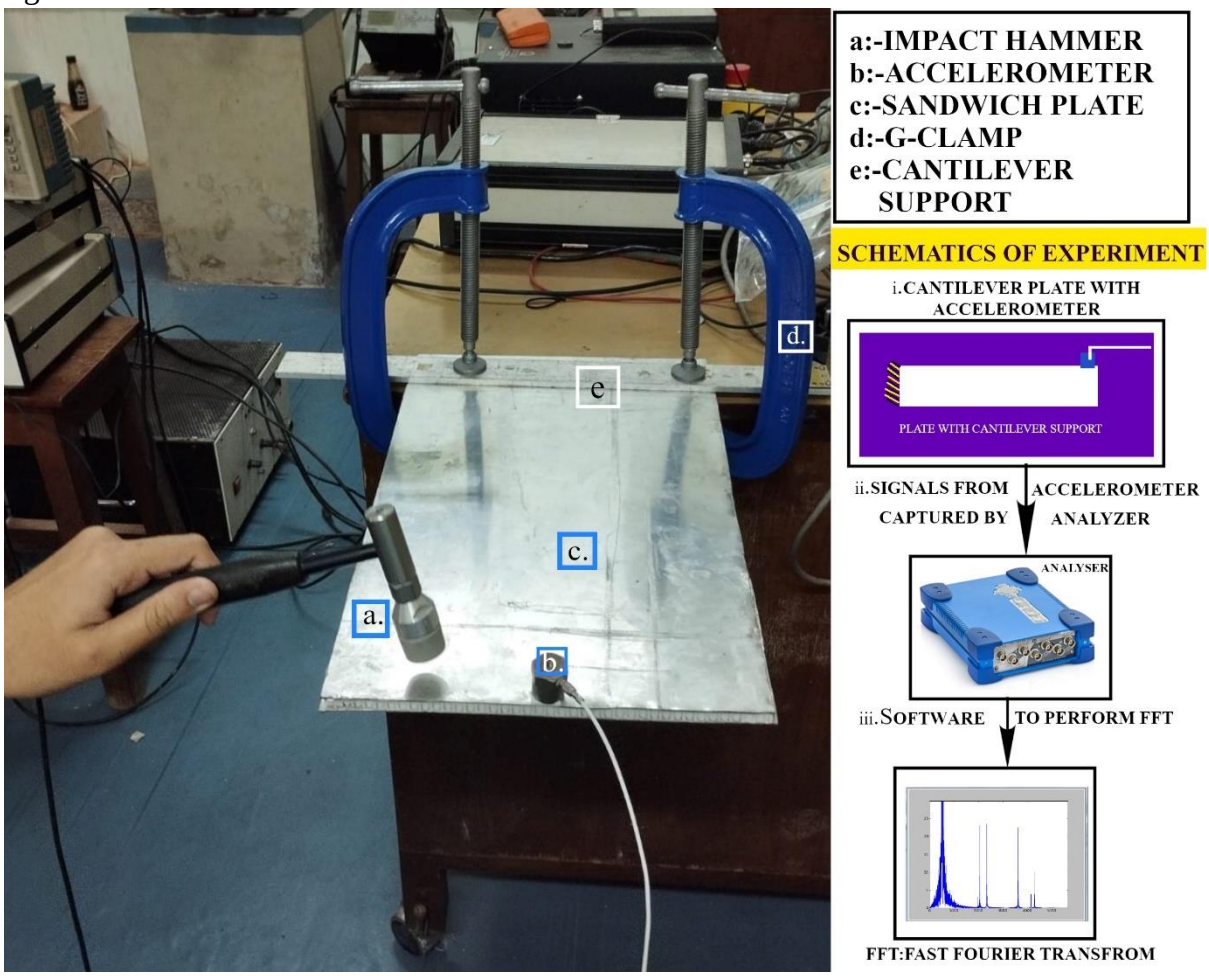

.

Figure.9.1. Experimental setup and procedure

9.1.IMPACT HAMMER FOR EXPERIMENTAL MODAL ANALYSIS

Modal testing is the form of vibration testing of an object whereby the natural (modal) frequencies, modal masses, modal damping ratios and mode shapes of the object under test are determined. A modal test consists of an acquisition phase and an analysis phase. The complete process is often referred to as a Modal Analysis or Experimental Modal Analysis.

In fig.9.1. impact hammer is marked as (a). A typical impact test will use an impact modal hammer and a response accelerometer. It is important to consider the scale of the test structure when selecting these sensors. The impact hammer imparts an impulse force into the system and is intended to excite a broad bandwidth. The Impact hammers range in size, sensitivity, and hardness depending on the scale of the system they need to excite and the bandwidth of interest.

Similarly, the response accelerometer needs to be sensitive enough to detect the ringing of the structure without saturating. The output of the impact hammer and accelerometer are used to calculate the fast Fourier Transform & frequency response functions (FRFs) across the structure.

9.2.DISCRETE FOURIER TRANSFORM (DFT) AND FAST FOURIER TRANSFORM(FFT) ALGORITHM

Frequency domain analysis and Fourier transforms are a cornerstone of signal and system analysis. These ideas are also one of the conceptual pillars within vibration studies and analysis. Among all of the mathematical tools utilized in modal analysis, frequency domain analysis is arguably the most far-reaching. FFT algorithm has changed the world .FFT very quickly solve numerical partial differential equation, helps to denoise data ,data analysis, vibration analysis ,audio and image compression .

FFT is the algorithm to calculate discrete Fourier transform(DFT).FFT increases the speed to compute DFT. Fourier analysis converts a signal from its original domain (often time or space) to a representation in the frequency domain and vice versa. The DFT is obtained by decomposing a sequence of values into components of different frequencies[36].

9.2.1.DISCRETE FOURIER TRANSFORM(DFT)

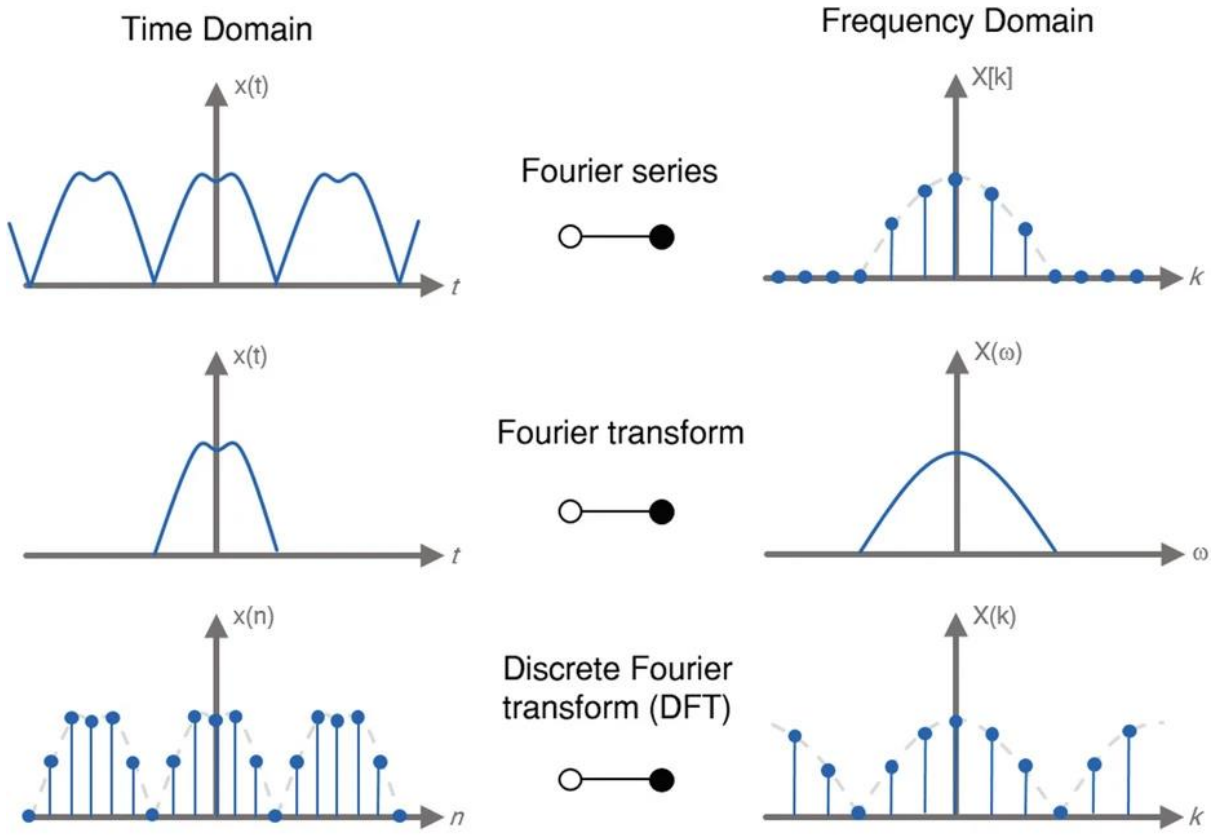

Figure 9.2.Several techniques to convert time domain to frequency domain

Discrete Fourier Transform is a method used to convert time domain to frequency domain .Now DFT is studied for generalised case not only for frequency and time case.

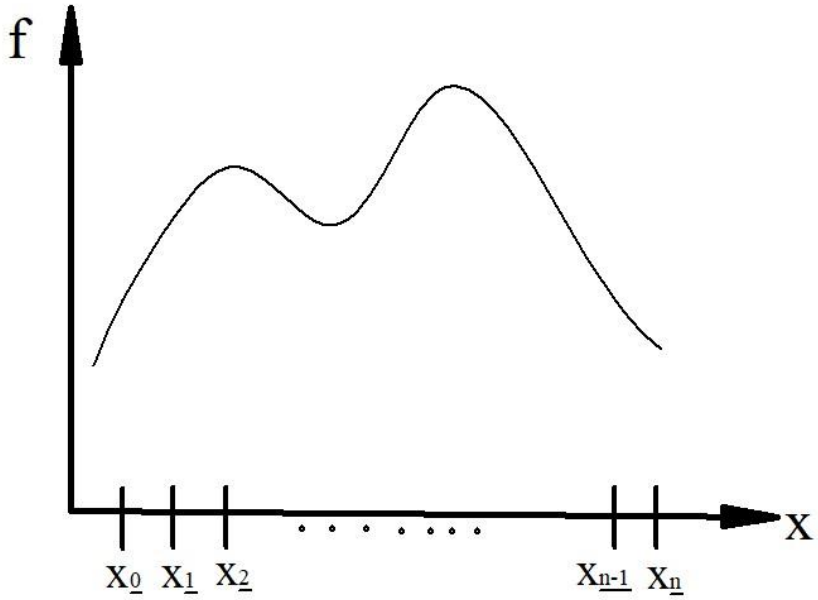

Figure 9.3. some function f vs some random points of independent variables x obtained from experiments.

Sometimes analytical functions are not present but experimental data or simulated data are only present at some discrete locations. From fig 9.3. value of some function f is actually known at some discrete locations $x_0,x_1,x_2,\ldots\ldots,x_{n-1},x_n$.It is actually believed that some continuous function f is present underlying the discrete points of x obtained from the experiment. Now we will break this function f into sines and cosines by DFT.

$$\begin{pmatrix} f_0 \\ f_1 \\ f_2 \\ . \\ . \\ f_n \end{pmatrix} = f \tag{9.1}$$

For each of the data points f_k,we will try to compute Fourier transform vector component:$\hat{f}_k$ which is the frequency component. $\hat{f}_k$ will tell how much of this this frequency is in the data.

n=number of data points

$$\hat{f}_k = \sum_{j=0}^{n-1} f_j e^{-i2\Pi jk/n} \tag{9.2}$$

Where,$i = \sqrt{-1}$

$$f_k = (\sum_{j=0}^{n-1} \hat{f}_j e^{i2\Pi jk/n})/\mathrm{n} \tag{9.3}$$

Where,$i = \sqrt{-1}$

$\{f_0, f_1, , \ldots., f_n\} \Rightarrow \{\hat{f}_0, \hat{f}_1, \ldots., \hat{f}_n\}$ [CONVERSION BY DFT]

$$\begin{pmatrix} \hat{f}_0 \\ \hat{f}_1 \\ \hat{f}_2 \\ . \\ . \\ \hat{f}_n \end{pmatrix} = \hat{f} \tag{9.4}$$

$$\omega_n = e^{-\frac{2\Pi i}{n}} \tag{9.5}$$

Where, ω_n is the fundamental frequency related to what kind of sines and cosines can be approximated to the n discrete data points in domain of x

$$\begin{pmatrix} \hat{f}_0 \\ \hat{f}_1 \\ \hat{f}_2 \\ . \\ . \\ \hat{f}_n \end{pmatrix} = \begin{bmatrix} 1 & 1 & 1 & . & . & 1 \\ 1 & \omega_n & {\omega_n}^2 & . & . & {\omega_n}^{n-1} \\ 1 & {\omega_n}^2 & {\omega_n}^4 & . & . & {\omega_n}^{2(n-1)} \\ . & . & . & . & . & . \\ . & . & . & . & . & . \\ . & . & . & . & . & . \\ 1 & {\omega_n}^{n-1} & {\omega_n}^{2(n-1)} & {\omega_n}^{3(n-1)} & . & {\omega_n}^{(n-1)^2} \end{bmatrix} \begin{pmatrix} f_0 \\ f_1 \\ f_2 \\ . \\ . \\ f_n \end{pmatrix} \tag{9.6}$$

$$\hat{f} = [F]_n \, f \tag{9.7}$$

Where n=number of rows and n=number of columns

$[F]_n$ is n x n matrix

$$\begin{bmatrix} 1 & 1 & 1 & . & . & 1 \\ 1 & \omega_n & {\omega_n}^2 & . & . & {\omega_n}^{n-1} \\ 1 & {\omega_n}^2 & {\omega_n}^4 & . & . & {\omega_n}^{2(n-1)} \\ . & . & . & . & . & . \\ . & . & . & . & . & . \\ . & . & . & . & . & . \\ 1 & {\omega_n}^{n-1} & {\omega_n}^{2(n-1)} & {\omega_n}^{3(n-1)} & . & {\omega_n}^{(n-1)^2} \end{bmatrix} = [F]_n = DFT\ MATRIX \tag{9.8}$$

DFT MATRIX is a complex matrix and also a symmetric matrix.

$\hat{f}$ are complex values

Thus $\hat{f}$ not only tells the frequency value of each mode but also tells about the phase. Magnitude of elements of $\hat{f}$ matrix tells about the frequency magnitude of first ,second,…nth modes and the argument of the complex numbers tells the phase between sine and cosine of the x.

This DFT matrix is very computationally intensive so FFT is resorted to make the equation quickly solvable.

9.2.2.FAST FOURIER TRANSFORM FOR FAST SOLUTION

DFT is never calculated without the FFT algorithm. If eq.9.6 is directly used to calculate Discrete Fourier Transform ,it will take very long time .The computational complexity of the above algorithm is $O(n^2)$ *where n is the number of data points chosen*.If FFT algorithm is used ,efficiency and speed of the computation will improve drastically. The computational complexity of FFT algorithm is $O(n \log_2 n)$ and if n is higher then effect of $\log_2 n$ is negligible.

Now basic understanding of FFT algorithm approach is stipulated below without going into the intensive mathematics. This is an attempt to delve into what actually is FFT doing without going deep into the mathematical complexity. We will understand FFT algorithm with an example.

Suppose, n=2^{10}=1024

Now from equation 9.7,

$\hat{f}=[F]_{1024}\, f$

Now in FFT ,the reorganisation of DFT matrix [F] is done to make the computation simple and fast and f is reorganised as $f=\begin{pmatrix} f_{even} \\ f_{odd} \end{pmatrix}$

$f_{even} = \{f_2, f_4, f_6, f_8, \dots\dots.\}^T$ (9.9)

$f_{odd} = \{f_1, f_3, f_5, f_7, \dots\dots.\}^T$

$\hat{f}=[F]_{1024}\, f=\begin{bmatrix} I_{512} & -D_{512} \\ I_{512} & -D_{512} \end{bmatrix}\begin{bmatrix} F_{512} & 0 \\ 0 & F_{512} \end{bmatrix}\begin{bmatrix} f_{even} \\ f_{odd} \end{bmatrix}$ (9.10)

Where, I_{512}=Identity matrix with 512 rows and 512 column

$$D_{512} = \begin{bmatrix} 1 & 0 & 0 & 0 & 0 & 0 & 0 \\ 0 & \omega_n & 0 & 0 & 0 & 0 & 0 \\ 0 & 0 & {\omega_n}^2 & 0 & 0 & 0 & 0 \\ 0 & 0 & 0 & . & 0 & 0 & 0 \\ 0 & 0 & 0 & 0 & . & 0 & 0 \\ 0 & 0 & 0 & 0 & 0 & . & 0 \\ 0 & 0 & 0 & 0 & 0 & 0 & {\omega_n}^{511} \end{bmatrix}$$

Transformation of $[F]_{1024}$ is done into $\begin{bmatrix} I_{512} & -D_{512} \\ I_{512} & -D_{512} \end{bmatrix}\begin{bmatrix} F_{512} & 0 \\ 0 & F_{512} \end{bmatrix}$ in FFT

In FFT, the above transformation of DFT matrix and reorganisation of terms of f vector reduces the computational complexity and increases the efficiency and reduces the time of computation as diagonal and identity matrix is easy to compute. But we will again split the DFT matrix

$in\ \begin{bmatrix} F_{512} & 0 \\ 0 & F_{512} \end{bmatrix}$, F_{512} is also DFT matrix of n=512 which can be further split into

$F_{512} = \begin{bmatrix} I_{256} & -D_{256} \\ I_{256} & -D_{256} \end{bmatrix}\begin{bmatrix} F_{256} & 0 \\ 0 & F_{256} \end{bmatrix}$.

and this process will go on till F_2.

This makes FFT faster and reduces computational complexity in performing Discrete Fourier Transform.

9.3. USING MPU-6050 SIX-AXIS (GYRO + ACCELEROMETER),ARDUINO AND PYTHON CODE TO PERFORM FFT OF ACCELERATION RECEIVED FROM MPU-6050 [NOT USING ANALYSER EXPERIMENTAL SET UP USED ABOVE]

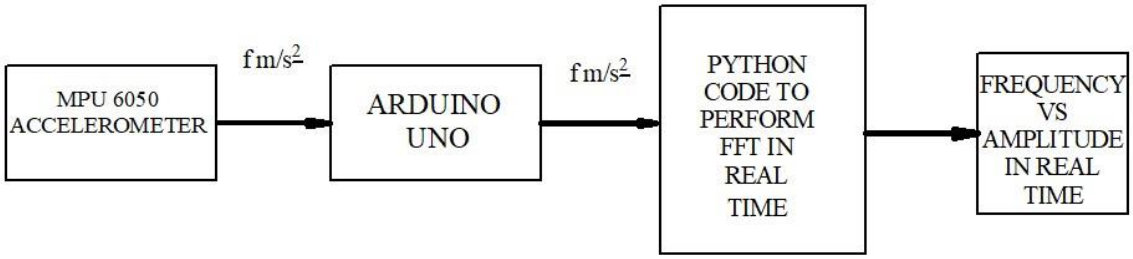

FIGURE 9.4. BLOCK DIAGRAM TO PERFORM FFT USING MPU-6050,ARDUINO UNO AND PYTHON

First, MPU-6050 accelerometer is calibrated. Then it is interfaced with Arduino to capture accelerations of the system in real time. Then Arduino acceleration results are exported to Python environment. Python code is used to perform Fast Fourier Transform on the received acceleration data in real time. Then time vs acceleration and frequency vs amplitude plot are shown in real time on Python GUI. This methodology will help to find the natural frequency of the system.

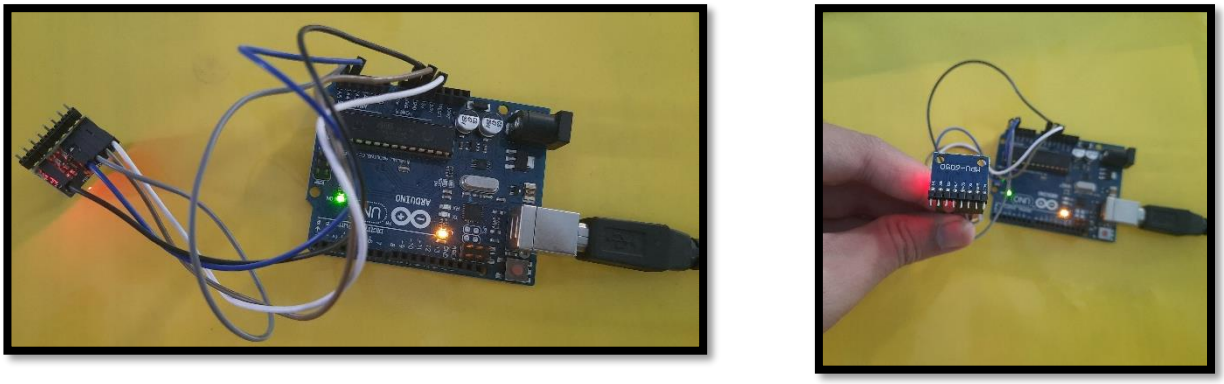

(a) **(b)**

FIGURE 9.5.(a)MPU6050 interfaced with Arduino (b)MPU-6050 Sensor

CH10 : RESULTS AND DISCUSSIONS

10.1 EXPERIMENTS TO DETERMINE THE NATURAL FREQUENCIES OF SANDWICH PANELS

In-house computer codes are developed based on the finite element formulation presented to extract data related to the free vibration response of CNTRC sandwich panels with titanium or aluminium honeycomb core. To validate the codes developed, two set of experiments are initially carried out with re-entrant and non re-entrant honeycomb cores. The first experiment is performed to obtain the natural 2frequencies for different span lengths of a sandwich panel (**Table. 10.1**) comprising of two thin aluminium skins joined using a suitable adhesive to an auxetic honeycomb 100% infused PLA (Poly-lactic acid) core developed using additive manufacturing method on a 3D printing machine (**Fig. 10.1**). In the second experiment, the natural frequencies of two Aluminum-Aluminum sandwich panels comprising of two aluminium skins and a re-entrant (θ_h = +40^0) and a non re-entrant (θ_h = -40^0) honeycomb aluminium core manufactured using CNC milling (**Fig. 10.2**) and adhesively joined together are obtained (**Table.10.2**). The adhesives used are epoxy-based and are assumed to have negligible influence on the vibration outcomes of the developed sandwich panels. The experimental results are found to be in close agreement with the results obtained using the present HSDT based finite element formulation. The suitability of the present FEM codes developed to carry out further analyses is established by their excellent ability in predicting the experimental results.

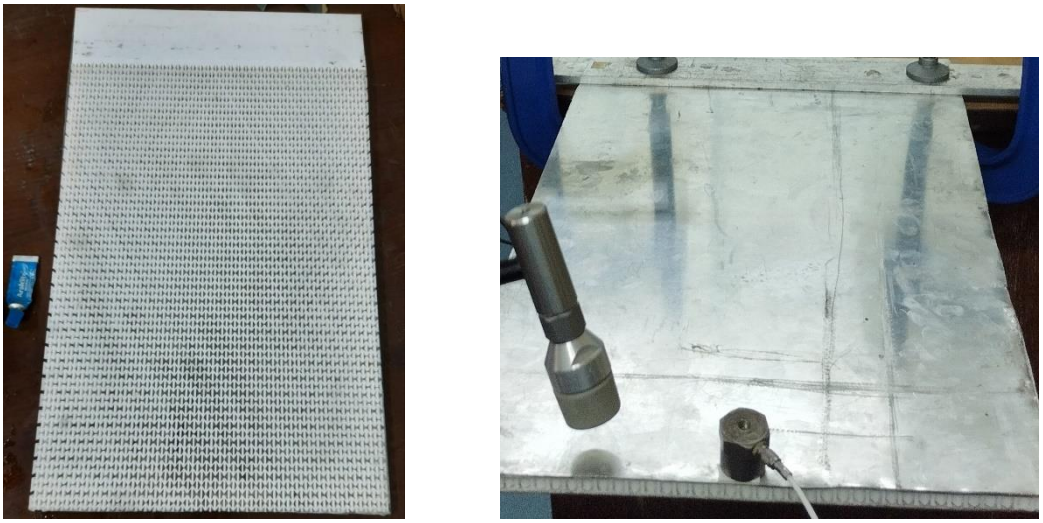

(a) (b)

Fig. 10.1 Photograph of the (a) 3-D printed 100% infused PLA auxetic honeycomb re entrant core, (b) aluminium skin and 100% infused PLA auxetic honeycomb core joined together with adhesive to form the sandwich panel

(a) Re-entrant Auxetic profile cutting

(b) Non re-entrant profile cutting

Fig. 10.2. Photograph of the (a) aluminium auxetic honeycomb re entrant core, (b) aluminium honeycomb non re-entrant core, manufactured by profile cutting using CNC Milling.

Table 10.1: Natural Frequencies (Hz) of cantilever sandwich panel with aluminum face plates and PLA infused auxetic honeycomb core

(h_f=1.5mm, h_c=6mm, h= h_c +2h_f, h_h / l_h =2.0, θ_h=-40^0, E_{pla}=4.107E9, ρ_{pla}=1.24g/cc, ν_{pla}=0.35, E_{Al}=70.0E9, ρ_{Al}=2700g/cc, ν_{Al}=0.30)

Sample Specifications	**Sample 1 (*a*=0.35m, *b*=0.25m)**	**Sample 2 (*a*=0.40m, *b*=0.25m)**	**Sample 3 (*a*=0.45m, *b*=0.25m)**	**Sample 4 (*a*=0.50m, *b*=0.25m)**
Experimental Results (Hz)	76	58	46	37
Current FEM (Hz)	78.89	59.66	46.77	37.66

Table 10.2: Natural Frequencies (Hz) of cantilever sandwich panel with aluminum face plates and non re-entrant auxetic aluminium honeycomb core

(h_f=1mm, h_c=6mm, h= h_c +2h_f, h_h / l_h =2.0, E_{Al}=70.0E9, ρ_{Al}=2700g/cc, ν_{Al}=0.30)

Sample Specifications	***Re-entrant honeycomb (θ_h = -40^0)***		***Non Re-entrant honeycomb (θ_h = 40^0)***	
	Experimental	**FEM**	**Experimental**	**FEM**
Sample 1 (*a*=0.35m, *b*=0.25m)	92	93.92	75	77.47
Sample 2 (*a*=0.40m, *b*=0.25m)	70	71.75	51	54.82
Sample 3 (*a*=0.45m, *b*=0.25m)	55	56.57	27	30.44
Sample 4 (*a*=0.50m, *b*=0.25m)	42	45.73	36	38.84

10.2 VALIDATIONS OF CURRENT FEM WITH ESTABLISHED RESULTS

The present FEM codes are validated with the available free vibration results of sandwich panels with non-honeycomb cores. The natural frequencies of sandwich panels are evaluated and compared with the results of Lei et al. [8] in **Table 10.3**. The non-dimensional natural frequencies of rotating isotropic plates are obtained and compared with the results (**Table 10.4**) obtained by Sreenivasamurthy and Ramamurti for different values of the non-dimensional rotational speed (Ω). The excellent agreement of the current FEM results with the experimental and the published results establishes the correctness and consistency of the present formulation to accurately predict the free vibration response of sandwich panels with honeycomb cores.

Table 10.3: Non-dimensional natural frequencies $\left(\varpi = \omega_n(L^2/h)\sqrt{\rho_{m0}/E_{m0}}\right)$ of FG-CNTRC plates with different CNTs grading patterns in thermal environments $[V^*_{CNT} = 0.12,\ a/b = 1,\ b/h = 10;\ \eta_1 = 0.137,\ \eta_2 = 1.022,\ \eta_3 = 0.715]$

Temp	Mode		Current FEM			Lei *et al.* [8]			
		UD	FG-V	FG-Λ	FG-O	UD	FG-V	FG-Λ	FG-O
300	1	12.368	10.988	13.363	10.167	12.1261	11.3074	13.0235	10.4535
	2	17.077	16.374	17.958	15.872	16.8071	16.2611	19.7496	15.353
500	1	11.114	10.018	11.914	9.299	11.0402	10.2442	11.9171	9.5378
	2	14.571	14.008	15.323	13.887	14.7052	14.2264	18.0036	13.4627
700	1	9.401	8.678	9.968	8.122	9.2518	8.7751	10.7101	8.2728
	2	11.532	11.086	12.127	11.058	11.5159	11.5436	15.8853	11.1033

Table 10.4: Validation of the natural frequencies of rotating isotropic plates (a/b=1, h/a=0.12, ν=0.30)

Non-dimensional Rotational Speed $\Omega = \frac{\omega_z}{\omega_0}$	Sreenivasamurthy and Ramamurti [1]	Current FEM
0.0	3.43685	3.47311
0.2	3.51858	3.55324
0.4	3.75280	3.78192
0.6	4.12875	4.13146
0.8	4.56786	4.56938
1.0	5.09167	5.06909

10.3 VIBRATION INDICATORS OF CNTRC SANDWICH PANELS

The non-dimensional frequencies $\left(\omega_n = \omega\left(\frac{a^2}{h}\right)\sqrt{\frac{\rho_{m0}}{E_{m0}}}\right)$ of sandwich composite panels comprising of CNT reinforced carbon-fiber composite top and bottom facesheets and an isotropic Titanium alloy (***Ti-6Al-4V***) based honeycomb core are presented. The span and the chord length of the sandwich panel are represented by '***a***' and '***b***' respectively, while the thickness of the face sheets and the honeycomb core are denoted by h_s and h_c respectively (**Fig.6.1**). The total thickness of the sandwich panel is thereby $h = h_c + 2h_f$. Two different aspect ratios of a/h= 10 and 50 are considered in the present work which borders close to the moderately thick and moderately thin sandwich panels. A core to factsheets thickness ratio of $\frac{h_c}{h_f} = 8$ is considered in general, unless otherwise mentioned, which accounts for an 80% thick core enveloped by two thin faceplates each comprising of 10% of total thickness of the

sandwich panel. The present study considers different grading patterns of the CNT reinforced face plates (UD, FG-V, FG- **Λ**, FG-O and FG-X) based on which gradation in the volume fractions of the CNT nanoparticles are assumed to be varied across the thickness of the honeycomb sandwich panel. The properties of the PMMA matrix at the base temperature of T=300K are used for calculation of the non-dimensional frequencies since the material properties of the PMMA matrix are highly dependent on the absolute value of the operating temperature. **Table 10.5** lists the temperature based properties CNT nanoparticles [8]. Titanium alloy (Ti-6Al-4V) is considered as homogeneous core with the following material properties at an operating temperature of $\boldsymbol{T}$ [9]: $E_c = 122.56(1 - 4.586 \times 10^{-4}T)$ GPa, $\nu_c = 0.29$, $\rho_c =$ 4429 kg/m^3, and $\alpha_c = 7.5788(1 + 6.638 \times 10^{-4}T - 3.147 \times 10^{-4}T^2) \times 10^{-6}$/K. The face sheets are assumed to be manufactured of poly-methyl methacrylate (PMMA) and (10, 10) armchair SWCNTs as the matrix with reinforcing constituents for the CNTRC face sheets. The temperature-dependent material properties of PMMA are [9]: $E^m = (3.52 - 0.0034T)$ GPa, $\nu^m = 0.34$, $\rho^m = 1150$ kg/m^3, and $\alpha^m = 45.0(1 + 0.0005\Delta T) \times 10^{-6}$/K, where $T =$ 300K. The effectiveness parameters of the SWCNT are taken to be (η_1=0.137, η_2=1.022, η_3=0.715) for λ_{CNT}=0.12; (η_1=0.142, η_2=1.626, η_3=1.138) for λ_{CNT}=0.17; and (η_1=0.141, η_2=1.585, η_3=1.109) for λ_{CNT}=0.28, respectively, where λ_{CNT} denotes the volume fraction of CNT reinforcements. In case of rotating sandwich panel, a parameter named non-dimensional rotational speed ($\Omega = \frac{\omega_z}{\omega_0}$) is defined that relates the actual rotational speed in rad/s (ω_z) of the rotating sandwich panel with circular frequency at resonance of the non-rotating sandwich panel (ω_0).

Table 10.5: Material properties of SWCNTs at different levels of temperature [10] (L= 9.26 nm, R = 0.68 nm, h = 0.067 nm, ν_{12}^{CNT}= 0.175, ρ_{CNT} = 1400 kg/m^3)

Temp, T (K)	E_{11}^{CNT} **(GPa)**	E_{22}^{CNT} **(GPa)**	G_{12}^{CNT} **(GPa)**	α_{11}^{CNT} **(10^{-6}/K)**	α_{22}^{CNT} **(10^{-6}/K)**
300	5646.6	7080.0	1944.5	3.4584	5.1682
400	5567.9	6981.4	1970.3	4.1496	5.0905
500	5530.8	6934.8	1964.3	4.5361	5.0189
700	5474.4	6864.1	1964.4	4.8877	4.8943

10.4 NATURAL FREQUENCIES OF CNTRC COMPOSITE HONEYCOMB PLATES

10.4.1 INFLUENCE OF NON RE-ENTRANT AND RE-ENTRANT ANGLE IN HONEYCOMB CORES

The cellular structure of the honeycomb core plays a significant role on the properties and strength of the sandwich panel made from re-entrant auxetic (Negative Poisson's ratio, NPR) and non re-entrant (non-negative Poisson's ratio) honeycomb cores. The variations in the effective Elastic Modulus (E_1), Poisson's ratio and the density for different combinations of the inclined angle ($\boldsymbol{\theta_h}$) and the length to thickness of the honeycomb ribs (h_h/l_h) are plotted in **Fig. 10.3**, **Fig. 10.4** and **Fig. 10.5**, respectively. The Young's Modulus of both re-entrant and the non re-entrant honeycomb cores are found to decrease with an increase in the absolute value of the inclined angle ($|\pm\boldsymbol{\theta_h}|$) while the reverse trend is observed in case of the density of the honeycomb core. Both the Young's Modulus and density values are found to be higher in case of re-entrant inclined angle (Auxetic case) compared to the non re-entrant inclined angle for

corresponding absolute values of the inclined angle. The re-entrant inclined angle (**$-\theta_h$**) displays negative Poisson's ratio and the absolute value of the negative Poisson's ratio is found to decrease with an increase in the absolute value of the auxetic inclined angle (**$|-\theta_h|$**). In contrast, the non re-entrant inclined angle displays positive Poisson's ratio as most engineering materials in use which decreases with an increase in the inclined angle (**$+\theta_h$**). The non-dimensional first and second natural frequencies $\left(\omega_n = \omega\left(\frac{a^2}{h}\right)\sqrt{\frac{\rho_{m0}}{E_{m0}}}\right)$ of composite (0/90/0/90/0/**core**/0/90/0/90/0) sandwich panels made of PMMA matrix reinforced with CNT as face-sheets and Titanium based-alloy (***Ti-6Al-4V***) as the honeycomb core are presented in **Fig. 10.6** for both re-entrant and non re-entrant honeycomb cores. The non-dimensional frequencies are found to be lower in case of re-entrant (auxetic) included angle in comparison to the non re-entrant angle for all the five CNT distribution patterns considered. This may be explained from the fact that the effective density of the re-entrant angle honeycomb are much higher in magnitude than the non re-entrant angle honeycomb which results in a lower non-dimensional natural frequency in the re-entrant angle honeycomb (**Fig. 10.5**) for a certain value of the inclined angle. With an increase in the absolute inclined angle (**$|\pm\theta_h|$**), a decrease in the non-dimensional frequency is observed in both the re-entrant and the non re-entrant honeycomb irrespective of the CNT distribution pattern. An increase in the inclined angle results in a decrease in the Young's Modulus which results in a corresponding decrease in the stiffness of both the re-entrant and the non re-entrant honeycomb core sandwich panels. For a certain value of the inclined angle (**$|\pm\theta_h|$**) in general, the highest value of both the first and second natural frequencies is observed for the FG-X pattern of CNT distribution while the least value is observed for FG-O distribution pattern.

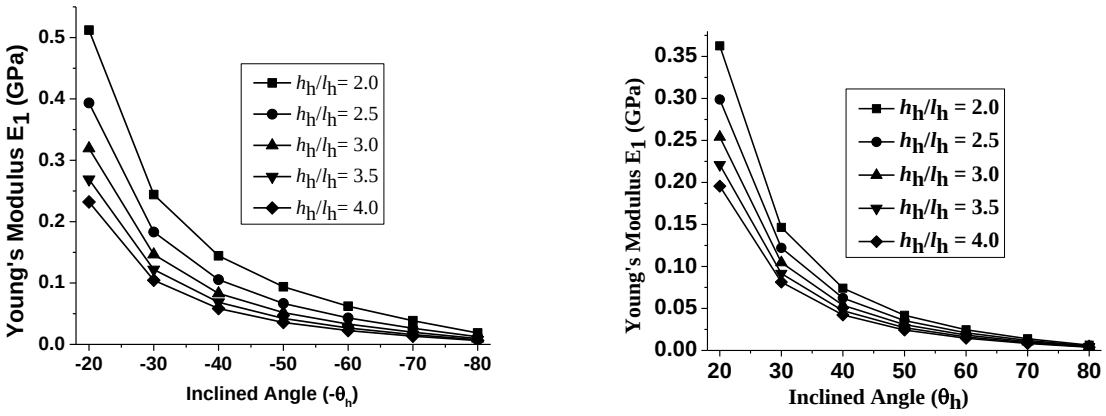

(a) Re-entrant Core ($-\theta_h$) (b) Non Re-entrant Core ($+\theta_h$)

Fig. 10.3. Plot of variations of the effective Young's Modulus (E_1) of the honeycomb core for different combinations of the inclined angle (**$\pm\theta_h$**) and the length to thickness ratio (h_h/l_h) for re-entrant and non re-entrant cores

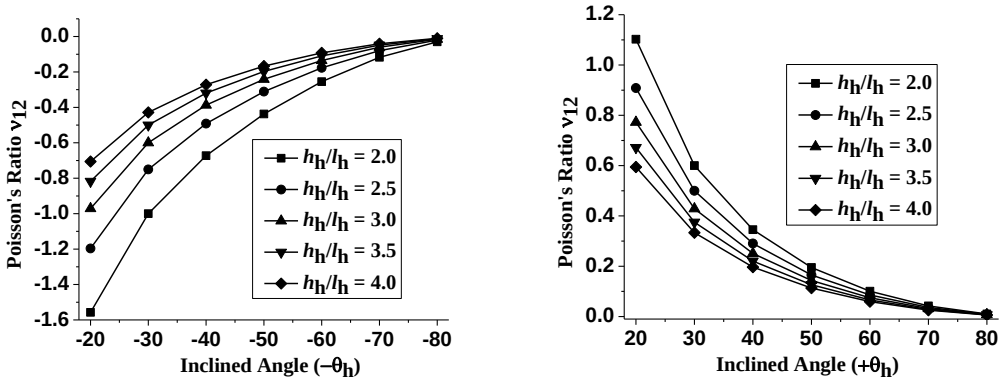

a) Re Entrant Core (-θ_h) (b) Non Re-entrant Core (+θ_h)

Fig. 10.4 Plot of variations of the effective Poisson's Ratio (v_{12}) of the honeycomb core for different combinations of the inclined angle ($\pm\theta_h$) and the length to thickness ratio (h_h/l_h) for re-entrant and non re-entrant cores

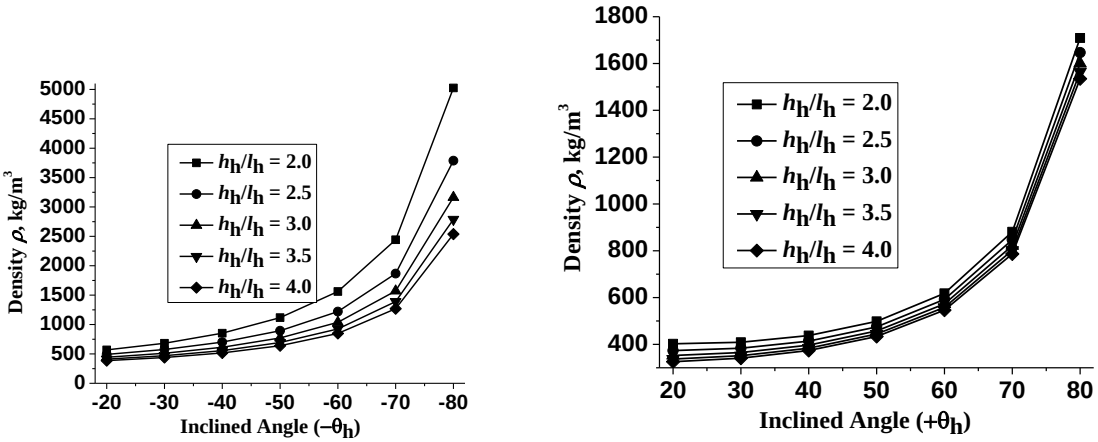

(a) Re-entrant Core (-θ_h) (b) Non Re-entrant Core (+θ_h)

Fig. 10.5 Plot of the variations on the effective density (ρ) of the honeycomb core for different combinations of the inclined angle ($\pm\theta_h$) and the length to thickness ratio (h_h/l_h) for re entrant and non re-entrant cores

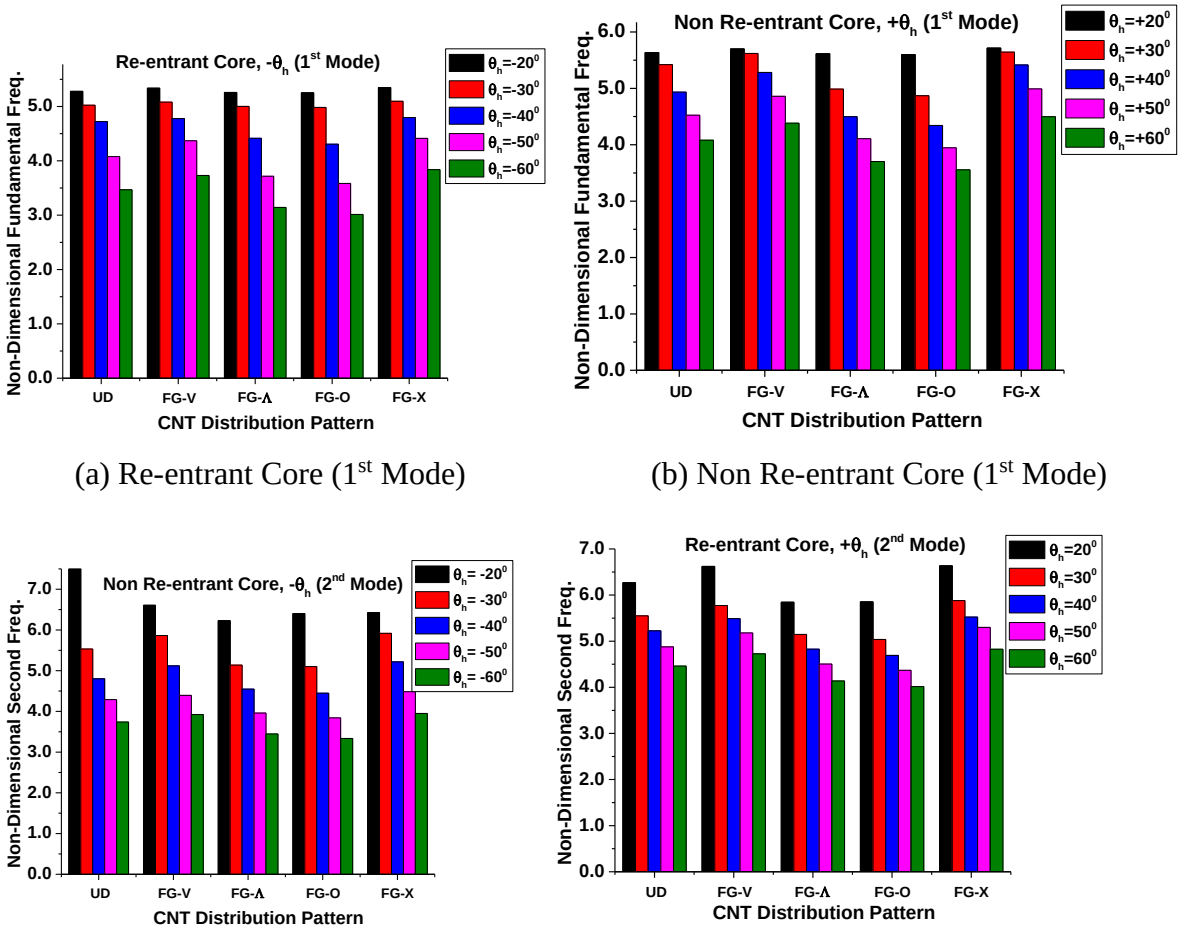

(a) Re-entrant Core (1st Mode) (b) Non Re-entrant Core (1st Mode)

(c) Re-entrant Core (2nd Mode) (d) Non Re-entrant Core (2nd Mode)

Fig. 10.6. Non-dimensional Frequencies $\left(\omega_n = \omega\left(\frac{a^2}{h}\right)\sqrt{\frac{\rho_{m0}}{E_{m0}}}\right)$ of CNTRC composite skin CNT reinforced PMMA (0/90/0/90/0/**core**/0/90/0/90/0) composite skin and honeycomb core comprising of ***Ti-6Al-4V honeycomb*** sandwich plates **at room temperature (*T*=300K)** (a/b=1, a/h=10, h_c/h_f=8, h= h_c +2h_f, h_h / l_h =2.0, λ_{CNT}=0.12)

10.4.2 INFLUENCE OF CORE MATERIAL AND PANEL ASPECT RATIO

The non-dimensional frequencies $\left(\omega_n = \omega\left(\frac{a^2}{h}\right)\sqrt{\frac{\rho_{m0}}{E_{m0}}}\right)$ of composite sandwich panels made of PMMA matrix reinforced with CNT composite face-sheets and a Titanium based-alloy (Ti-6Al-4V) and commercial grade aluminium alloy as the honeycomb core are presented in **Table 10.6, Table 10.7**, **Table 10.8 and Table 10.9,** for both re-entrant auxetic (θ_h**=-40^0**) and non re-entrant (θ_h**=+40^0**) honeycomb core types, respectively. The results are presented for two aspect ratios (a/h) of 10 and 50 of the sandwich panel. The natural frequencies of the sandwich panel are observed to be higher for relatively soft aluminium core compared to the titanium core for all combinations of the panel aspect ratio and the CNT distribution patterns. This may be explained based on spring analogy wherein the cores may be assumed to be acting as springs supporting the top and the bottom face sheet plates. The high stiffness combined with lower density of the aluminium core compared to the titanium core results in higher natural frequencies in the aluminium core sandwich panel compared to the titanium core one. As expected, an increase in the non-dimensional frequencies is observed for both the core types

(Ti-6Al-4V core and aluminium core) with an increase in the volume fraction of CNT (λ_{CNT} = 0.12, 0.17 and 0.28) which is clearly an effect of the strengthened sandwich faceplates composed of CNT reinforced PMMA matrix. For all the CNT distribution patterns considered, the highest value of the non-dimensional first and second frequencies is observed for FG-X followed by the FG-V, UD, FG-Λ and FG-O patterns for a particular CNT volume fraction in both the core types considered. This is quite convincing since the carbon nanotube reinforcements are mainly distributed closer to the outer fibers in case of FG-X and FG-V variation patterns (**Fig.6.1**), which experiences the highest stress under spanwise bending resulting in a higher stiffness in such sandwich panels. Conversely, the FG-O pattern that has higher reinforcement density close to the mid-plane or neutral surface that experiences insignificant bending stresses exhibits the lowest natural frequencies of all the grading patterns considered. In addition, an increase in the aspect ratio of the sandwich panel results in an increase in both the first and the second non-dimensional frequencies owing to the fact that an increase in the span length for a certain thickness of the sandwich panel results in a subsequent stiffness increment. This is again augmented by the fact that an increase in the aspect ratio results in an increase in the structural stiffness of the cantilever sandwich panel owing to higher flexibility in the cantilever structure.

Table 10.6 Non-dimensional fundamental Frequencies $\left(\omega_n = \omega\left(\frac{a^2}{h}\right)\sqrt{\frac{\rho_{m0}}{E_{m0}}}\right)$ of CNTRC (0/90/**core**/0/90) composite skin CNT reinforced PMMA skin and honeycomb core (θ_h=-40^0) comprising of ***Ti-6Al-4V honeycomb*** and Commercial grade ***Aluminum honeycomb*** sandwich plates **at room temperature (*T*=300K)**
(a/b=1, h_c/h_f=8, h= h_c +2h_f, h_h / l_h =2.0, θ_h=-40^0, E_{Al}=70.0E9, ρ_{Al}=2700g/cc, ν_{Al}=0.30)

θ_h	*a/h*	*CNT Distribution Pattern*	Ti-6Al-4V core			Aluminum Core		
			0.12	**0.17**	**0.28**	**0.12**	**0.17**	**0.28**
-40^0 (Mode 1)	**10**	UD	4.198	5.374	5.705	4.958	6.364	6.759
		FG V	4.194	5.344	6.069	5.126	6.653	7.833
		FG Λ	2.844	3.323	3.512	3.270	3.781	3.994
		FG O	2.256	2.637	2.695	2.578	3.023	3.087
		FG X	4.524	6.026	7.225	5.328	7.099	8.442
	50	UD	6.001	7.154	8.546	7.030	8.395	10.027
		FG V	6.104	7.311	8.792	7.164	8.603	10.369
		FG Λ	3.445	4.155	4.3812	4.023	4.866	5.129
		FG O	2.878	3.412	3.492	3.348	3.982	4.074
		FG X	7.719	9.197	11.201	9.041	10.793	13.154

Table 10.7. Non-dimensional Second Frequencies $\left(\omega_n = \omega\left(\frac{a^2}{h}\right)\sqrt{\frac{\rho_{m0}}{E_{m0}}}\right)$ of CNTRC (0/90/**core**/0/90) composite skin CNT reinforced PMMA skin and honeycomb core (θ_h=-40^0) comprising of ***Ti-6Al-4V*** and Commercial grade ***Aluminum*** sandwich panels **at room temperature (*T*=300K)** (a/b=1, h_c/h_f=8, h= h_c +2h_f, h_h / l_h =2.0, θ_h=-40^0, E_{Al}=70.0E9, ρ_{Al}=2700g/cc, ν_{Al}=0.30)

θ_h	*a/h*	*CNT Distribution Pattern*	Ti-6Al-4V core			Aluminum Core		
			0.12	**0.17**	**0.28**	**0.12**	**0.17**	**0.28**
-40^0	**10**	UD	4.843	5.754	6.782	5.625	6.668	7.799
		FG V	4.938	5.949	6.974	5.762	6.941	8.108

(Mode 2)		FG Λ	2.875	3.432	3.625	3.298	3.989	4.212
		FG O	2.458	2.972	2.986	2.856	3.461	3.476
		FG X	6.143	7.253	8.521	7.079	8.308	9.752
	50	UD	7.295	8.560	10.292	6.964	8.330	9.898
		FG V	7.414	8.709	10.453	5.639	6.848	8.095
		FG Λ	3.757	4.402	4.674	3.373	3.784	3.952
		FG O	2.908	3.529	3.556	2.582	2.936	3.003
		FG X	9.454	11.061	13.327	8.898	10.691	13.071

Table 10.8. Non-dimensional fundamental Frequencies $\left(\omega_n = \omega\left(\frac{a^2}{h}\right)\sqrt{\frac{\rho_{m0}}{E_{m0}}}\right)$ of CNTRC (0/90/**core**/0/90) composite skin CNT reinforced PMMA skin and non-re-entrant honeycomb core (θ_h=**40^0**) comprising of ***Ti-6Al-4V honeycomb*** and Commercial grade ***Aluminum honeycomb*** sandwich plates **at room temperature (*T*=**300K)
(a/b=1, h_c/h_f=8, h=h_c +2h_f, h_h/ l_h =2.0, θ_h=40^{0,} E_{Al}=70.0E9, ρ_{Al}=2700g/cc, ν_{Al}=0.30)

θ_h	*a/h*	*Mode 1*	**Ti-6Al-4V core**			**Aluminum Core**		
			0.12	**0.17**	**0.28**	**0.12**	**0.17**	**0.28**
40^0	**10**	UD	4.964	5.778	6.886	5.469	6.366	7.527
		FG V	3.772	4.387	5.199	4.170	4.882	5.809
		FG Λ	2.187	2.419	2.517	2.376	2.641	2.750
		FG O	1.727	1.934	1.973	1.889	2.123	2.164
		FG X	5.744	7.381	8.696	6.489	8.034	9.349
	50	UD	6.19	7.376	8.755	8.106	9.402	11.159
		FG V	5.017	6.066	7.150	6.181	7.214	8.567
		FG Λ	3.011	3.367	3.516	3.948	4.728	4.906
		FG O	2.297	2.601	2.658	3.538	4.259	4.257
		FG X	7.891	9.450	11.548	10.327	11.969	14.274

Table 10.9. Non-dimensional Second Frequencies $\left(\omega_n = \omega\left(\frac{a^2}{h}\right)\sqrt{\frac{\rho_{m0}}{E_{m0}}}\right)$ of CNTRC (0/90/**core**/0/90) composite skin CNT reinforced (0/90/core/0/90) composite PMMA skin and non re-entrant (θ_h=40^0) honeycomb core comprising of ***Ti-6Al-4V*** and Commercial grade ***Aluminum*** sandwich panels **at room temperature (*T*=300K)**
(a/b=1, h_c/h_f=8, h=h_c +2h_f, h_h/ l_h =2.0, θ_h=-40^0, E_{Al}=70.0E9, ρ_{Al}=2700g/cc, ν_{Al}=0.30)

θ_h	*a/h*	*Mode 2*	**Ti-6Al-4V core**			**Aluminum Core**		
			0.12	**0.17**	**0.28**	**0.12**	**0.17**	**0.28**
40^0	**10**	UD	5.138	6.124	7.143	5.752	6.805	7.867
		FG V	4.085	4.991	5.895	4.614	5.626	6.624
		FG Λ	2.843	3.423	3.569	3.188	3.845	4.004
		FG O	2.563	3.083	3.079	2.877	3.471	3.467
		FG X	6.379	7.533	8.889	6.974	8.347	9.637
	50	UD	7.219	8.358	9.945	8.397	9.762	11.583

		FG V	5.484	6.383	7.571	6.404	7.497	8.924
		FG Λ	3.516	4.199	4.359	4.075	4.886	5.071
		FG O	3.136	3.768	3.767	3.651	4.399	4.397
		FG X	9.237	10.669	12.712	10.692	12.427	14.845

10.4.3 INFLUENCE OF TWIST ANGLE AND OPERATING TEMPERATURE

The non-dimensional first and the second natural frequencies of carbon-nanotube reinforced (0/90/0/90/0/core/0/90/0/90/0) composite sandwich panels made from PMMA matrix reinforced by CNT's and a metallic Titanium alloy based (*Ti-6Al-4V*) honeycomb auxetic (θ_h =-40^0) core are presented in **Table 10.10 and Table 10.11** for different twist angles (ϕ = 0^0, 15^0 and 30^0) and operating temperatures (T=300K, 500K and 700K). It is observed that there is a reduction in the non-dimensional fundamental frequencies with an increase in the twist angle (ϕ) while the reverse is generally observed in case of the second natural frequencies. In general, the twist angle results in a reduction in the structural stiffness of the sandwich panel. In case of cantilever sandwich panels, the fundamental frequencies correspond to the bending mode while the second frequencies denote the torsional mode. As such, an increase in the twist angle suppresses the bending mode which signifies the reduction in the fundamental frequency and augments the twisting mode that signifies the increase in the second natural frequencies of the sandwich panel. In addition, a decrease in the non-dimensional frequency values is observed with an increase in the operating temperature (T). There is a drastic property degradation is observed in the CNT reinforcements with temperature increment (**Table 10.5**) which results in strength degradation of the CNT reinforced PMMA matrix comprising the composite face sheets. Similar degradation in the material properties of the Titanium honeycomb core is also observed with a rise in the operating temperature leading to a reduction in the stiffness of the honeycomb titanium core. The overall effect is thereby a reduction in the structural stiffness of the honeycomb sandwich panel with an increase in the operating temperature. In addition, internal stresses are developed inside the sandwich panel which results in a reduction in the structural stiffness of the sandwich panel. Similar to the previous case, the highest values of both the first and the second natural frequencies are observed for FG-X distribution pattern while the lowest is again obtained for FG-O pattern irrespective of the twist angle and operating temperature.

Table 10.10. Non-dimensional Fundamental Frequencies $\left(\omega_n = \omega\left(\frac{a^2}{h}\right)\sqrt{\frac{\rho_{m0}}{E_{m0}}}\right)$ of CNTRC composite skin (0/90/0/90/0/**core**/0/90/0/90/0) and **Titanium (*Ti-6Al-4V*) honeycomb core** at different twist angles (ϕ) and operating temperatures (***T***=300K, 500K, 700K) (a/b=1, a/h=10, h_c/h_f=8, h= h_c +2h_f, h_h / l_h =2.0, θ_h =-40^0, ρ_{m0}=1150kg/m^3, E_{m0}=2.50E9GPa)

Mode 1										
Temp.		ϕ **= 0^0**			ϕ **= 15^0**			ϕ **= 30^0**		
(T)	λ_{CNT}	**0.12**	**0.17**	**0.28**	**0.12**	**0.17**	**0.28**	**0.12**	**0.17**	**0.28**
300K	UD	4.255	5.455	5.793	3.591	4.336	5.200	3.957	4.858	5.307
	FG V	4.306	5.563	6.115	3.735	4.530	5.435	3.997	4.946	5.503
	FG Λ	4.240	5.410	5.863	3.427	4.127	5.049	3.936	4.817	5.389
	FG O	4.227	5.376	5.848	3.035	3.653	4.509	3.818	4.626	5.156
	FG X	4.283	5.112	6.257	3.963	4.856	5.793	4.085	5.097	5.757
500K	UD	3.674	3.512	5.013	3.667	4.569	4.805	3.545	4.315	4.401
	FG V	3.689	4.667	5.554	3.654	4.662	5.146	3.541	4.419	4.931
	FG Λ	3.691	4.723	5.202	3.649	4.635	5.101	3.515	4.395	4.817
	FG O	3.607	4.634	5.003	3.553	4.539	4.932	3.393	4.292	4.689

	FG X	3.764	4.856	5.417	3.726	4.768	5.305	3.613	4.553	4.132
	UD	2.953	3.761	3.981	2.933	3.723	3.949	2.865	3.597	3.841
	FG V	2.966	3.799	4.140	2.947	3.762	4.105	2.882	3.641	3.988
700K	FG Λ	2.965	3.799	4.139	2.944	3.754	4.098	2.868	3.611	3.961
	FG O	2.922	3.721	4.002	2.897	3.670	3.958	2.813	3.515	3.818
	FG X	3.011	3.887	4.338	2.993	3.851	4.304	2.931	3.733	4.175

Table 10.11. Non-dimensional Second Frequencies $\left(\omega_n = \omega\left(\frac{a^2}{h}\right)\sqrt{\frac{\rho_{m0}}{E_{m0}}}\right)$ of CNTRC composite skin (0/90/0/90/0/**core**/0/90/0/90/0) and Titanium honeycomb core at different twist angles (ϕ) and operating temperatures (a/b=1, a/h=10, h_c/h_f=8, h= h_c +2h_f, h_h / l_h =2.0, θ_h =-40^0, ρ_{m0}=1150kg/m^3, E_{m0}=2.50E9GPa)

Mode 2										
Temp.		$\phi = 0^0$			$\phi = 15^0$			$\phi = 30^0$		
(T)		**0.12**	**0.17**	**0.28**	**0.12**	**0.17**	**0.28**	**0.12**	**0.17**	**0.28**
	UD	4.861	5.8067	6.8609	4.267	5.174	6.108	5.475	6.585	7.514
	FG V	5.1828	6.1548	7.3128	4.431	5.386	6.376	5.622	6.767	7.789
300K	FG Λ	4.5482	5.4409	6.3845	4.094	4.977	5.965	5.337	6.440	7.446
	FG O	4.5282	5.4397	6.3659	3.710	4.528	5.403	5.026	6.068	7.046
	FG X	4.297	5.553	6.312	4.623	5.745	6.785	5.886	7.043	8.164
	UD	5.031	5.953	5.625	5.126	5.408	5.834	5.524	5.947	6.255
	FG V	5.033	5.942	7.133	5.141	6.097	7.178	5.514	6.341	7.398
500K	FG Λ	4.341	5.397	5.556	4.464	5.562	5.778	4.879	6.126	6.809
	FG O	4.198	5.155	5.649	4.351	5.310	5.806	4.798	5.841	6.371
	FG X	5.096	6.128	6.911	5.210	6.171	6.741	5.604	6.656	6.224
	UD	4.423	5.202	6.189	4.506	5.316	6.302	4.801	5.668	6.571
	FG V	4.578	5.386	6.421	4.660	5.498	6.538	4.946	5.837	6.797
700K	FG Λ	4.259	5.015	5.977	4.347	5.136	6.102	4.653	5.508	6.399
	FG O	3.948	4.656	5.539	4.037	4.775	5.661	4.343	5.182	6.004
	FG X	4.835	5.681	6.772	4.917	5.794	6.896	5.205	6.105	7.124

10.4.4 INFLUENCE OF UNIT CELL DIMENSIONS OF THE HONEYCOMB CORE AND CORE TO FACESHEET THICKNESS RATIO

The dimension of the unit cell that comprises the cellular structure of the honeycomb core has a major influence on the non-dimensional frequencies of the sandwich panel as a whole. Accordingly, the non-dimensional fundamental frequencies $\left(\omega_n = \omega\left(\frac{a^2}{h}\right)\sqrt{\frac{\rho_{m0}}{E_{m0}}}\right)$ of the CNTRC FG-X composite (0/90/**core**/0/90) PMMA face sheets along with Titanium honeycomb core sandwich panel for different values of the rib length to thickness ratio (h_h/l_h) and auxetic re-entrant inclined angle (-θ_h) are presented in **Table 10.12 and Table 10.13** for twist angle of ϕ=0^0 and 30^0, respectively. An increase in the non-dimensional fundamental frequencies is observed with an increase in the rib-thickness ratio (h_h/l_h) for both untwisted (ϕ=0^0) and twisted (ϕ=30^0) sandwich panels corresponding to a particular inclined angle and CNT volume fraction (λ_{CNT}). This may be attributed to an increase in effective Young's modulus (E_1) values of the honeycomb core with an increase in the rib-thickness ratio (h_h/l_h) though the Poisson's ratio values are found to decrease (**Fig. 10.4**) at a particular value of the inclined auxetic angle (-θ_h) as evident from **Fig. 10.3**. However, the increase in the density (**Fig. 10.5**) with an increase in the rib-thickness ratio (h_h/l_h) is seen to be much rapid at higher values of the inclined angle ($-\theta_h$). As a result of this rapid rise in the density values, the rate

of increase in the natural frequency values are found to be somewhat higher at lower values of the inclined angle.

Table 10.12 Non-dimensional Natural Frequencies $\left(\omega_n = \omega\left(\frac{a^2}{h}\right)\sqrt{\frac{\rho_{m0}}{E_{m0}}}\right)$ of CNTRC FG-X composite skin (0/90/core/0/90) and **untwisted** Titanium honeycomb core at different re-entrant angles (a/b=1, a/h=10, h_c/h_f=8, h= h_c +2h_f, h_h / l_h =2.0, $\boldsymbol{\phi=0^0}$, ρ_{m0}=1150kg/m^3, E_{m0}=2.50E9GPa, T=300K)

θ_{Aux}	h_h / l_h **=2.0**			h_h / l_h **=3.0**			h_h / l_h **=4.0**		
	0.12	**0.17**	**0.28**	**0.12**	**0.17**	**0.28**	**0.12**	**0.17**	**0.28**
-35	4.7358	6.3116	7.5657	5.1930	6.9384	8.3187	5.4374	7.0407	8.2453
-45	4.3027	5.7293	6.8735	4.8003	5.9454	7.1515	5.1120	6.2989	7.4022
-55	3.8197	5.0804	6.1008	4.3981	5.4863	6.5139	4.7007	5.5716	6.5359
-65	3.2598	4.1794	5.0288	3.8567	4.5805	5.4175	4.0775	4.6929	5.4514
-75	2.5936	3.0630	3.6663	2.9747	3.4195	3.9681	3.0824	3.4920	3.9690

Table 10.13. Non-dimensional Natural Frequencies $\left(\omega_n = \omega\left(\frac{a^2}{h}\right)\sqrt{\frac{\rho_{m0}}{E_{m0}}}\right)$ of CNTRC FG-X composite skin (0/90/core/0/90) and **twisted** Aluminum honeycomb core at different re-entrant angles (a/b=1, a/h=10, h_c/h_f=8, h= h_c +2h_f, θ_{Aux} =-40^0, $\boldsymbol{\phi=30^0}$, ρ_{m0}=1150kg/m^3, E_{m0}=2.50E9GPa, T=300K)

θ_{Aux}	h_h / l_h **=2.0**			h_h / l_h **=3.0**			h_h / l_h **=4.0**		
	0.12	**0.17**	**0.28**	**0.12**	**0.17**	**0.28**	**0.12**	**0.17**	**0.28**
-35	4.5638	5.9217	7.00477	4.7690	5.9841	7.0361	4.8093	5.9200	6.9380
-45	4.0559	5.1643	6.1029	4.1304	5.0820	6.0712	4.4079	5.3743	6.3074
-55	3.5016	4.3899	5.2204	3.8148	4.6726	5.5283	3.9621	4.7934	5.6147
-65	2.8691	3.5378	4.2262	3.2499	3.9417	4.6480	3.4033	4.0667	4.7219
-75	2.1751	2.6393	3.1398	2.5053	2.9734	3.4467	2.6186	3.0531	3.4729

The non-dimensional frequencies of CNTRC composite skin (0/90/core/0/90) untwisted sandwich panel at different temperatures with re-entrant auxetic (θ_h=-40^0) aluminum core are presented in **Table 10.14** for different values of the core to face sheet thickness ratio (h_c / h_f) and CNT distribution patterns. The non-dimensional frequency values are found to decrease with an increase in the h_c / h_f value irrespective of the operating temperature and the CNT distribution pattern considered. This may be attributed to the fact that an increase in the core to face sheet thickness ratio results in a reduced strength contribution from the much thinner face sheets that are reinforced by CNT compared to the core material that is comparatively thicker but is of much lesser strength.

Table 10.14. Non-dimensional Fundamental Frequencies $\left(\omega_n = \omega\left(\frac{a^2}{h}\right)\sqrt{\frac{\rho_{m0}}{E_{m0}}}\right)$ of CNTRC composite skin (0/90/core/0/90) untwisted Aluminum honeycomb core for different core to face sheets ratios of the auxetic honeycomb panel (a/b=1, a/h=10, h= h_c +2h_f, h_h/l_h =2.0, θ_h=-40^0, ϕ=0^0, ρ_{m0}=1150kg/m^3, E_{m0}=2.50E9GPa, T=300K)

$\boldsymbol{\phi=0^0}$	$\boldsymbol{h_c/h_f}$**=4**			$\boldsymbol{h_c/h_f}$ **=6**			$\boldsymbol{h_c/h_f}$ **=10**		
	300K	**500K**	**700K**	**300K**	**500K**	**700K**	**300K**	**500K**	**700K**
UD	4.109	3.618	2.915	3.645	3.146	2.552	3.019	2.633	2.143
FG V	3.978	3.674	2.923	3.611	3.154	2.565	3.021	2.654	2.154
FG Λ	3.796	3.387	2.933	3.554	3.174	2.568	3.025	2.650	2.156

FG O	1.791	1.583	1.270	1.685	1.515	1.201	1.513	1.339	1.086
FG X	4.524	3.891	3.127	3.929	3.394	2.735	3.248	2.801	2.288

10.4.5 INFLUENCE OF ROTATIONAL SPEED AT VARYING TEMPERATURES

The non-dimensional fundamental frequencies $\left(\omega_n = \omega\left(\frac{a^2}{h}\right)\sqrt{\frac{\rho_{m0}}{E_{m0}}}\right)$ of CNT reinforced composite PMMA skin (0/90/**core**/0/90) untwisted sandwich panel (λ_{CNT} = *0.12*) comprising of a titanium based (*Ti-6Al-4V)* honeycomb core are presented for varying values of the non-dimensional rotational speed (**Ω**) in **Table 10.15** in case of re-entrant and non re-entrant inclined angles of θ_h=-40^0 and +40^0, respectively. The non-dimensional fundamental frequency values are found to increase with an increase in the non-dimensional rotational speed in case of both re-entrant and non re-entrant incline angle (θ_h) which is a direct consequence of the centrifugal stiffening effect arising out of rotation. In general, the non-dimensional frequency values are higher for the non re-entrant core (+θ_h) sandwich panels compared to the re-entrant core (-θ_h) for all combinations of the CNT distribution pattern and rotational speed. For a certain value of the non-dimensional rotational speed, the highest value of the non-dimension fundamental frequency is observed for the FG-X configuration while the lowest is observed for the FG-O distribution pattern of the CNT's. The non-dimensional fundamental frequencies of FG-X CNT distribution pattern are plotted considering different values of hub-radius to span ratio $\left(\frac{r_{hub}}{a}\right)$ considering (0/90/0/90/0/**core**/0/90/0/90/0) PMMA composite sandwich panels in **Fig. 10.7 and Fig. 10.8** for re-entrant angle and non re-entrant angles, respectively. An increase in the non-dimensional fundamental frequency values is observed with an increase in the hub radius (r_{hub}) irrespective of the inclined angle (θ_h) and thickness ratio (h_h/l_h) for both re-entrant and non re-entrant honeycomb core. This arises from the fact that higher values of the hub radius results in higher values of the centrifugal forces which in turn results in higher initial deflections and enhanced stiffness of the sandwich panel owing to the addition of the geometric stiffness matrix. From **Fig. 10.7**, it is evident that for a certain value of the re-entrant inclined angle, an increase in the thickness ratio (h_h/l_h) results in an increase in the non-dimensional fundamental frequency values irrespective of the hub-radius value. Similarly, from **Fig. 10.8**, an increase in the hub radius results in an increase in the non-dimensional frequency but the reverse trend is observed with an increase in the operating temperature from *T*=300K to *T*=500K.

Table 10.15. Non-dimensional fundamental frequencies $\left(\omega_n = \omega\left(\frac{a^2}{h}\right)\sqrt{\frac{\rho_{m0}}{E_{m0}}}\right)$ of CNTRC composite PMMA skin (0/90/**core**/0/90) Titanium (***Ti-4Al-6V***) honeycomb core sandwich panel at different rotational speeds (a/b=1, a/h=10, h_c/h_f=8, h= h_c +2h_f, ϕ=0^0, h_h/l_h =2.0, ρ_{m0}=1150kg/m^3, λ_{CNT}=0.12, E_{m0}=2.50E9GPa, Ω=0.00, 0.25, 0.50, 0.75 and 1.00)

θ_h		Ω=0.00		Ω=0.25		Ω=0.50		Ω=0.75		Ω=1.0	
	ϕ=0^0	300K	500K	300K	500K	300K	500K	300K	500K	300K	500K
-40^0 (Auxetic)	**UD**	4.199	3.649	4.366	3.787	4.828	4.155	5.506	4.755	6.326	5.465
	FG-V	4.214	3.388	4.389	3.656	4.869	4.132	5.564	4.734	6.401	5.494
	FG-Λ	4.215	2.493	4.385	2.792	4.842	3.361	5.509	3.902	6.316	4.411
	FG-O	2.103	1.904	2.211	2.007	2.473	2.276	2.832	2.629	3.254	2.493
	FG-X	4.530	3.901	4.714	4.061	5.222	4.507	5.966	5.124	6.865	6.245
+40^0	**UD**	4.848	4.632	5.176	4.920	6.034	5.683	7.217	6.744	8.570	7.971
	FG-V	3.546	3.417	3.804	3.665	4.472	4.309	5.383	5.189	6.424	6.195

(Non-Auxetic)	**FG-Λ**	3.371	3.245	3.607	3.472	4.219	4.061	5.057	4.869	6.018	5.797
	FG-O	1.601	1.409	1.731	1.525	2.061	1.819	2.496	2.206	2.976	2.632
	FG-X	5.745	4.972	6.106	5.285	7.067	6.118	8.404	7.279	8.857	8.624

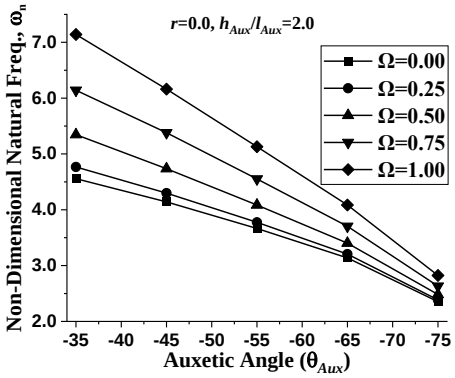

(a) r_{Hub}/a=0.0, h_h/l_h=2.0

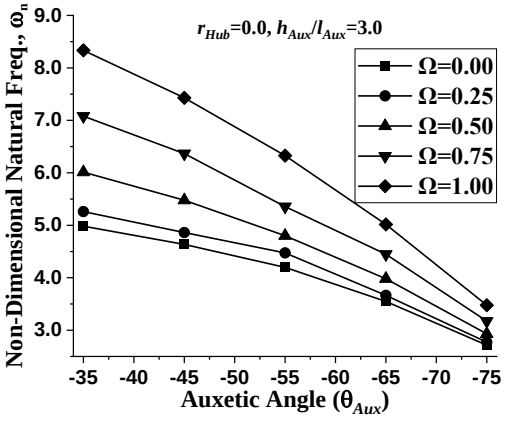

(b) r_{Hub}/a =0.0, h_h/l_h =3.0

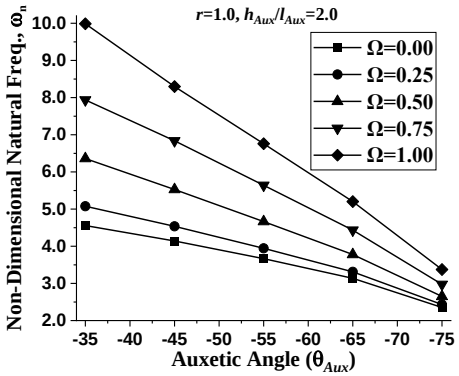

(c) r_{Hub}/a=1.0, h_h/l_h=2.0

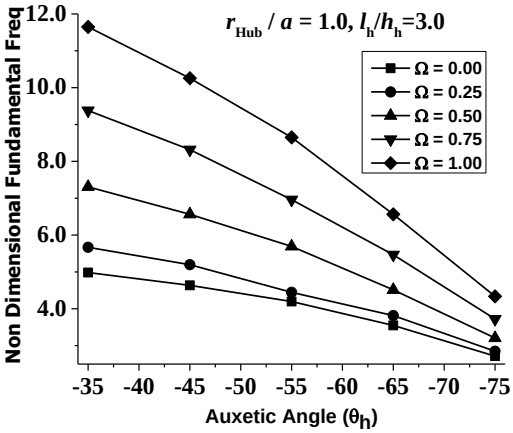

(d) r_{Hub}/a=1.0, h_h/l_h=3.0

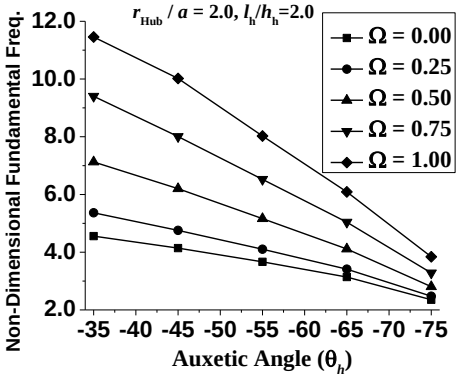

(e) r_{Hub}/a=2.0, h_h/l_h=2.0

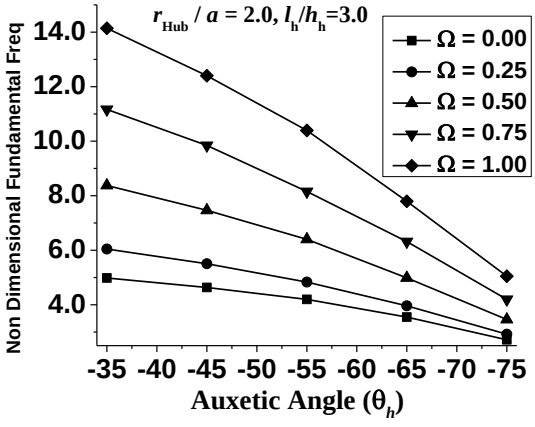

(f) r_{Hub}/a=2.0, h_h/l_h =3.0

Fig. 10.7. Plot of the non-dimensional fundamental frequencies $\left(\omega_n = \omega\left(\frac{a^2}{h}\right)\sqrt{\frac{\rho_m}{E_m}}\right)$ of CNTRC **FG-X** composite skin (0/90/0/90/0/core/0/90/0/90/0) and untwisted Titanium honeycomb core for different hub to span ratio (r_{hub} / a) and re-entrant inclined angles (-θ_{Aux})

(a/b=1, a/h=10, h_c/h_f=8, h= h_c +2h_f, h_h / l_h =2.0, ϕ=0^0, λ_{CNT}=0.12**,** FG-V, ρ_{m0}=1150kg/m^3, E_{m0}=2.50E9GPa, T=300K)

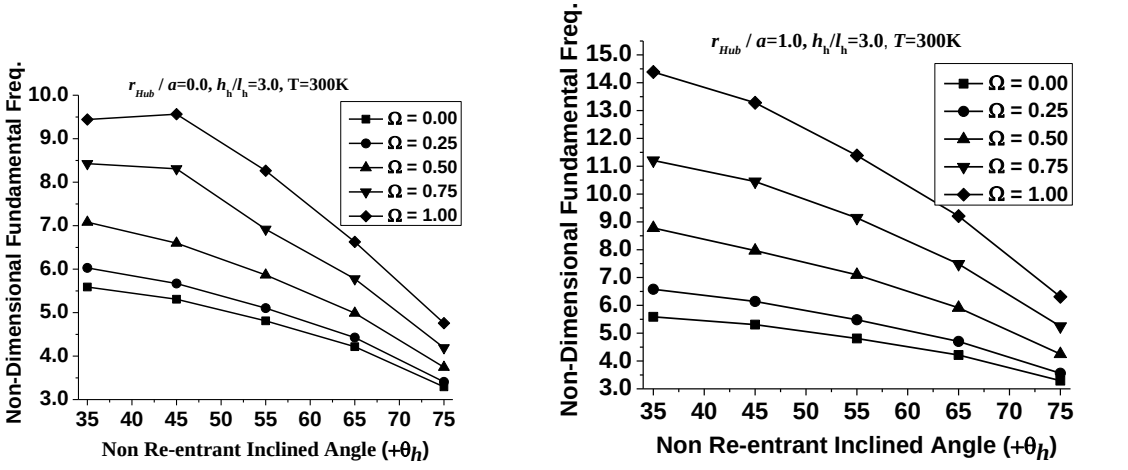

(a) r_{Hub}=0.0, h_h/l_h =3.0,T=300K **(b) r_{Hub}=1.0, h_h/l_h =3.0, T=300K**

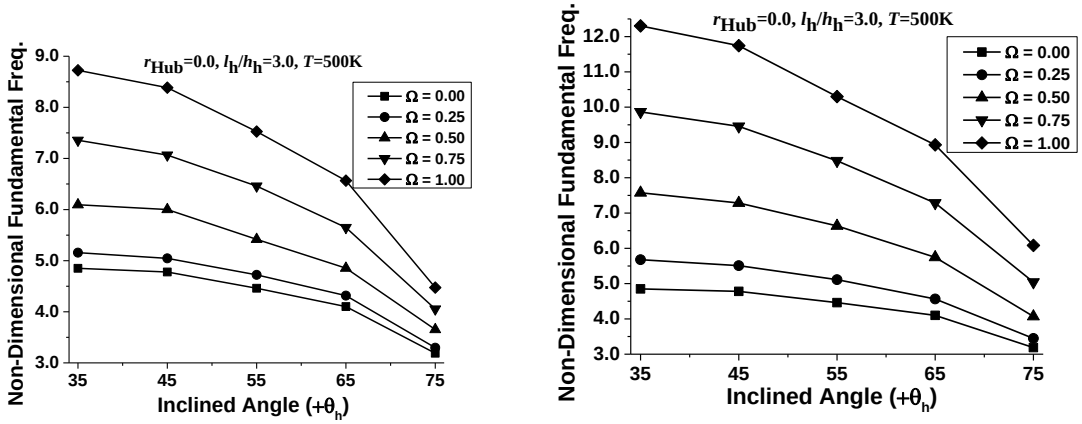

(a) r_{Hub}=0.0, h_h/l_h =3.0,T=500K **(b) r_{Hub}=1.0, h_h/l_h =3.0, T=500K**

Fig. 10.8 Plot of the non-dimensional fundamental frequencies $\left(\omega_n = \omega\left(\frac{a^2}{h}\right)\sqrt{\frac{\rho_{m0}}{E_{m0}}}\right)$ of CNTRC **FG-X** composite skin (0/90/0/90/0/core/0/90/0/90/0) and untwisted Titanium honeycomb core for different hub to span ratio (r_{hub} / a) and non re-entrant angles (θ_{Aux}) and temperatures (T=300K and 700K) (a/b=1, a/h=10, h_c/h_f=8, h= h_c +2h_f, h_h / l_h =3.0, ϕ=0^0, λ_{CNT}=0.12**,** FG-V, ρ_{m0}=1150kg/m^3, E_{m0}=2.50E9GPa, T=300K, 500K and 700K)

10.5. MODE SHAPE STUDY OF HONEYCOMB AUXETIC CORE SANDWICH PANELS

The first three mode shape of untwisted (ϕ=0^0) and stationary (Ω=0.0) sandwich plates made from CNT reinforced (0/90/0/90/0/core/0/90/0/90/0) composite skin PMMA matrix as face sheets and an auxetic honeycomb core are plotted for different combinations of re-entrant and non re-entrant auxetic angle, CNT distribution pattern and operating temperatures. **Table 10.16** presents the mode shapes for uniformly distributed (UD) CNT reinforcements in the PMMA matrix at T=300K at h_h / l_h =3.0 for different values of the re-entrant angle ranging from -20^0 to -70^0 The mode shapes indicate that the first mode is the first bending for higher values of the auxetic angles (θ_h = -50^0, -60^0 and -70^0) although it is the symmetry mode at lower values of the auxetic angle (θ_h = -20^0, -30^0 and -40^0). However, the second mode is the found to be

the symmetric twisted mode, except at θ_h = -40^0 where again the bending mode is observed. Similarly, from the mode shape of non re-entrant honeycomb core presented in **Table 10.17,** it is observed that the first mode is the bending mode except at at lower inclined angles (θ_h = 20^0), while the second and third modes are mostly the symmetric mode indicating torsion. **Table 10.18** presents the mode shapes of the auxetic honeycomb sandwich panels at θ_h = -40^0 for different CNT volume fractions (λ_{CNT}) and operating temperature (***T***). The mode shapes at lower CNT volume fractions are mostly the symmetric ones at lower temperatures (T=300K and 500K) but the symmetry is lost at higher CNT volume fractions and temparetures.

Table 10.16 ***Mode Shapes*** of CNTRC composite skin (0/90/0/90/0/**core**/0/90/0/90/0) untwisted Titanium honeycomb core for different re-entrant angles (-θ_h) for UD distribution pattern
(a=b=1.0m, a/h=10, h_c/h_f=8, h= h_c +2h_f, h_h / l_h =3.0, ϕ=0^0, λ_{CNT}=0.12 (**UD**), ρ_{m0}=1150kg/m^3, E_{m0}=2.50E9GPa, T=300K)

	θ_h	***Mode 1***	***Mode 2***	***Mode 3***
***h/l* =3 UD**	**-20**	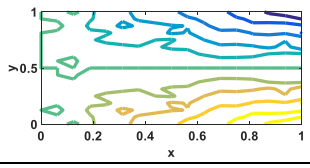	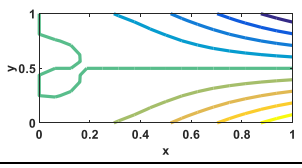	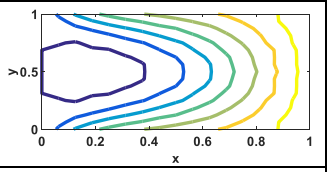
	-30^0	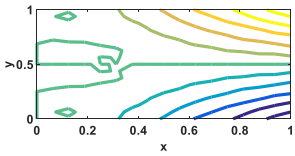	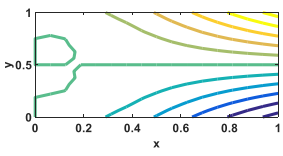	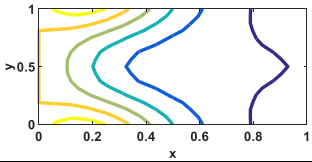
	-40	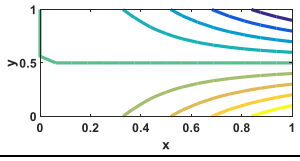	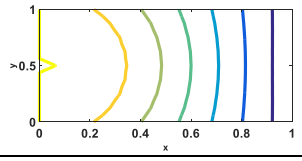	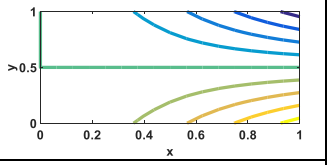
	-50	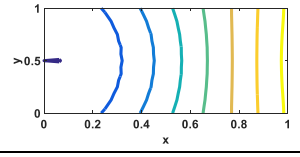	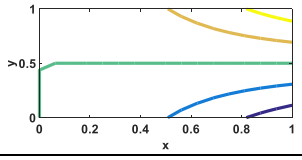	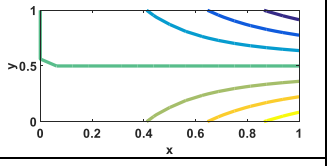
	-60	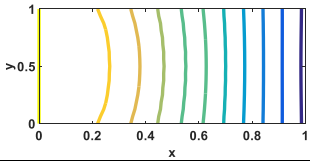	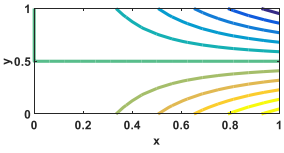	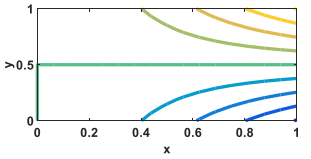
	-70	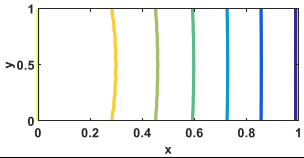	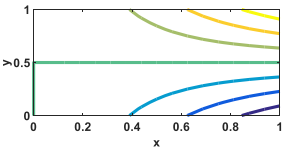	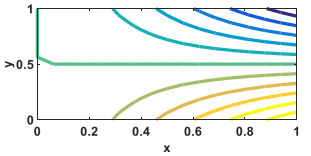

Table 10.17. ***Mode Shapes*** of CNTRC composite skin (0/90/0/90/0/**core**/0/90/0/90/0) untwisted Titanium honeycomb core for different non re-entrant angles (+θ_h) for UD distribution pattern
(a=b=1.0m, a/h=10, h_c/h_f=8, h= h_c +2h_f, h_h / l_h =3.0, ϕ=0^0, λ_{CNT}=0.12 (**UD**), ρ_{m0}=1150kg/m^3, E_{m0}=2.50E9GPa, T=300K)

	θ_h	***Mode 1***	***Mode 2***	***Mode 3***

***h/l*= 3 UD**	**20**	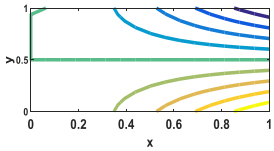	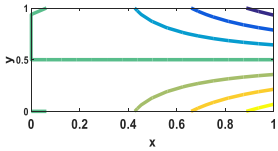	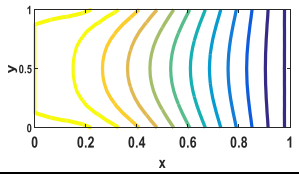
	30	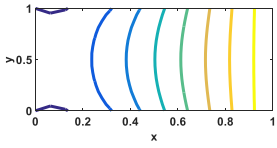	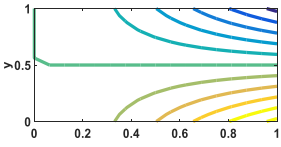	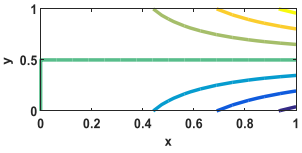
	40	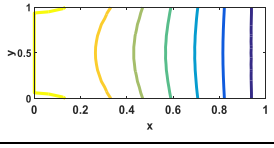	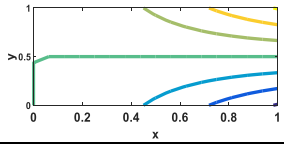	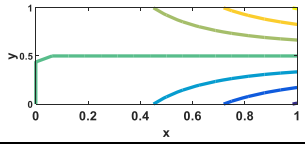
	50	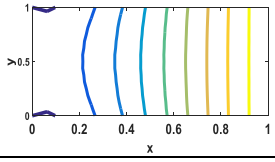	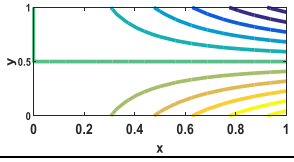	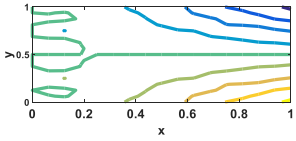

Table 10.18. ***Mode Shapes*** of CNTRC composite skin (0/90/0/90/0/**core**/0/90/0/90/0) and untwisted Titanium honeycomb core for different CNT volume fractions (λ_{CNT}) and operating temperatures (a=b=1.0m, a/h=10, h_c/h_f=8, h= h_c +2h_f, h_h / l_h =2.0, ϕ=0^0, θ_h =-40^0, λ_{CNT}=0.12 (**FG-Λ**), ρ_{m0}=1150kg/m^3, E_{m0}=2.50E9GPa, T=300K, 500K and 700K)

T	***v_CNT***	***Mode 1***	***Mode 2***	***Mode 3***
300	**0.12**	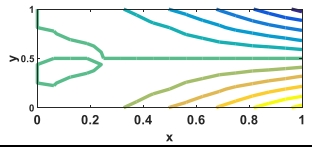	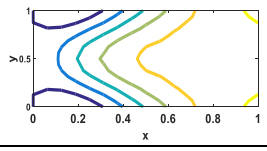	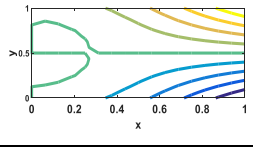
	0.17	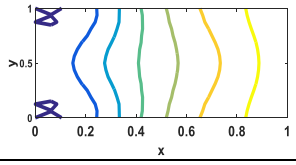	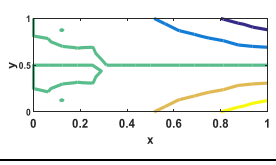	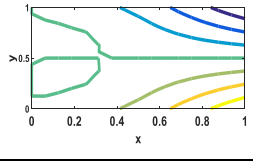
	0.28	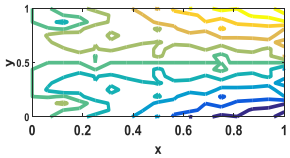	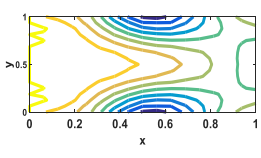	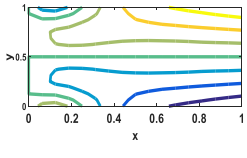
500	**0.12**	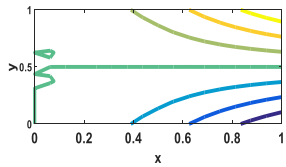	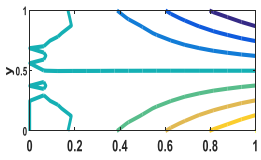	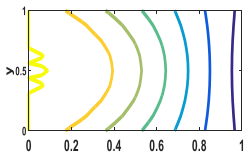
	0.17	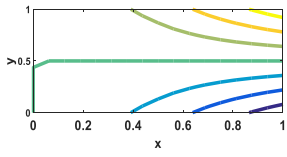	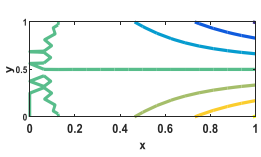	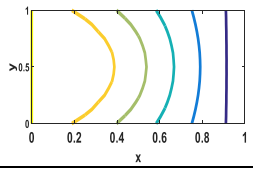

	0.28	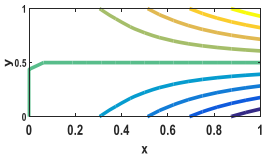	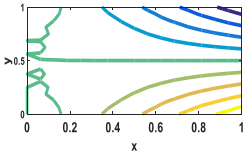	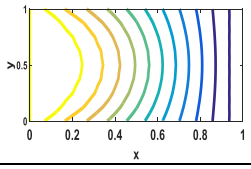
700	**0.12**	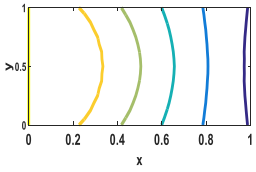	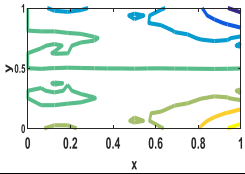	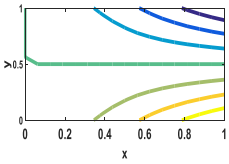
	0.17	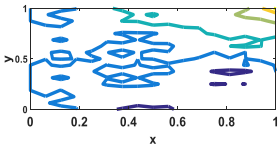	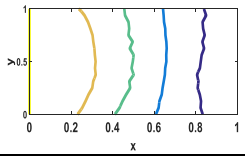	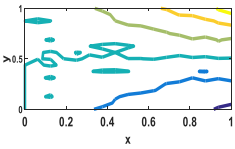
	0.28	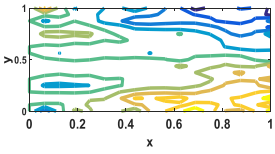	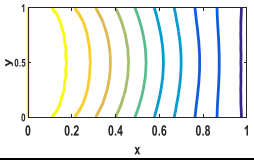	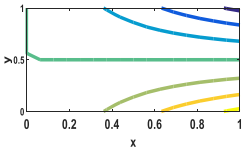

CH 11: CONCLUSION

From the above results ,it is concluded that:

- The natural frequencies of the sandwich panel are observed to be higher for relatively soft aluminium core compared to the titanium core for all combinations of the panel aspect ratio and the CNT distribution patterns.
- an increase in the non-dimensional frequencies is observed for both the core types (Ti-6Al-4V core and aluminium core) with an increase in the volume fraction of CNT (λ_{CNT} = 0.12, 0.17 and 0.28)
- For all the CNT distribution patterns considered, the highest value of the non-dimensional first and second frequencies is observed for FG-X followed by the FG-V, UD, FG-Λ and FG-O patterns for a particular CNT volume fraction in both the core types considered.
- An increase in the aspect ratio of the sandwich panel results in an increase in both the first and the second non-dimensional frequencies
- It is observed that there is a reduction in the non-dimensional fundamental frequencies with an increase in the twist angle (ϕ) while the reverse is generally observed in case of the second natural frequencies.
- A decrease in the non-dimensional frequency values is observed with an increase in the operating temperature (T).
- An increase in the non-dimensional fundamental frequencies is observed with an increase in the rib-thickness ratio (h_h/l_h) for both untwisted ($\phi=0^0$) and twisted ($\phi=30^0$) sandwich panels corresponding to a particular inclined angle and CNT volume fraction (λ_{CNT}).
- Non-dimensional fundamental frequencies is higher at lower value of inclined angle ($-\theta_h$)
- The non-dimensional frequency values are found to decrease with an increase in the h_c / h_f value irrespective of the operating temperature and the CNT distribution pattern considered.
- In case of re-entrant and non re-entrant inclined angles of θ_h=-40^0 and +40^0, respectively. The non-dimensional fundamental frequency values are found to increase with an increase in the non-dimensional rotational speed in case of both re-entrant and non re-entrant incline angle (θ_h)
- An increase in the non-dimensional fundamental frequency values is observed with an increase in the hub radius (r_{hub}) irrespective of the inclined angle (θ_h) and thickness ratio (h_h/l_h) for both re-entrant and non re-entrant honeycomb core.
- Various mode shapes were observed whether it was bending mode or symmetric twisted mode or another mode.

REFERENCES:

1 .Sreenivasamurthy, S. and Ramamurti, V., 1981. Coriolis effect on the vibration of flat rotating low aspect ratio cantilever plates. *The Journal of Strain Analysis for Engineering Design*, *16*(2), pp.97-106.

2. Kant, T. and Swaminathan, K., 2001. Analytical solutions for free vibration of laminated composite and sandwich plates based on a higher-order refined theory. *Composite structures*, *53*(1), pp.73-85.

3 . Rao, M.K. and Desai, Y.M., 2004. Analytical solutions for vibrations of laminated and sandwich plates using mixed theory. *Composite Structures*, *63*(3-4), pp.361-373.

4 . Zhu, P., Lei, Z.X. and Liew, K.M., **2012**. Static and free vibration analyses of carbon nanotube-reinforced composite plates using finite element method with first order shear deformation plate theory. *Composite Structures*, *94*(4), pp.1450-1460.

5 . Balawi, S. and Abot, J.L., 2008. The effect of honeycomb relative density on its effective in-plane elastic moduli: An experimental study. *Composite Structures*, *84*(4), pp.293-299.

6 . Chen, D.H. and Ozaki, S., 2009. Analysis of in-plane elastic modulus for a hexagonal honeycomb core: Effect of core height and proposed analytical method. *Composite Structures*, *88*(1), pp.17-25.

7 . Lei, Z.X., Liew, K.M. and Yu, J.L., 2013. Free vibration analysis of functionally graded carbon nanotube-reinforced composite plates using the element-free kp-Ritz method in thermal environment. *Composite Structures*, *106*, pp.128-138.

8. Wang, Y.J., Zhang, Z.J., Xue, X.M. and Zhang, L., **2019**. Free vibration analysis of composite sandwich panels with hierarchical honeycomb sandwich core. *Thin-Walled Structures*, *145*, p.106425.

9. M. Grujicic, R. Galgalikar, J.S. Snipes, et al., Multi-physics modeling of the fabrication and dynamic performance of all-metal auxetic-hexagonal sandwich-structures, Mater. Des. 51 (2013) 113–130.

10. M. Grujicic, R. Galgalikar, J.S. Snipes, et al., Multi-physics modeling of the fabrication and dynamic performance of all-metal auxetic-hexagonal sandwich-structures, Mater. Des. 51 (2013) 113–130.

11. N.T. Duong, N.D. Duc, Evaluation of elastic properties and thermal expansion coefficient of composites reinforced by randomly distributed spherical particles with negative Poisson's ratios, Compos. Struct. 153 (2016) 569–577.

12. N.D. Duc, P.H. Cong, Nonlinear dynamic response and vibration of sandwich composite plates with negative Poisson's ratio in auxetic honeycombs, J. Sandw. Struct. Mater. (2016).

13. Duc, N.D., Seung-Eock, K., Tuan, N.D., Tran, P. and Khoa, N.D., 2017. New approach to study nonlinear dynamic response and vibration of sandwich composite cylindrical panels with auxetic honeycomb core layer. *Aerospace Science and Technology*, *70*, pp.396-404.

14. Wang, X., Zhao, Z.Y., Li, L., Zhang, Z.J., Zhang, Q.C., Han, B. and Lu, T.J., 2019. Free vibration behaviour of Ti-6Al-4V sandwich beams with corrugated channel cores: Experiments and simulations. *Thin-Walled Structures*, *135*, pp.329-340.

15. Wang, Y.J., Zhang, Z.J., Xue, X.M. and Zhang, L., 2019. Free vibration analysis of composite sandwich panels with hierarchical honeycomb sandwich core. *Thin-Walled Structures*, *145*, p.106425.

16 . Wang, Y.J., Zhang, Z.J., Xue, X.M. and Zhang, L., 2019. Free vibration analysis of composite sandwich panels with hierarchical honeycomb sandwich core. *Thin-Walled Structures*, *145*, p.106425.
17. Zhao, Y., Ge, M. and Ma, W., 2020. The effective in-plane elastic properties of hexagonal honeycombs with consideration for geometric nonlinearity. *Composite Structures*, *234*, p.111749.
18 . Singha, T.D., Rout, M., Bandyopadhyay, T. and Karmakar, A., 2020. Free vibration analysis of rotating pre-twisted composite sandwich conical shells with multiple debonding in hygrothermal environment. *Engineering Structures*, *204*, p.110058.
19 . Singha, T.D., Rout, M., Bandyopadhyay, T. and Karmakar, A., 2021. Free vibration of rotating pre-twisted FG-GRC sandwich conical shells in thermal environment using HSDT. *Composite Structures*, *257*, p.113144.

20 . Pham, Q.H., Nguyen, P.C. and Tran, T.T., 2022. Free vibration response of auxetic honeycomb sandwich plates using an improved higher-order ES-MITC3 element and artificial neural network. *Thin-Walled Structures*, *175*, p.109203.
21 . Kushwaha, Y.S., Hemanth, N.S., Badgayan, N.D. and Sahu, S.K., 2022. Free vibration analysis of PLA based auxetic metamaterial structural composite using finite element analysis. *Materials Today: Proceedings*, *56*, pp.1063-1067.
22 . Liu, Y., Shi, X., Wang, Z., Wang, X., Xiong, J. and Guan, Z., 2023. Nonlinear vibrations of all-composite sandwich plates with a hexagon honeycomb core: Theoretical and experimental investigations. *Composite Structures*, *305*, p.116512.
23 . Jiang, W., Zhou, J., Liu, J., Zhang, M. and Huang, W., 2023. Free vibration behaviours of composite sandwich plates with re-entrant honeycomb cores. *Applied Mathematical Modelling*, *116*, pp.547-568.
24. Hamrouni, A., Rebiere, J.L., El Mahi, A., Beyaoui, M. and Haddar, M., 2023. Experimental and finite element analyses of a 3D printed sandwich with an auxetic or non-auxetic core. *Journal of Sandwich Structures & Materials*, p.10996362231151454.
25. Jiang, W., Zhou, J., Liu, J., Zhang, M. and Huang, W., 2023. Free vibration behaviours of composite sandwich plates with reentrant honeycomb cores. Applied Mathematical Modelling, 116, pp.547-568.
26. Hamrouni, A., Rebiere, J.L., El Mahi, A., Beyaoui, M. and Haddar, M., 2023. Experimental and finite element analyses of a 3D printed sandwich with an auxetic or non-auxetic core. Journal of Sandwich Structures & Materials, p.10996362231151454.
27.Yeganeh-Haeri A, Weidner DJ, Parise JB (1992) Elasticity of α-cristobalite: a silicon dioxide with a negative Poisson's ratio. Science 257(5070):650–652
28. Cellular solid Structure and properties-second edition by Lorna J. Gibson and Michael F. Ashby page 106-184
29. Qian, D., Dickey, E.C., Andrews R., and Rantell, T. (2000), Load Transfer and Deformation Mechanisms in Carbon Nanotube-Polystyrene Composites, Applied Physics Letter, Vol. 76, pp. 2868-2870.

30 .Shen, H.S. (2009), Nonlinear Bending of Functionally Graded Carbon Nanotube-Reinforced Composite Plates in Thermal Environments, Composite Structures, Vol. 91, No. 1, pp. 9-19.
31. Qian, D., Dickey, E.C., Andrews R., and Rantell, T. (2000), Load Transfer and Deformation Mechanisms in Carbon Nanotube-Polystyrene Composites, Applied Physics Letter, Vol. 76, pp. 2868-2870.

32 .Seidel, G.D., and Lagoudas, D.C. (2006), Micromechanical Analysis of the Effective Elastic Properties of Carbon Nanotube Reinforced Composites, Mechanics of Materials, Vol. 38, pp. 884-907.
33 .Jones, R.M. (1975), Mechanics of Composite Materials, McGraw Hill Kogakusha Limited.
34 . Cook, R.D., Malkus, D.S., and Plesha, M.E. (1989), Concepts and Applications of Finite Element Analysis, John Wiley & Sons, New York
35 . Bathe, K.J. (1990), Finite Element Procedures in Engineering Analysis, New Delhi: Prentice Hall of India.
36. M. T. HEIDEMAN & C. S. BURRUS, "A Bibliography of Fast Transform and Convolution Algorithms II," Technical Report Number 8402, Electrical Engineering Dept., Rice University, Houston, TX 77251-1892, Feb. •984.